Methods of Determining Electron Concentrations in the Magnetosphere from Nose Whistlers

by

C. G. Park

January 1972

Technical Report No. 3454-1

RADIOSCIENCE LABORATORY

STANFORD ELECTRONICS LABORATORIES

STANFORD UNIVERSITY · STANFORD, CALIFORNIA

DOCUMENT CONTROL DATA - R & D

(Security classification of title, body of abstract and indexing annotation must be entered when the overall report is classified)

1. ORIGINATING ACTIVITY (Corporate author)	2a. REPORT SECURITY CLASSIFICATION
Stanford Electronics Laboratories	Unclassified
	2b. GROUP

3. REPORT TITLE

Methods of Determining Electron Concentrations in the Magnetosphere From Nose Whistlers

4. DESCRIPTIVE NOTES (Type of report and inclusive dates)

Technical Report

5. AUTHOR(S) (First name, middle initial, last name)

Park, Chung G.

6. REPORT DATE	7a. TOTAL NO. OF PAGES	7b. NO. OF REFS
January 1972	100	21

8a. CONTRACT OR GRANT NO. NSF GA-19608, GA-18128 GA-28042, NGL-05-020-008.	9a. ORIGINATOR'S REPORT NUMBER(S)
b. PROJECT NO.	Technical Report No. 3454-1
c.	9b. OTHER REPORT NO(S) (Any other numbers that may be assigned this report)
d.	SEL-73-334

10. DISTRIBUTION STATEMENT

Reproduction in whole or in part is permitted for any purpose of the United States Government.

11. SUPPLEMENTARY NOTES	12. SPONSORING MILITARY ACTIVITY

13. ABSTRACT

Whistler propagation in the magnetosphere is studied in detail to find accurate and economical means of determining the path latitude and the electron concentration along the path from whistler parameters f_n (nose frequency) and t_n (travel time at the nose). Longitudinal propagation in field aligned whistler ducts of cold plasma is assumed, and the earth's magnetic field is approximated by a centered dipole. The effects of whistler propagation in the earth-ionosphere waveguide and through the conjugate ionospheres are treated as small perturbations. Several alternative methods are described so that the most economical method may be chosen depending on the desired accuracy and the availability of a computer or a calculator.

DD FORM 1473 1 NOV 65

14. KEY WORDS	LINK A		LINK B		LINK C	
	ROLE	WT	ROLE	WT	ROLE	WT
WHISTLER						
ELECTRON DENSITY						
MAGNETOSPHERE						
DIPOLE GEOMETRY						

METHODS OF DETERMINING ELECTRON CONCENTRATIONS IN

THE MAGNETOSPHERE FROM NOSE WHISTLERS

by

C. G. Park

January 1972

Technical Report No. 3454-1

Radioscience Laboratory

Stanford University   Stanford, California

Preceding page blank

ABSTRACT

Whistler propagation in the magnetosphere is studied in detail to find accurate and economical means of determining the path latitude and the electron concentration along the path from whistler parameters f_n (nose frequency) and t_n (travel time at the nose). Longitudinal propagation in field aligned whistler ducts of cold plasma is assumed, and the earth's magnetic field is approximated by a centered dipole. The effects of whistler propagation in the earth-ionosphere waveguide and through the conjugate ionospheres are treated as small perturbations. Several alternative methods are described so that the most economical method may be chosen depending on the desired accuracy and the availability of a computer or a calculator.

CONTENTS

LIST OF TABLES

ILLUSTRATIONS

NOMENCLATURE AND NOTATION

c	: speed of light in vacuo	$(2.9978 \times 10^{10} \text{ cm sec}^{-1})$
e	: electronic charge	$(1.6021 \times 10^{-19} \text{ coulombs})$
m_e	: electron mass	$(9.1066 \times 10^{-28} \text{ grams})$
m_p	: proton mass	$(1837\ m_e)$
k	: Boltzmann's constant	$(1.3805 \times 10^{-16} \text{ erg deg}^{-1})$
g_o	: acceleration of gravity at sea level	$(980.67 \text{ cm sec}^{-2})$
ϵ_o	: permitivity of vacuum	$(8.854 \times 10^{-12} \text{ farads m}^{-1})$
R_E	: mean earth's radius	(6370 km)
ϕ	: dipole latitude	
θ	: dipole colatitude	
r	: geocentric distance	
L	: McIlwain's parameter	
δ	: magnetic dip angle	
h	: altitude	
S	: arc length of field line	
n	: electron concentration	
N_T	: electron tube content	
f_H	: electron gyrofrequency	
f_p	: plasma frequency	
f_n	: whistler nose frequency	
f'_n	: nose frequency corrected for dispersion due to the ionosphere	
t_n	: whistler travel time at nose frequency	
t'_n	: travel time at nose corrected for dispersion due to the ionosphere.	

D   : whistler dispersion $(tf^{1/2})$

SUBSCRIPTS:

o   : earth's surface

l   : 1000 km altitude

eq   : equatorial plane

LIST OF ELECTRON CONCENTRATION MODELS

	Abbreviation	Temperature	Ionic composition at 1000 km altitude		
			O^+	H^+	He^+
Diffusive Equilibrium Model	DE-1	$1600^\circ K$	90%	8%	2%
	DE-2	3200	90	8	2
	DE-3	1600	50	40	10
	DE-4	800	50	40	10
Collisionless Model	CL	1600	–	100	–
	R-4	$n \propto r^{-4}$			
Hybrid Model	HY	DE-2 for $\phi > 30^\circ$			
		CL for $\phi < 30^\circ$			

ACKNOWLEDGEMENTS

I. INTRODUCTION

A. INTRODUCTION

When Storey successfully explained whistlers in 1953 as radiation from lightning propagating from hemisphere to hemisphere along geomagnetic lines of force, he also discovered that an equatorial electron concentration of ~ 400 cm^{-3} at a geocentric distance of 3 R_E was required to explain the observed whistler dispersion [Storey, 1953]. This was the first evidence of such large electron concentrations far beyond normal F2 layer heights, and it opened a new region of interest for exploration which later came to be called the protonosphere, magnetosphere or plasmasphere. Since then whistlers have provided a powerful and unique tool for probing this remote region of space, and much progress in our understanding of the morphology and dynamics of the inner magnetosphere has been made through ground-based whistler observations.

The discovery of nose whistlers [Helliwell et al., 1956] added the possibility of determining whistler path latitude and permitted more detailed studies of plasma distribution in the magnetosphere [Smith, 1960]. This led to the discovery of the plasmapause [Carpenter, 1962, 1963] and later to detailed descriptions of its dynamical behavior and to measurements of electron concentration profiles inside and outside the plasmapause [Carpenter, 1966; Angerami and Carpenter, 1966; Carpenter, 1970; Park and Carpenter, 1970]. More recently, the whistler technique has been used to measure cross-L motions of thermal plasma in the plasmasphere [Carpenter and Stone, 1967; Park and Carpenter, 1970; Carpenter et al,1971] and coupling fluxes of ionization between the protonosphere and the ionosphere [Park, 1970].

As the whistler technique finds more applications in magnetospheric research, there is a growing need for simple means of processing the data and for improvements in accuracy. This report describes various ways of deducing information on path latitude and electron concentration from whistler nose frequency and travel time at the nose. The whistlers are assumed to be received on the ground. When the nose is not visible on a spectrogram, the nose frequency and travel time at the nose can be extrapolated from the visible portion of the whistler trace by the techniques such as those developed by Smith and Carpenter [1961], Dowden and Allcock [1971] and by Bernard [1971].

This work is an extension of the work of Angerami [1966], who refined the whistler technique by obtaining empirical support for a diffusive-equilibrium model of the field-line distribution of electrons inside the plasmapause and an idealized collisionless model outside the plasmapause. The basic approaches and formulations used here are similar to his, and many of the ideas for improvements developed out of conversations with him.

For the theory of whistler propagation and other background material, the reader is referred to a book by Helliwell [1965] or a review paper by Carpenter and Smith [1964]. For a detailed development of models of electron distribution along geomagnetic field lines, see Angerami and Thomas [1963] and Angerami [1966].

Figure 1 shows an example of a multi-component whistler train. At the top is a frequency-time spectrogram of a recording from Eights,Antarctica. The causative sferic is identified and marked t = 0. The middle panel shows a tracing of three nose whistler components, while the bottom panel is a sketch of their field line paths. The purpose of this report is to develop methods of determining accurately and economically the path latitude

EI 6 JUN 63 ~0150LT
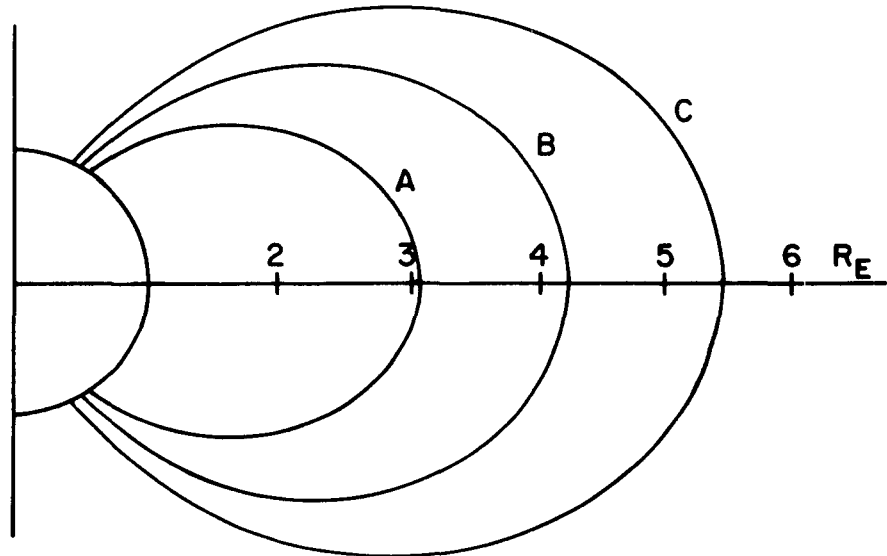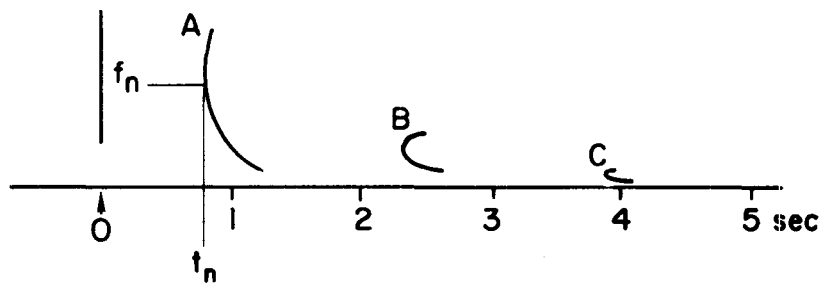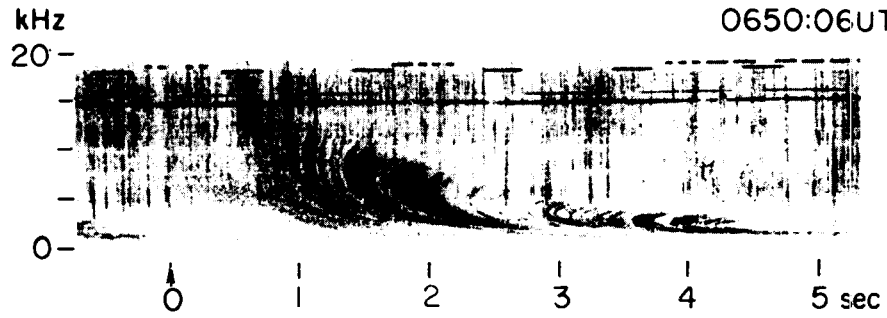
Figure 1. An example of a multicomponent whistler recorded at Eights, Antarctica on June 6, 1963. The top panel is a frequency-time spectrogram showing many discrete whistler components all excited by a sferic at t = o. The middle panel is a tracing of 3 whistler components and the causative sferic. The bottom panel is a sketch of corresponding field-aligned propagation paths in the magnetosphere.

and electron concentration along the path from whistler parameters f_n and t_n.

B. THE WHISTLER INTEGRAL

In the case of longitudinal propagation of a whistler wave, the refractive index μ is given by

$$\mu = \left[1 + \frac{f_p^{\,2}}{ff_H\left(1 - \frac{f}{f_H}\right)} \right]^{1/2} \tag{1.1}$$

where f is the wave frequency, f_p the plasma frequency, and f_H the electron gyrofrequency. If $\mu \gg 1$, calculations can be greatly simplified by neglecting the 1 inside the bracket. This is a good approximation inside the plasmapause, where plasma frequencies are relatively high. For example, assume an equatorial electron concentration of 100 cm^{-3} at $L = 4$ ($f_p = 90$ kHz and $f_H = 13.5$ kHz.) At $f = 0.5\, f_H$, $\mu \cong 25$ and the error introduced by neglecting the 1 is less than 0.1%. In the plasma trough region beyond the plasmapause, the error is larger because of low plasma densities there. Angerami [1966] examined in detail the validity of this approximation when applied to 'knee whistlers' propagating just outside the plasmapause. He found that on an occasion when the equatorial electron concentration was as low as 2 cm^{-3} at $L = 4$, the above approximation introduced an error of $\sim 40\%$ in the calculated electron concentration. When electron concentrations are that low, errors due to other factors which are negligible under normal conditions also become serious (see Chapter 6). For extremely low electron concentrations, all sources of error including the 1 in Eqn. (1.1) should be carefully evaluated.

The refractive index is then written as

$$\mu = \frac{f_p}{f^{1/2} f_H^{1/2} \left(1 - \dfrac{f}{f_H}\right)^{1/2}} \quad ,$$

and the group refractive index as

$$\mu_G = \frac{d}{df}(\mu f) = \frac{f_p}{2f^{1/2} f_H^{1/2} \left(1 - \dfrac{f}{f_H}\right)^{3/2}}$$

The travel time of a whistler wave propagating along a geomagnetic field line is

$$t(f) = \frac{1}{2c} \int \frac{f_p}{f^{1/2} f_H^{1/2} \left(1 - \dfrac{f}{f_H}\right)^{3/2}} \, ds \qquad (1.2)$$

where c is the speed of light in free space and ds is an element of path length along the field line. The integral is over the entire length of the field line path. If a centered dipole approximation is used for the earth's magnetic field, f_H is a simple function of s (see Appendix). In order to express f_p as a function of s, however, it is necessary to adopt a model of the plasma distribution along field lines. Since the exact distribution along a field line at a given time is not known, the choice of a model is somewhat arbitrary. The results, however, are remarkably insensitive to the choice of models as will be seen in the next chapter.

The solutions of Eq. (1.2) show that t has a minimum value t_n at some frequency f_n for all reasonable models of f_p. In other words, Eq. (1.2) describes the shape of a nose whistler. Our task is to establish quantitative relationships between (f_n, t_n) and (f_H, f_p), so that the information in the whistler path latitude and on electron concentration

- 5 -

along the path can be determined from observed whistler parameters. The integral in Eq. (1.2) can be evaluated analytically only for extremely simple models of f_p, i.e. f_p = constant or $f_p \propto f_H^{1/2}$ (gyrofrequency model). For more realistic models adopted in this report, numerical techniques must be used.

Because of the gyrofrequency term in Eq. (1.2), electrons at low altitudes such as in the ionospheric F2 region make a relatively small contribution to the total integral, in spite of their large concentrations. It will be shown in Chapter 6 that if the plasma is in diffusive equilibrium along magnetic field lines, nearly 80% of the propagation delay occurs within 30° of the magnetic equator. For this reason, whistlers can be used to measure electron concentrations near the equatorial plane with great accuracy, without a precise knowledge of concentration profiles in the F region and the topside ionosphere up to several thousand kilometers. Further discussion on this point follows in Chapter 6.

C. AN OUTLINE OF STRATEGY

This section contains an outline of the methods of attacking the problem and of the organization of the remainder of this report.

As pointed out in the previous section, the ionospheric F2 region, with its large electron concentrations and great variability, makes a relatively small contribution to the whistler integral. Therefore, the conjugate path segments through the F region will be treated as a small correction term. An arbitrary boundary is drawn at 1000 km altitude, and the path of integration in Eq. (1.2) is divided into the 'ionospheric' part below 1000 km and the 'magnetospheric' part above (this will serve as the definition of the ionosphere and the magnetosphere throughout this report, unless otherwise stated). Equation (1.2) is then rewritten as

$$t(f) = \frac{1}{2c} \int_{mag} \frac{f_p}{f^{1/2} f_H^{1/2} \left(1 - \frac{f}{f_H}\right)^{3/2}} \, ds + \frac{1}{2c} \int_{iono} \frac{f_p}{f^{1/2} f_H^{1/2} \left(1 - \frac{f}{f_H}\right)^{3/2}} \, ds$$

(1.3)

The two integrals are illustrated schematically in Figure 2. The dashed curves 1 and 2 represent the ionospheric and the magnetospheric contributions, respectively, and the solid curve 3 is the sum of the two. The relative contribution by the ionosphere is exaggerated for the purpose of illustration. An actual whistler with observed f_n and t_n would have f_n' and t_n' if it had traveled through the magnetospheric path only.

In Chapter 2, the ionosphere is ignored, and methods are developed to obtain the whistler path latitude and electron concentration along the path from f_n' and t_n'. In Chapter 3, the ionospheric part of Eq. (1.3) is considered, and methods are developed to obtain f_n' and t_n' from f_n and t_n. If t_n is measured from the sferic on a whistler spectrogram (see Figure 34), the subionospheric propagation time must be taken into account. This is discussed in Chapter 4. Chapter 5 summarizes the results with step by step instructions for calculating magnetospheric parameters from f_n and t_n. In Chapter 6, uncertainties in the whistler method are discussed in detail and a few suggestions are made for future improvements. Finally for purposes of easy reference an appendix presents a collection of formulas and graphs involving some frequently used parameters of a dipole geomagnetic field.
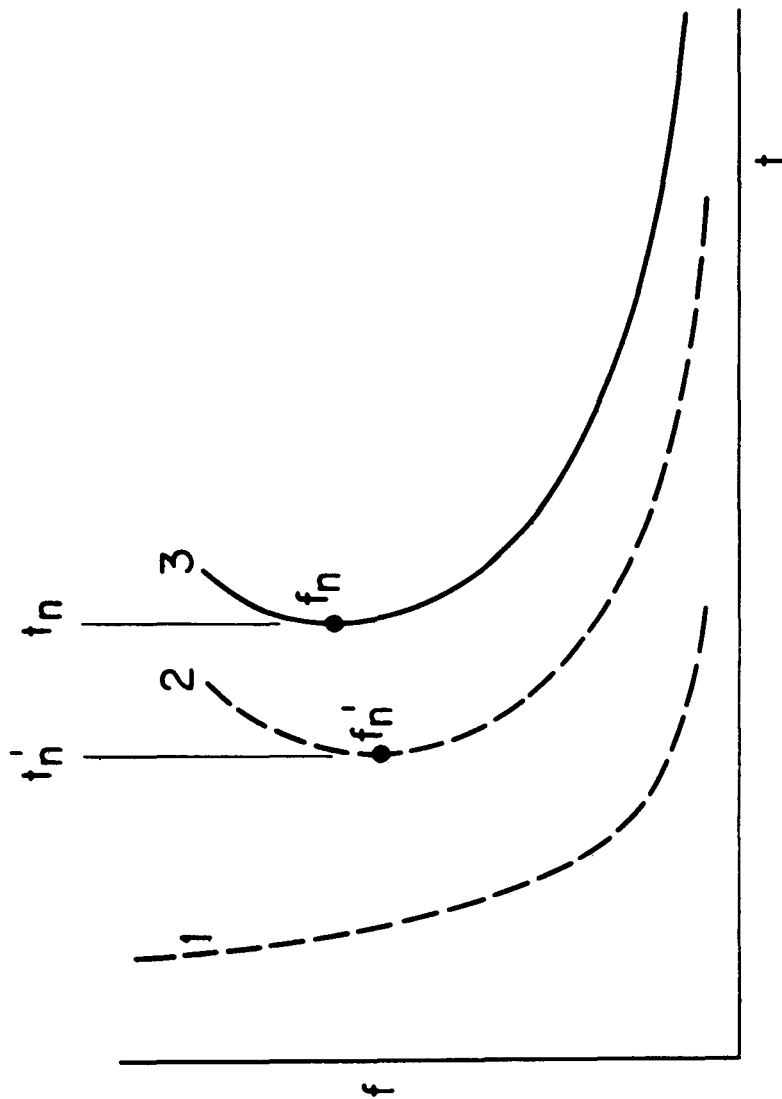
Figure 2. A sketch illustrating whistler dispersion in the ionosphere and magnetosphere. The dashed curve 1 representing the ionospheric contribution is shown exaggerated for illustration. The dashed curve 2 represents the travel time through the magnetosphere and the solid curve 3 is the sum of 1 and 2.

II. CALCULATIONS AND RESULTS

A. OUTLINE OF THE CHAPTER

In this chapter, we consider whistler wave propagation in the magneto-sphere from 1000 km altitude in one hemisphere to the 1000 km level in the conjugate hemisphere. We assume that the magnetosphere is symmetrical about the equator and write

$$t(f) = \frac{1}{c} \int_{1000\ km}^{equator} \frac{f_p}{f^{1/2} f_H^{1/2} \left(1 - \frac{f}{f_H}\right)^{3/2}}\ ds \qquad (2.1)$$

Several different models for the distribution of f_p along field lines will be adopted in the next section. With a model for f_p, the integral in Eq. (2.1) can be evaluated numerically for a given magnetic field line. The wave frequency f is varied in search for the frequency f_n' which gives the minimum time delay t_n'. This is repeated for different magnetic field lines (L = 2, 3, 4, etc., L being McIlwain's parameter [McIlwain, 1961] and for different models of plasma distribution along the field lines. From these results, relationships will be found between the whistler parameters f_n' and t_n' and the parameters of the medium, L and f_p. The results will be presented in various forms so that, depending on the desired accuracy, the whistler path latitude and the electron concentration along the path can be determined by the most economical means.

We will briefly examine the properties of Eq. (2.1) and justify in advance the form in which the results are presented in Sections 2-D, E and G. Calculations in the next section will show that f_n' is approximately proportional to the minimum electron gyrofrequency along the propagation path, f_{Heq}, so that

$$f_{Heq} = Kf'_n \qquad\qquad (2.2)$$

where K is a quasi-constant that varies slowly with f'_n and models of f_p. The L-value corresponding to f_{Heq} for a dipole field can be easily obtained from the relation,

$$L = \left(\frac{f_{Hoeq}}{f_{Heq}}\right)^{1/3} = \left(\frac{8.736 \times 10^5}{f_{Heq}}\right)^{1/3}$$

(f_{Hoeq} is the electron gyrofrequency at the earth's equator and its numerical value given above corresponds to a magnetic field strength of 0.312 gauss.) Since the bulk of the whistler propagation delay occurs in the equatorial region where f_p and f_H are slow functions of s, Eq. (2.1) can be roughly approximated by a simple algebraic equation,

$$t(f) = \frac{f_{peq} \, S_1}{c \, f^{1/2} f_{Heq}^{1/2} \left(1 - \frac{f}{f_{Heq}}\right)^{3/2}}$$

where f_{peq} is the plasma frequency at the equator, and S_1 the path length between 1000 km altitude and the equator. At the nose frequency f'_n, it follows from Eq. (2.2) that the quantity inside the parentheses $1 - \frac{f'_n}{f_{Heq}}$ is very nearly constant. Since S_1 is roughly proportional to L and $f_{Heq} \propto L^{-3}$, we can write

$$t'_n(f'_n) \propto \left(\frac{n_{eq} L^5}{f'_n}\right)^{1/2}$$

where n_{eq} is electron concentration at the equator. For a given field line

distribution model, n_{eq} is proportional to electron concentration at 1000 km altitude n_1. Therefore, we can also write

$$t'_n(f'_n) \propto \left(\frac{n_1 L^5}{f'_n}\right)^{1/2}$$

The above two equations can be written

$$n_{eq} = K_{eq} \frac{f'_n {t'_n}^2}{L^5} \qquad (2.3)$$

and

$$n_1 = K_1 \frac{f'_n {t'_n}^2}{L^5} \qquad (2.4)$$

where K_{eq} and K_1 are quasi-constants varying slowly with f'_n and electron concentration models.

A very useful parameter in studying the magnetosphere is tube content, the total number of electrons in a tube of force. For the purpose of defining tube content the tube of force is chosen to have 1 cm^2 cross-sectional area at 1000 km altitude and to extend to the dipole equatorial plane. Tube content is then

$$N_T = \int n \, A \, ds$$

where n is the electron concentration and A the cross-sectional area of the tube of force. The integral extends from 1000 km altitude to the equator. Since most of the tube volume is near the equator, we expect tube content to be roughly proportional to $n_{eq} A_{eq} S$. Since S is roughly proportional to L, and $A_{eq} \propto \frac{1}{f_{Heq}} \propto L^3$, N_T varies roughly as $n_{eq} L^4$.

SEL-71-058

Using Eq. (2.3), we write

$$N_T = K_T \; \frac{f_n^{\prime} t_n^{\;2}}{L} \tag{2.5}$$

where K_T is again a quasi-constant. In Eq. (2.2) through (2.5), the K's are nearly constant so that once they are evaluated accurately as a function of $f_n^{\prime}$ and for various electron concentration models, their value can be read from graphs or approximated by empirical formulae with a high decree of precision.

B. ELECTRON CONCENTRATION MODELS

Four different models of electron distribution along magnetic field lines will be used in the next section. Angerami and Carpenter [1966] compared whistler results with electron concentrations at 1000 km altitude measured by the topside sounder aboard the Alouette I satellite, and found that a diffusive equilibrium model is a good approximation inside the plasmapause where equatorial electron concentrations are 10^2-10^3 cm^{-3}. Outside the plasmapause, where equatorial electron concentrations are $\sim 10^0$-10^1 cm^{-3}, collisions may not be sufficiently frequent to establish a diffusive equilibrium distribution. Angerami and Carpenter [1966] showed that outside the plasmapause, an idealized collisionless model was more appropriate than diffusive equilibrium model. However, the choice of an appropriate model for low concentration regions remains to be put on firm ground.

The idealized collisionless model to be used in this report probably represents an extreme case as compared to most circumstances that occur outside the plasmapause. The actual distribution may fall somewhere between a diffusive-equilibrium and collisionless distribution. Because of the dynamic nature of the plasmapause region, some flux tubes undergo

large fluctuations in electron concentration, and the field line distribution must change accordingly. For example, during magnetic storms when the plasmapause moves inward, a collisionless model may temporarily be adequate to describe the low concentration region outside the storm-time plasmapause. During the recovery phase, the depleted flux tubes fill gradually from the ionosphere, and the field line distribution must become more like a diffusive equilibrium distribution as the electron concentration increases. For a distribution that might exist during the transition, we will consider a hybrid model in which the plasma is assumed to be in diffusive equilibrium from 1000 km altitude up to 30° in dipole latitude, but no collisions are allowed within 30° of the equator.

In the fourth model to be considered, $n \propto r^{-4}$ along a field line, where r is the geocentric distance. As pointed out by Angerami [1966], this model closely approximates the collisionless model adopted here, and it has the advantage of computational simplicity. There now follows a description of each model and the abbreviations by which each model will be identified throughout this report.

1. Diffusive Equilibrium (DE model)

Detailed treatment of the problem of a multi-component plasma in hydrostatic equilibrium along geomagnetic field lines can be found elsewhere in the literature (see, for example, Angerami and Thomas [1963] or Angerami [1966]). Here we adopt Angerami's [1966] formulation as given by his Eqs. (2.4) through (2.7).* The electron concentration is given by

---

*Angerami stated in a private communication that his Eq. (2.7b) is in error and should read

$$a = r_o \left[1 - \frac{1}{R} - \frac{\Omega^2 r_o^2}{2g_o} \left(R^2 \cos^2\theta - \cos^2\theta_o \right) \right]$$

$$n = n_1 \left[\sum_i \xi_{i1} \exp\left(-\frac{z}{H_i}\right)\right]^{1/2} \tag{2.6}$$

$$z = r_1 - \frac{r_1^2}{r} - \frac{\Omega^2}{2g_1} \left(r^2 \cos^2\phi - r_1^2 \cos^2\phi_1 \right) \tag{2.7}$$

$$H_i = \frac{kT}{m_i g_1} \tag{2.8}$$

where

ξ = fractional abundance of ionic species

r = geocentric distance

Ω = angular rotational speed of the earth

g = acceleration of gravity

ϕ = dipole latitude

k = Boltzman's constant

T = temperature

m = mass

The subscript i refers to the ith ionic species (O^+, He^+ and H^+), and

the subscript 1 refers to the reference level at 1000 km altitude. Figure

3 illustrates the coordinates and the symbols used in Eqs. (2.6) through

(2.8). The geopotential height z takes into account variations of gravi-

tational force with distance and the centrifugal force due to corotation

of the plasma with the earth. The centrifugal force term becomes impor-

tant only for $L \gtrsim 6$ [Angerami, 1966]. For simplicity, it is assumed that

the magnetospheric plasma corotates with the earth at all latitudes of

interest here. At high latitudes, particularly outside the plasmapause,
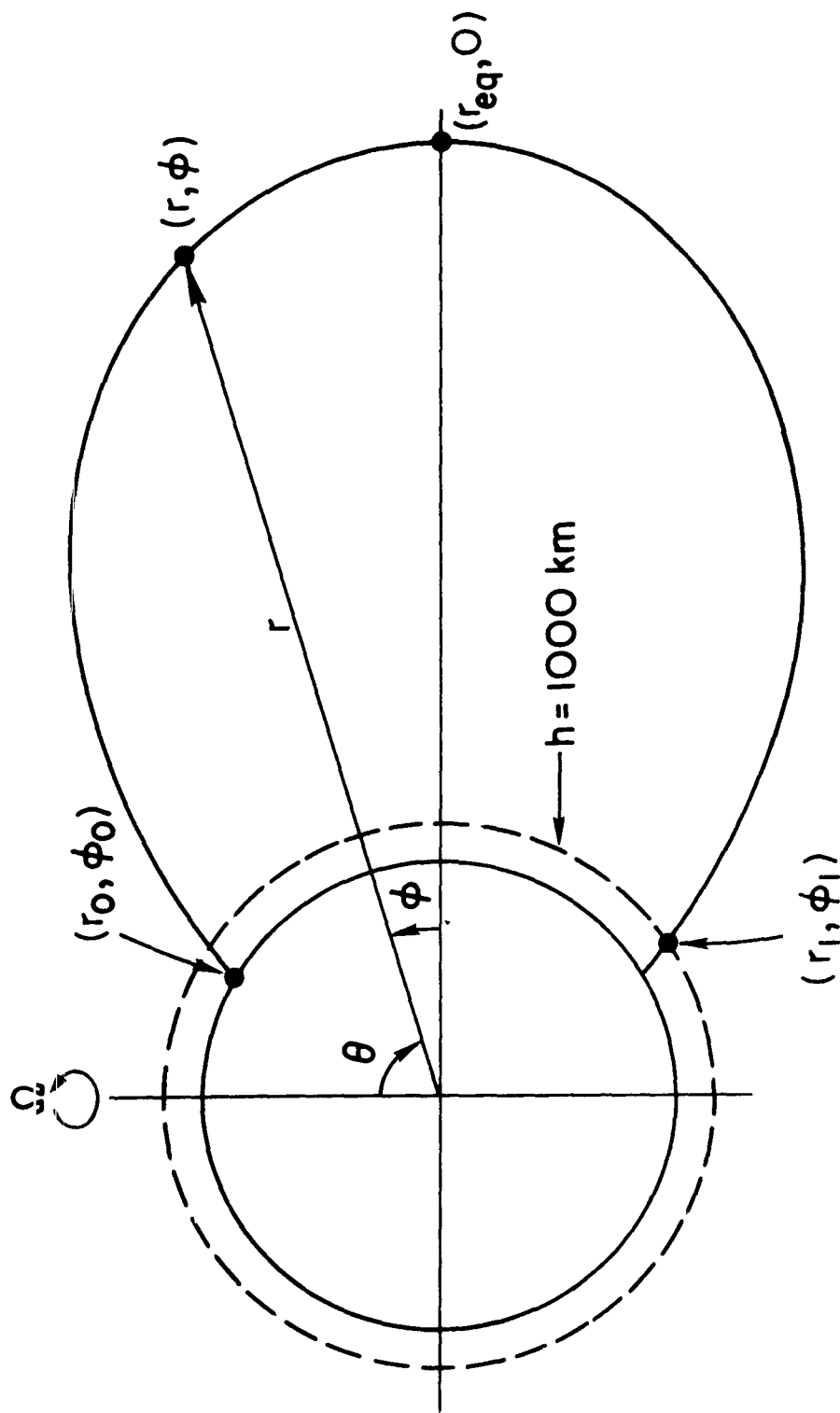
Figure 3. A sketch of the earth and a magnetic field line illustrating the coordinate system and symbols used in this report.

15

this may not be a good assumption. The effects on the field-line distribution of plasma of centrifugal force associated with convective motions in the outer magnetosphere need further investigation.

Equations (2.6) through (2.8) show that electron concentration depends on the temperature and the ionic composition at the reference level as well as on geometric factors. We will adopt several different combinations of the temperature and ionic composition at 1000 km altitude as summarized in Table 1. It is assumed that $T = T_e = T_i$ and that T is constant with altitude. Since whistlers essentially measure electron concentrations near the equator, it is preferable to normalize n to the equatorial concentration rather than to the concentration at the base of the magnetosphere. Equation (2.6) is rewritten as

$$
n = n_{eq} \left[\frac{\sum_i \xi_{il} \exp\left(-\frac{z}{H_i}\right)}{\sum_i \xi_{il} \exp\left(-\frac{z_{eq}}{H_i}\right)} \right]^{1/2}
\tag{2.9}
$$

where the subscript eq refers to the dipole equator. Figure 4 illustrates how electron concentration varies along lines of force for different L-values according to the DE-1 model (see Table 1). The distance along the field line S is measured from the equatorial plane, and the terminal points of the curves correspond to the base level at 1000 km altitude. Near the base level, O^+ and He^+ concentrations decrease rapidly with altitude and H^+ soon becomes the major ion. Beyond that point, electron concentration varies slowly with distance because of the large plasma scale height. If the temperature or ionic composition is changed, the curves in Figure 4 remain essentially unchanged at distances more than a few hundred kilometers above the base level. The only significant changes in electron

TABLE I. PARAMETERS OF DIFFUSIVE EQUILIBRIUM MODELS

Abbreviation	Temperature	Composition at 1000 km.		
		O^+	H^+	He^+
DE- 1	$1600^O K$	90%	8%	2%
DE- 2	3200	90	8	2
DE- 3	1600	50	40	10
DE- 4	800	50	40	10
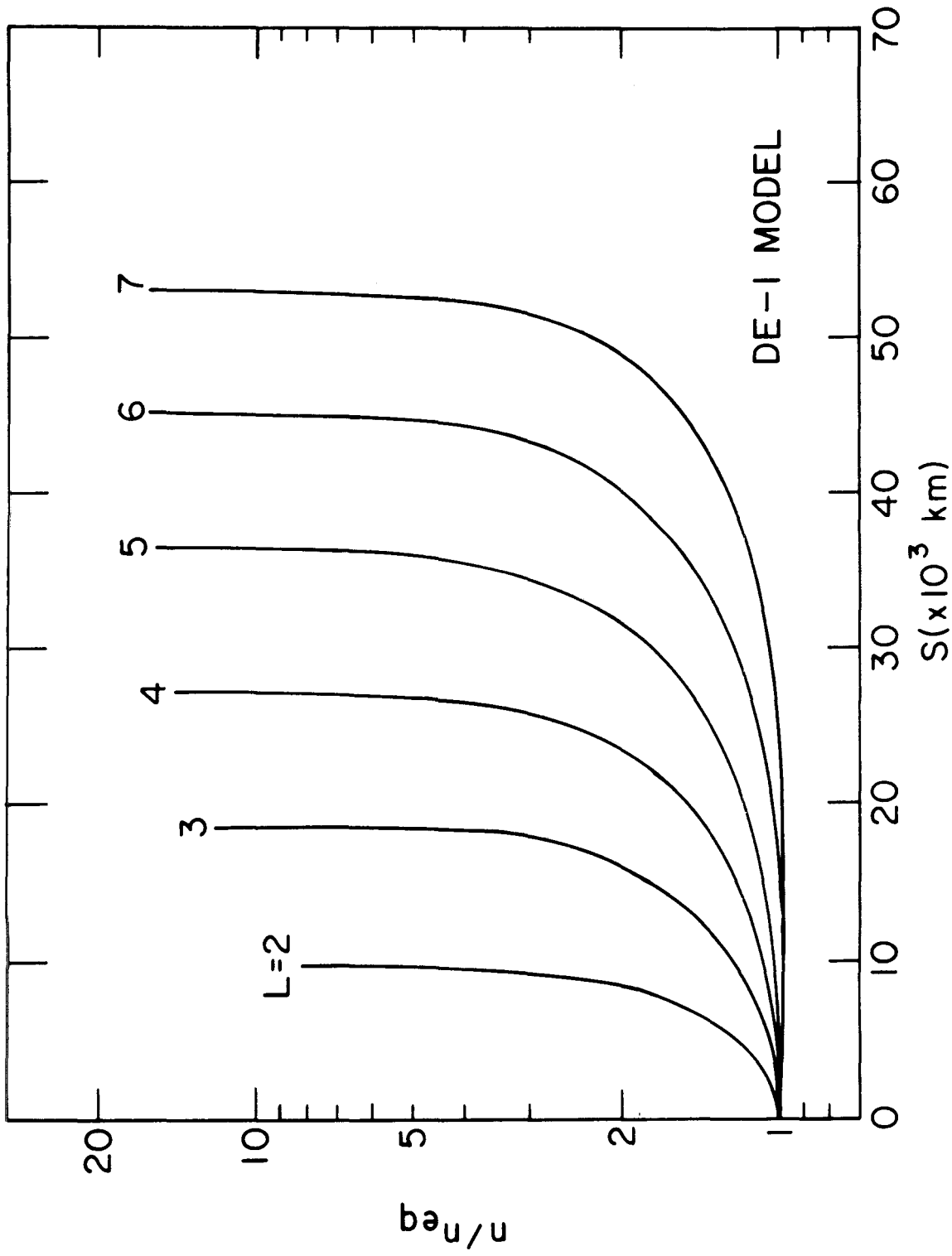
Figure 4. A plot of normalized electron concentration versus distance along field lines at several L values according to a diffusive equilibrium model. ($T_i = T_e = 1600^\circ$K, 90% O^+, 8% H^+ and 2% He^+ at 1000 km) the arc length is measured from the equator, and the end points of the curves correspond to 1000 km altitude.

distribution occur where O^+ and He^+ concentrations are important.

2. Collisionless Model (CL model)

We adopt the formulation of Angerami [1966] for the distribution of a proton-electron plasma along lines of force above 1000 km altitude under the influence of gravitational force, a charge separation electric field, and centrifugal force due to corotation with the earth, but not the effects of collisions between particles. The concentration is given by

$$ n = n_1 \left\{ \exp\left(-\frac{z}{2H}\right) - \left(1 - \frac{B}{B_1}\right)^{1/2} \exp\left[-\frac{z}{2H\left(1 - \frac{B}{B_1}\right)}\right] \right\} \qquad (2.10) $$

where B is the magnetic field strength and z and H are given by Eqs. (2.7) and (2.8), respectively. Eliminating n_1 in Eq. (2.10),

$$ n = n_{eq} \frac{\left\{ \exp\left(-\frac{z}{2H}\right) - \left(1 - \frac{B}{B_1}\right)^{1/2} \exp\left[-\frac{z}{2H\left(1 - \frac{B}{B_1}\right)}\right] \right\}}{\left\{ \exp\left(-\frac{z_{eq}}{2H}\right) - \left(1 - \frac{B_{eq}}{B_1}\right)^{1/2} \exp\left[-\frac{z_{eq}}{2H\left(1 - \frac{B_{eq}}{B_1}\right)}\right] \right\}} \qquad (2.11) $$

We assume a constant temperature of $3200^\circ K$ for both electrons and protons. Figure 5 shows the normalized electron concentration as a function of distance along lines of force for several L-values. The CL model differs from DE models in presenting a much faster variation in electron concentration with distance, particularly near the equator.

3. $n \propto r^{-4}$ Model (R-4 model)

This model approximates the collisionless model very closely, and
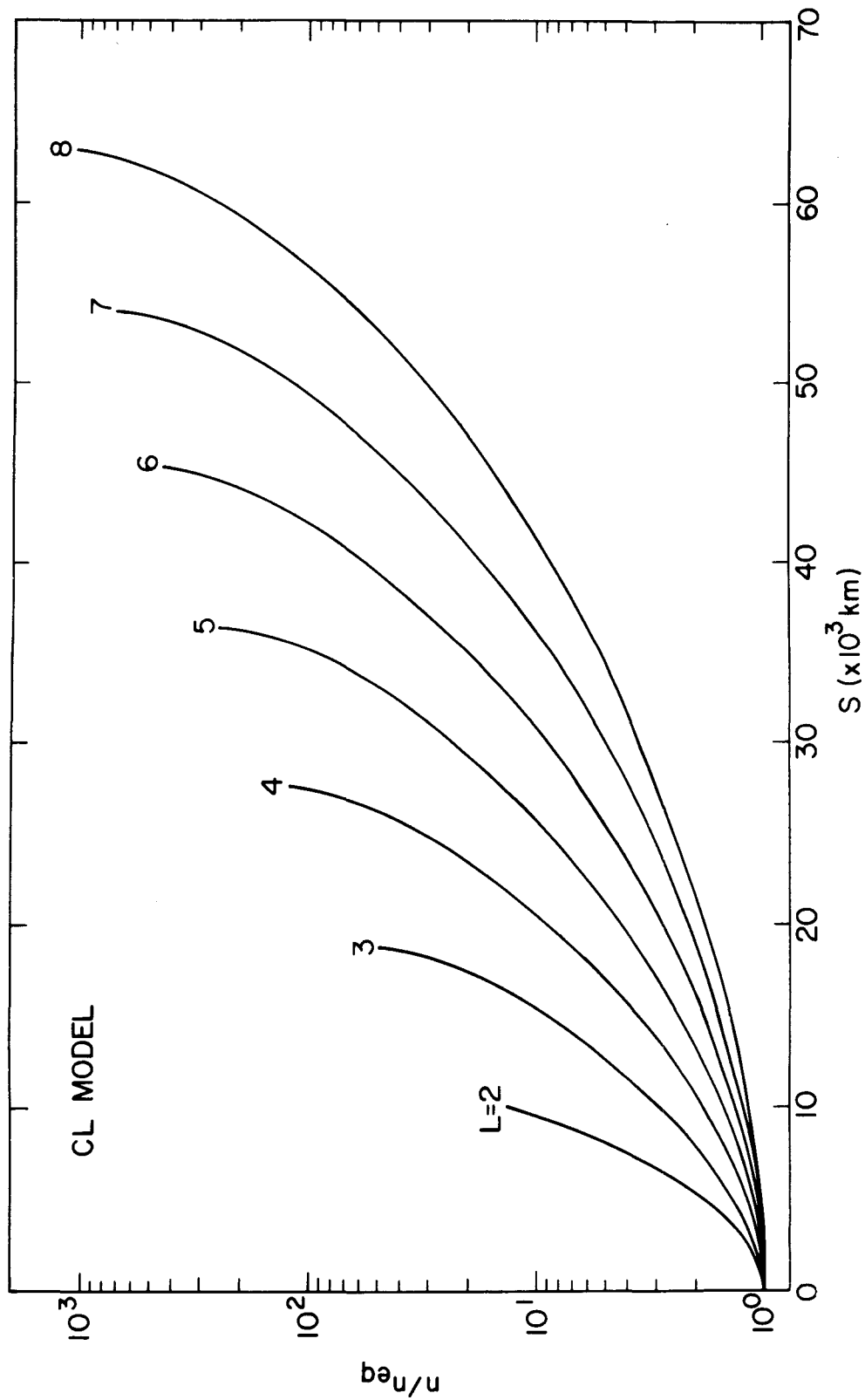
Figure 5. A plot of normalized electron concentration in a format similar to that of Figure 4 but according to an idealized collisionless model.

has the advantage of being much simpler.

$$n = n_1 r_1^4 r^{-4} \qquad\qquad (2.12)$$

or

$$n = n_{eq} r_{eq}^4 r^{-4} \qquad\qquad (2.13)$$

4. Hybrid Model (HY model)

This model combines a diffusive equilibrium model and a collision-less model. We apply DE-2 model (90% O^+, 2% He^+ and 8% H^+ at 1000 km and $T = 3200^O$K) from 1000 km altitude up to 30° dipole latitude and CL model (collisionless H^+ and electrons at 3200^OK) from 30° to the dipole equator. This is an attempt to recognize the fact that when the magneto-spheric concentrations are low, the plasma may not be in diffusive equi-librium, but at the same time, it is unrealistic to assume no collisions down to 1000 km altitude, as is done in the CL model. The electron con-centration according to this hybrid model is illustrated in Figure 6.

The models described above are listed on page xi for quick reference.

C. CALCULATIONS

Eq. (2.1) is rewritten as

$$t(f) = \frac{1}{c} \int_0^{\phi_1} \frac{f_p}{f^{1/2} f_H^{1/2} (1 - \frac{f}{f_H})^{3/2}} \frac{ds}{d\phi} d\phi \qquad\qquad (2.14)$$

where ϕ is the magnetic latitude, and ϕ_1 the magnetic latitude at 1000 km altitude. For a dipole field (see Appendix),

$$r = r_o L \cos^2\phi \qquad\qquad\text{and}\qquad \frac{dr}{d\phi} = - 2r_o L \cos\phi \sin\phi$$
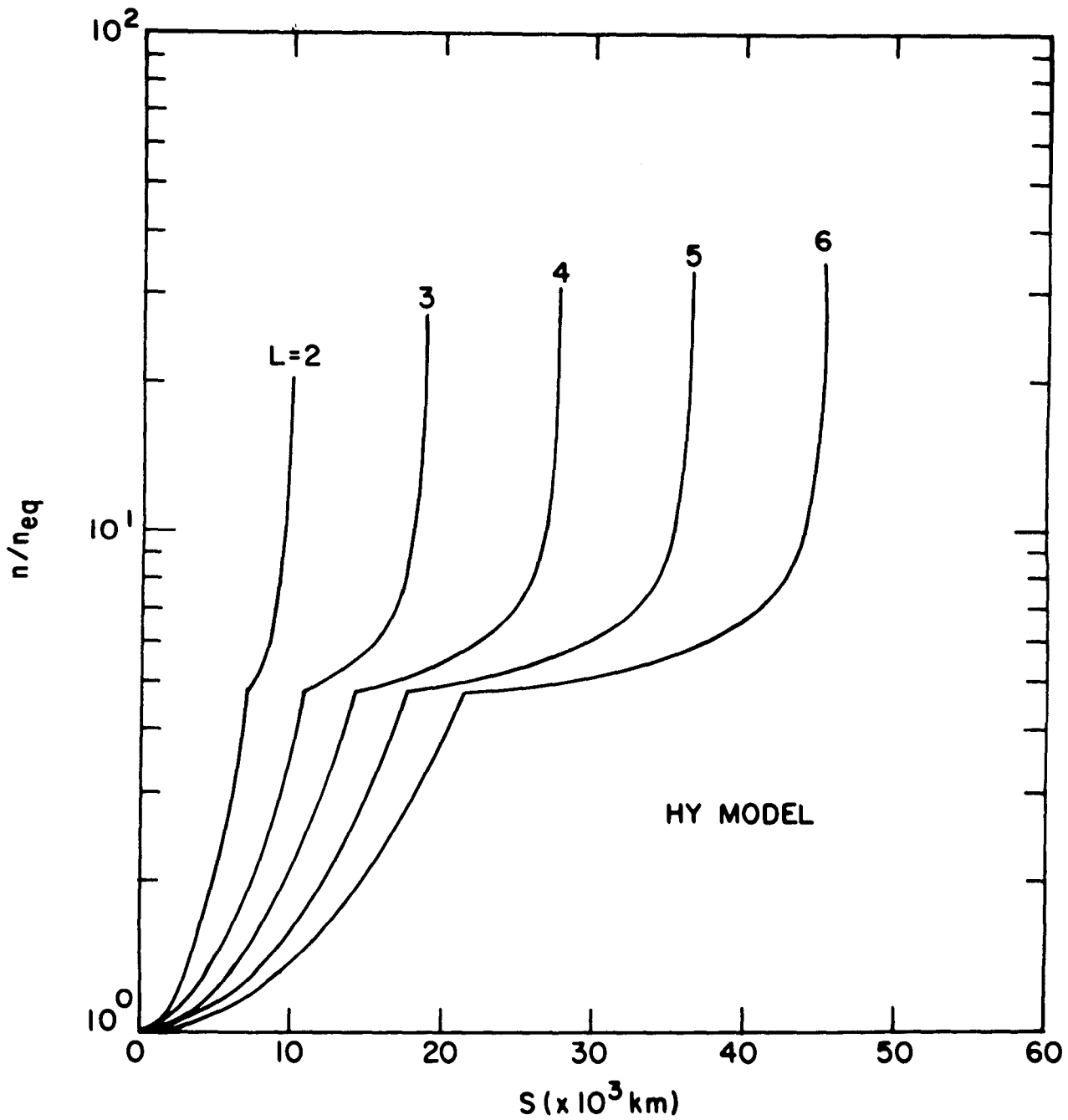
Figure 6. A plot of normalized electron concentration
in a format similar to that of Figure 4 but
according to a hybrid model (see the text for details).

so that

$$\frac{ds}{d\phi} = \left[\left(\frac{dr}{d\phi}\right)^2 + r^2\right]^{1/2} = r_o L \cos\phi \left(1 + 3 \sin^2\phi\right)^{1/2} \qquad (2.15)$$

The electron gyrofrequency can be expressed as (see Appendix)

$$f_H = f_{Hoeq} \left(\frac{r_o}{r}\right)^3 \left(1 + 3 \sin^2\phi\right)^{1/2} \qquad (2.16)$$

where f_{Hoeq} is the electron gyrofrequency at the earth's equator, or

8.736×10^5 Hz. The plasma frequency is

$$f_p = \alpha \; n^{1/2} = \alpha \left[n_{eq} \; \lambda \; (\phi)\right]^{1/2} \qquad (2.17)$$

where α is a constant, and $\lambda(\phi)$ represents various electron concentration models described in the previous section. The upper limit in the integration ϕ_1 is obtained from the relation

$$\cos\phi_1 = \left(\frac{r_1}{r_o L}\right)^{1/2} \qquad (2.18)$$

Using Eq. (2.15) through (2.17), Eq. (2.14) can be written as

$$t(f) = \beta \; n_{eq}^{1/2} \int_0^{\phi_1} \Im(\phi, \; f)d\phi = \beta \; n_{eq}^{1/2} I(f) \quad (2.19)$$

where β is a constant.

For a given field line, say $L = 4$, ϕ_1 is evaluated to the nearest even tenth of a degree (the maximum error in ϕ_1 is then 0.1^o). The integral is evaluated numerically by Simpson's rule with $\Delta\phi = 0.1^o$, and by

iteration, we search for the wave frequency f_n' which gives the minimum

value of the integral $I(f_n')$. The iteration is continued until the error

in f_n' is reduced to less than 0.2%. This procedure is repeated for various

L-values and various electron concentration models. The results are tab-

ulated in the second column of Tables 2 through 8 in the next section.

Following the reasoning given in Section 2A, we express the numerical

results in the same form as in Eqs. (2.2) through (2.5). The values of

various K's are also tabulated in Tables 2 through 8.

Eq. (2.19),

$$n_{eq} = \left[\frac{t_n'}{\beta I(f_n')} \right]^2$$

·when expressed in the form of Eq. (2.3), yields

$$K_{eq} = \frac{L^5}{f_n' \left[\beta I(f_n') \right]^2}$$

The electron concentration at 1000 km altitude is easily calculated from

n_{eq} and the electron concentration model $\lambda(\phi)$:

$$n_1 = n_{eq} \lambda(\phi_1) = K_1 \frac{f_n' t_n'^2}{L^5}$$

K_1 and K_{eq} are then related by

$$K_1 = K_{eq} \lambda(\phi_1)$$

The tube content is

$$N_T = \int_0^{\phi_1} n \, A \, \frac{ds}{d\phi} \, d\phi \qquad (2.20)$$

where A is the cross-sectional area of a tube of force with 1 cm^2 area at

TABLE 2. RESULTS FOR THE DE-1 MODEL

L	f'_n	$K = \dfrac{f_{Heq}}{f'_n}$	$K_{eq} = \dfrac{n_{eq} L^5}{f'_n t'_n{}^2}$	$K_1 = \dfrac{n_1 L^5}{f'_n t'_n{}^2}$	$K_T = \dfrac{N_T L}{f'_n t'_n{}^2}$	$\dfrac{N_T}{n_{eq}}$
2	3.870×10^4	2.821	27.55	227.4	8.924×10^9	5.184×10^9
2.5	2.046×10^4	2.733	24.34	252.2	8.533×10^9	1.369×10^{10}
3	1.195×10^4	2.708	23.58	282.8	8.476×10^9	2.911×10^{10}
4	5.063×10^3	2.696	23.53	333.9	8.560×10^9	9.313×10^{10}
5	2.586×10^3	2.703	24.06	370.5	8.723×10^9	2.266×10^{11}
6	1.493×10^3	2.708	24.70	393.4	8.872×10^9	4.655×10^{11}
7	9.361×10^2	2.721	25.49	407.3	9.041×10^9	8.517×10^{11}
8	6.235×10^2	2.737	26.34	413.1	9.210×10^9	1.432×10^{12}

TABLE 3. RESULTS FOR THE DE-2 MODEL

L	f'_n (Hz)	$K = \dfrac{f_{Heq}}{f'_n}$	$K_{eq} = \dfrac{n_{eq} L^5}{f'^2_n n}$	$K_1 = \dfrac{n_1 L^5}{f'^2_n n}$	$K_T = \dfrac{N_T L}{f'^2_n n}$	$\dfrac{N_T}{n_{eq}}$
2	3.832×10^4	2.850	29.60	158.4	8.998×10^9	4.864×10^9
2.5	2.015×10^4	2.775	26.62	160.3	8.688×10^9	1.275×10^{10}
3	1.177×10^4	2.750	25.74	167.1	8.674×10^9	2.730×10^{10}
4	5.000×10^3	2.730	25.30	178.9	8.785×10^9	8.889×10^{10}
5	2.560×10^3	2.730	25.43	187.3	8.938×10^9	2.197×10^{11}
6	1.478×10^3	2.736	25.72	192.7	9.082×10^9	4.576×10^{11}
7	9.291×10^2	2.741	26.08	195.8	9.211×10^9	8.479×10^{11}
8	6.219×10^2	2.743	26.44	196.6	9.312×10^9	1.443×10^{12}

TABLE 4. RESULTS FOR THE DE-3 MODEL

L	f'_n (Hz)	$K = \dfrac{f_{Heq}}{f'_n}$	$K_{eq} = \dfrac{n_{eq} L^5}{f'_n t'^2_n}$	$K_1 = \dfrac{n_1 L^5}{f'_n t'^2_n}$	$K_T = \dfrac{N_T L}{f'_n t'^2_n}$	$\dfrac{N_T}{n_{eq}}$
2	3.851×10^4	2.836	28.08	103.7	8.945×10^9	5.096×10^9
2.5	2.041×10^4	2.740	24.62	114.1	8.552×10^9	1.357×10^{10}
3	1.195×10^4	2.709	23.70	127.1	8.482×10^9	2.899×10^{10}
4	5.063×10^3	2.696	23.58	149.7	8.568×10^9	9.301×10^{10}
5	2.586×10^3	2.703	24.10	165.9	8.729×10^9	2.264×10^{11}
6	1.493×10^3	2.708	24.73	176.1	8.878×10^9	4.653×10^{11}
7	9.361×10^2	2.721	25.50	182.3	9.045×10^9	8.516×10^{11}
8	6.235×10^2	2.737	26.35	184.8	9.213×10^9	1.432×10^{12}

TABLE 5. RESULTS FOR THE DE-4 MODEL

L	f'_n (Hz)	$K = \dfrac{f_{Heq}}{f'_n}$	$K_{eq} = \dfrac{n_{eq} L^5}{f'_n t'^2_n}$	$K_1 = \dfrac{n_1 L^5}{f'_n t'^2_n}$	$K_T = \dfrac{N_T L}{f'_n t'^2_n}$	$\dfrac{N_T}{n_{eq}}$
2	3.977×10^4	2.746	22.78	196.7	8.793×10^9	6.176×10^9
2.5	2.117×10^4	2.641	19.65	267.1	8.302×10^9	1.650×10^{10}
3	1.239×10^4	2.611	19.10	347.7	8.141×10^9	3.452×10^{10}
4	5.240×10^3	2.605	19.70	501.8	8.106×10^9	1.054×10^{11}
5	2.657×10^3	2.630	21.02	630.1	8.260×10^9	2.456×10^{11}
6	1.523×10^3	2.655	22.49	721.5	8.455×10^9	4.873×10^{11}
7	9.478×10^2	2.687	24.15	780.3	8.705×10^9	8.653×10^{11}
8	6.282×10^2	2.716	25.90	805.7	8.959×10^9	1.417×10^{12}

TABLE 6. RESULTS FOR THE CL MODEL

L	f'_n (Hz)	$K = \dfrac{f_{Heq}}{f'_n}$	$K_{eq} = \dfrac{n_{eq} L^5}{f'^2_n t_n}$	$K_l = \dfrac{n_l L^5}{f'^2_n t_n}$	$K_T = \dfrac{N_T \bar{L}}{f'^2_n t_n}$	$\dfrac{N_T}{n_{eq}}$
2	4.131×10^4	2.644	16.79	2.223×10^2	8.861×10^9	8.444×10^9
2.5	2.259×10^4	2.475	12.34	3.733×10^2	8.375×10^9	2.651×10^{10}
3	1.357×10^4	2.385	10.46	6.061×10^2	8.155×10^9	6.316×10^{10}
4	5.943×10^3	2.297	8.782	1.366×10^3	7.947×10^9	2.317×10^{11}
5	3.102×10^3	2.253	8.052	2.612×10^3	7.831×10^9	6.078×10^{11}
6	1.814×10^3	2.229	7.680	4.453×10^3	7.750×10^9	1.308×10^{12}
7	1.148×10^3	2.220	7.535	7.032×10^3	7.702×10^9	2.454×10^{12}
8	7.710×10^2	2.213	7.481	1.041×10^4	7.653×10^9	4.190×10^{12}

TABLE 7. RESULTS FOR THE R-4 MODEL

L	f'_n (Hz)	$K = \dfrac{f_{Heq}}{f'_n}$	$K_{eq} = \dfrac{n_{eq} L^5}{f'_n t'_n{}^2}$	$K_1 = \dfrac{n_1 L^5}{f'_n t'_n{}^2}$	$K_T = \dfrac{N_T L}{f'_n t'_n{}^2}$	$\dfrac{N_T}{n_{eq}}$
2	4.080×10^4	2.677	18.45	1.648×10^2	7.004×10^9	6.073×10^9
2.5	2.237×10^4	2.500	13.38	2.917×10^2	6.380×10^9	1.863×10^{10}
3	1.347×10^4	2.403	11.13	5.031×10^2	6.136×10^9	4.466×10^{10}
4	5.943×10^3	2.297	8.939	1.277×10^3	5.923×10^9	1.696×10^{11}
5	3.125×10^3	2.236	7.832	2.732×10^3	5.832×10^9	4.654×10^{11}
6	1.842×10^3	2.196	7.140	5.164×10^3	5.780×10^9	1.049×10^{12}
7	1.177×10^3	2.164	6.687	8.960×10^3	5.770×10^9	2.072×10^{12}
8	7.949×10^2	2.147	6.372	1.457×10^4	5.789×10^9	3.721×10^{12}

TABLE 8. RESULTS FOR THE HY MODEL

L	f'_n (Hz)	$K = \dfrac{f_{Heq}}{f'_n}$	$K_{eq} = \dfrac{n_{eq} L^5}{f'^2_n t'_n}$	$K_1 = \dfrac{n_1 L^5}{f'^2_n t'_n}$	$K_T = \dfrac{N_T L}{f'^2_n t'_n}$	$\dfrac{N_T}{n_{eq}}$
2	4.161×10^4	2.624	16.10	329.4	8.924×10^9	8.870×10^9
2.5	2.220×10^4	2.518	13.34	324.5	8.307×10^9	2.432×10^{10}
3	1.303×10^4	2.483	12.43	337.2	8.136×10^9	5.304×10^{10}
4	5.572×10^3	2.450	11.69	363.9	8.066×10^9	1.767×10^{11}
5	2.859×10^3	2.444	11.55	385.5	8.120×10^9	4.395×10^{11}
6	1.658×10^3	2.440	11.54	400.2	8.170×10^9	9.173×10^{11}
7	1.060×10^3	2.403	9.810	436.0	8.238×10^9	2.016×10^{12}

1000 km. It is inversely proportional to the magnetic field strength and can be written as

$$A = \frac{B_1}{B} = \left(\frac{r}{r_1}\right)^3 \left[\frac{1 + 3\ \sin^2\phi_1}{1 + 3\ \sin^2\phi}\right]^{1/2} = \left[\frac{\cos\phi}{\cos\phi_1}\right]^6 \left[\frac{1 + 3\ \sin^2\phi_1}{1 + 3\ \sin\phi}\right]^{1/2}$$

$\frac{ds}{d\phi}$ is given by Eq. (2.15). Substituting these and $n = n_{eq}\lambda(\phi)$ into Eq. (2.20),

$$N_T = \frac{n_{eq}r_o L\ \left(1 + 3\ \sin^2\phi_1\right)^{1/2}}{\cos^6\phi_1} \int_0^{\phi_1} \lambda(\phi)\cos^7\phi\, d\phi \qquad (2.21)$$

The integral is evaluated numerically by Simpson's rule with $\Delta\phi = 0.1^\circ$, and the results are expressed in the form of Eq. (2.5),

$$N_T = K_T\ \frac{f'_n t'^2_n}{L} \qquad (2.5)$$

D. TABULATION OF RESULTS

The results of the calculations are listed in Tables 2 through 8 for various electron concentration models. These tables represent numerical relationships between $(f'_n,\ t'_n)$ and $(L,\ n_{eq},\ n_1,\ N_T)$ for selected L-values. The tables can be stored in a computer, and corresponding relationships for intermediate values of L can be calculated by interpolation. Parabolic interpolations involving t'_n and log (f'_n) are usually satisfactory.

E. GRAPHICAL PRESENTATION OF RESULTS

In this section, the results of calculations are presented in various graphical forms whose usefulness depends on desired speed and accuracy. In Figure 7, f'_n is plotted versus L for a diffusive equilibrium model and
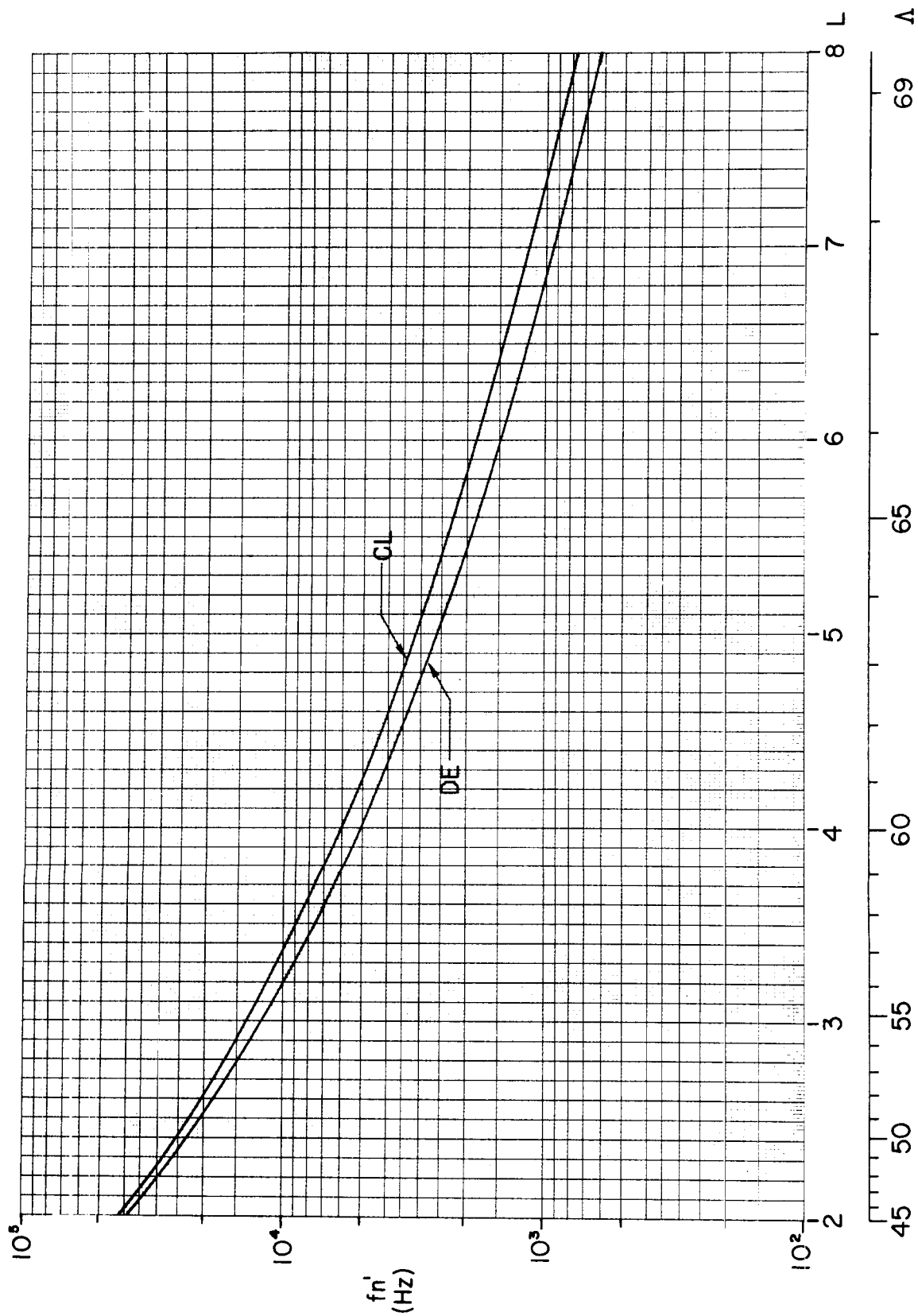
Figure 7. A plot of f_n' versus L and invariant latitude Λ for diffusive equilibrium and collisionless models of field-line plasma distribution.

33

collisionless model. The differences among various DE models and the difference between the CL model and the R-4 model cannot be resolved on plots of this scale. The curve for the hybrid model would lie about mid-way between the two curves shown.

Figures 8 through 11 can be used for a quick determination of n_{eq} and N_T from f_n' and t_n'. Figures 8 and 9 represent a diffusive equilibrium model, and Figures 10 and 11 a collisionless model. Again, the differences among various DE models and the differences between the CL Model and R-4 Model are too small to be shown in plots of this scale. It is not prac-tical to obtain n_1 directly from f_n' and t_n' in the manner of n_{eq} and N_T. The reason is that n_1 depends sensitively on the electron concentration model, and thus will require a large number of graphs, each corresponding to a different model. An alternative approach is to obtain n_1 from n_{eq} or N_T. Figures 12 and 13 show the relationships between n_{eq}, n_1 and N_T for various electron concentration models.

As pointed out in Section 2A, a greater precision can be achieved by the use of quasi-constants K, K_{eq}, K_1 and K_T. Figures 14 through 21 show plots of various K's versus f_n' for various electron concentration models. These values of K's are then used in Eqns. (2.2) through (2.5) to calcu-late L, n_{eq}, n_1, and N_T.

F.   OVERLAY METHOD

For a quick estimate of L, n_{eq} and N_T directly from a whistler spec-trogram, transparent overlays have been devised as illustrated in Figures 22 and 23. These overlays are for a diffusive equilibrium model, but similar overlays can be easily constructed for other models from the re-sults in the previous section. The differences among various DE models
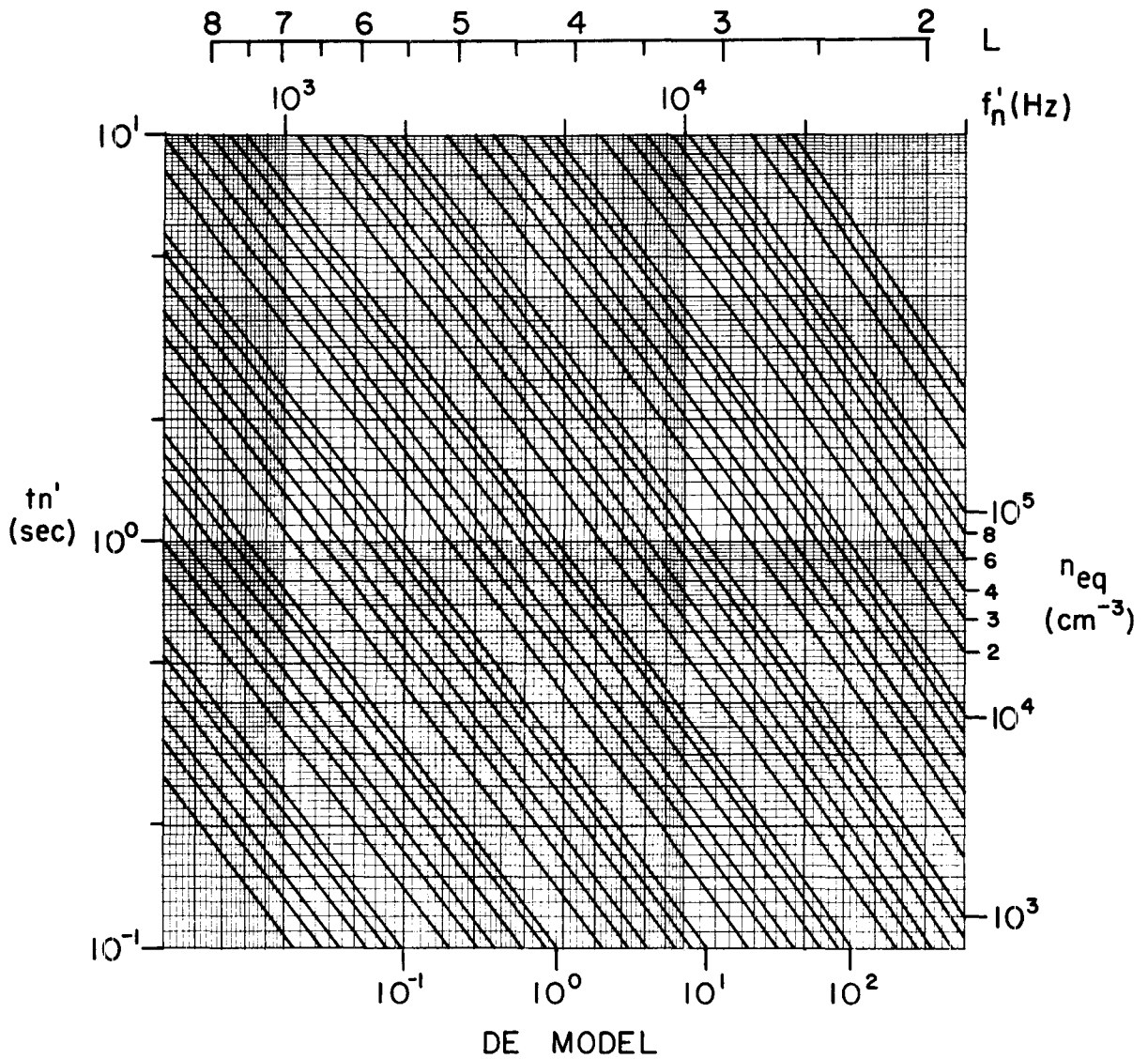
Figure 8. Curves of constant equatorial electron concentration for a diffusive equilibrium model plotted in t_n' - f_n' coordinates. The scale at top shows L-values.
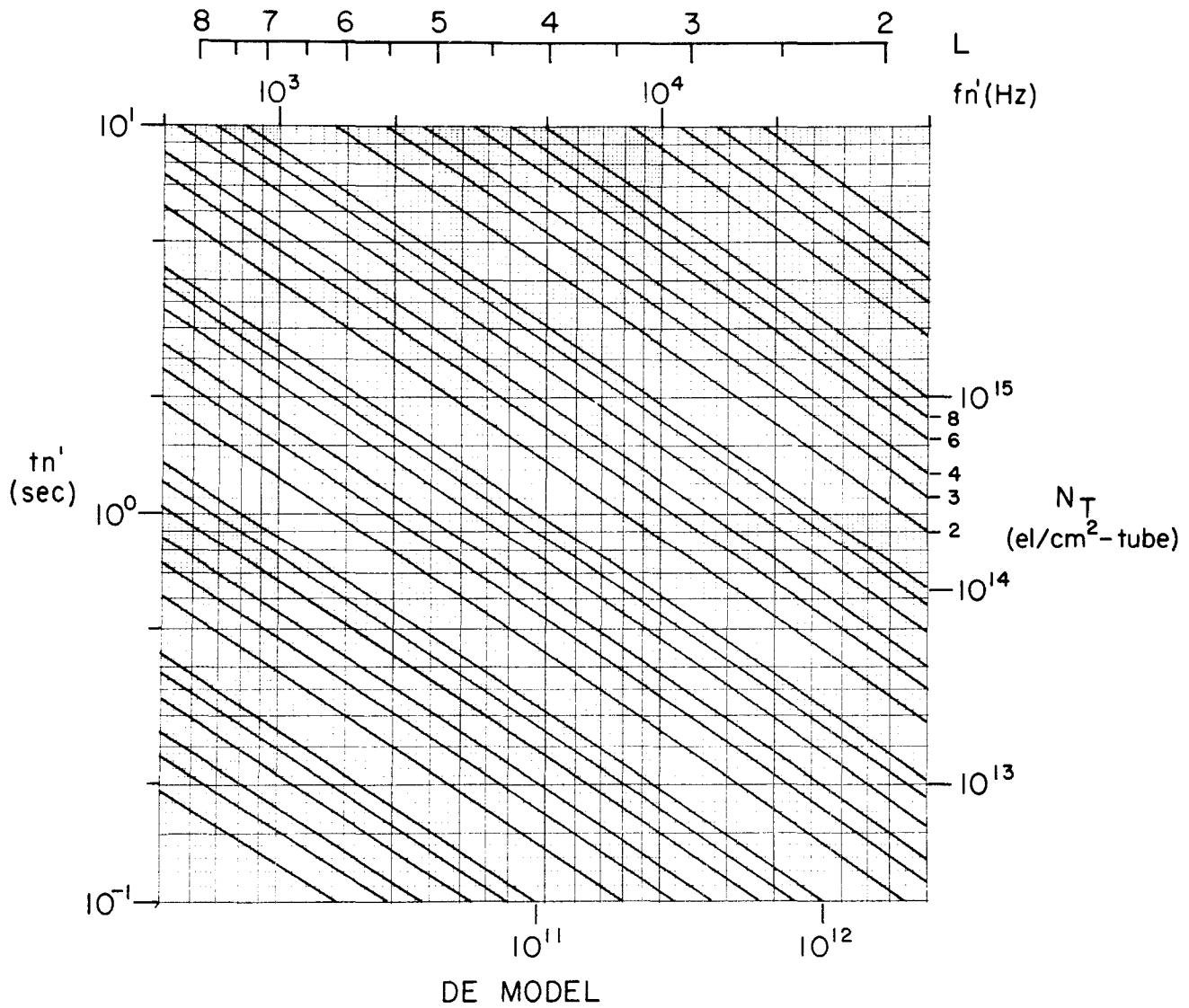
Figure 9. Curves of constant tube content for a diffusive equilibrium model. The format is similar to that of Figure 8.
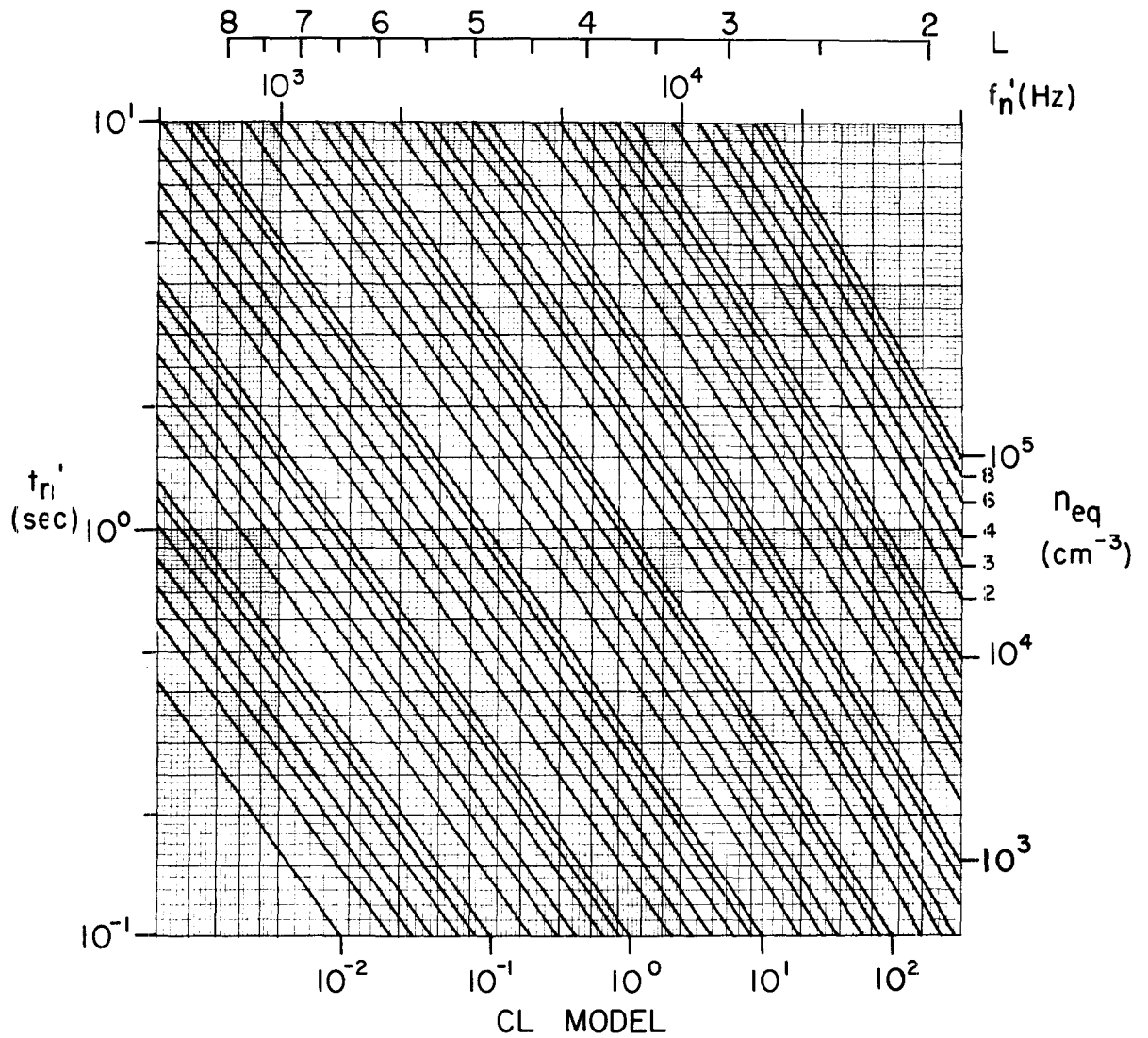
Figure 10. Curves of constant equatorial electron concentration for a collision-
less model. The format is similar to that of Figure 8.
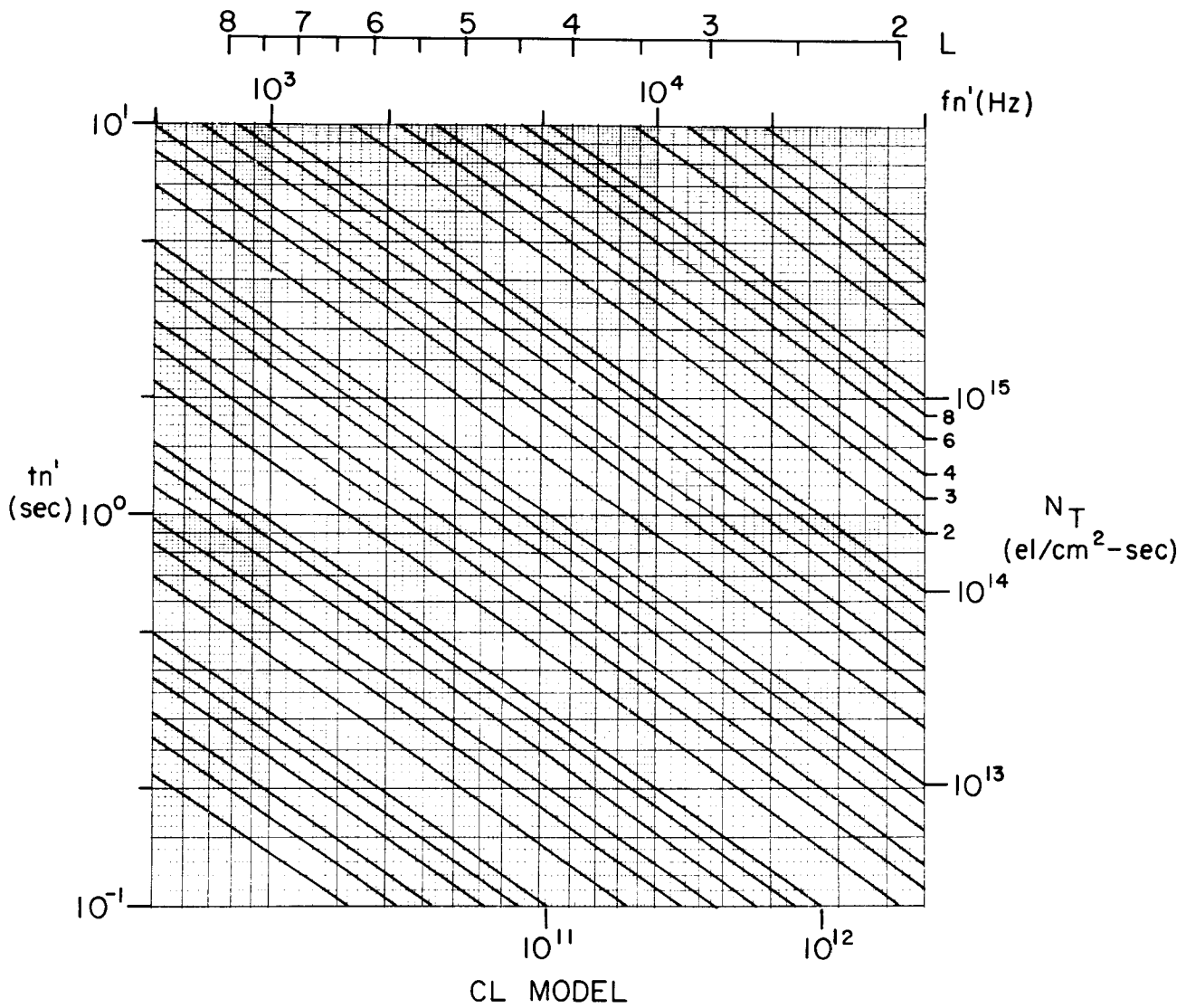
Figure 11. Curves of constant tube content for a collisionless model.
The format is similar to that of Figure 8.
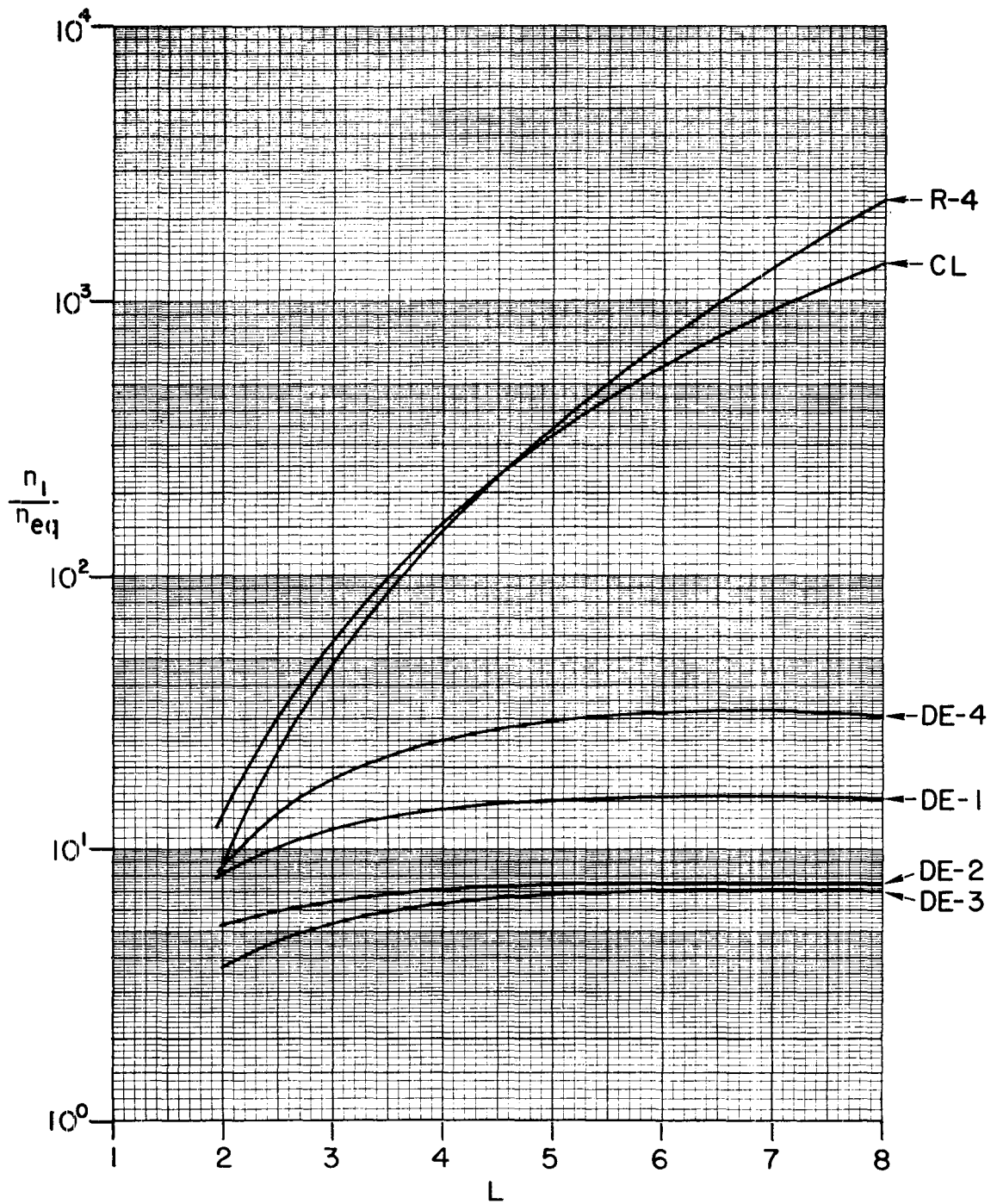
Figure 12. A plot of the ratio between the electron concentra-
tion at 1000 km altitude and the equatorial concen-
tration as a function of L for different field-line distribution
models.
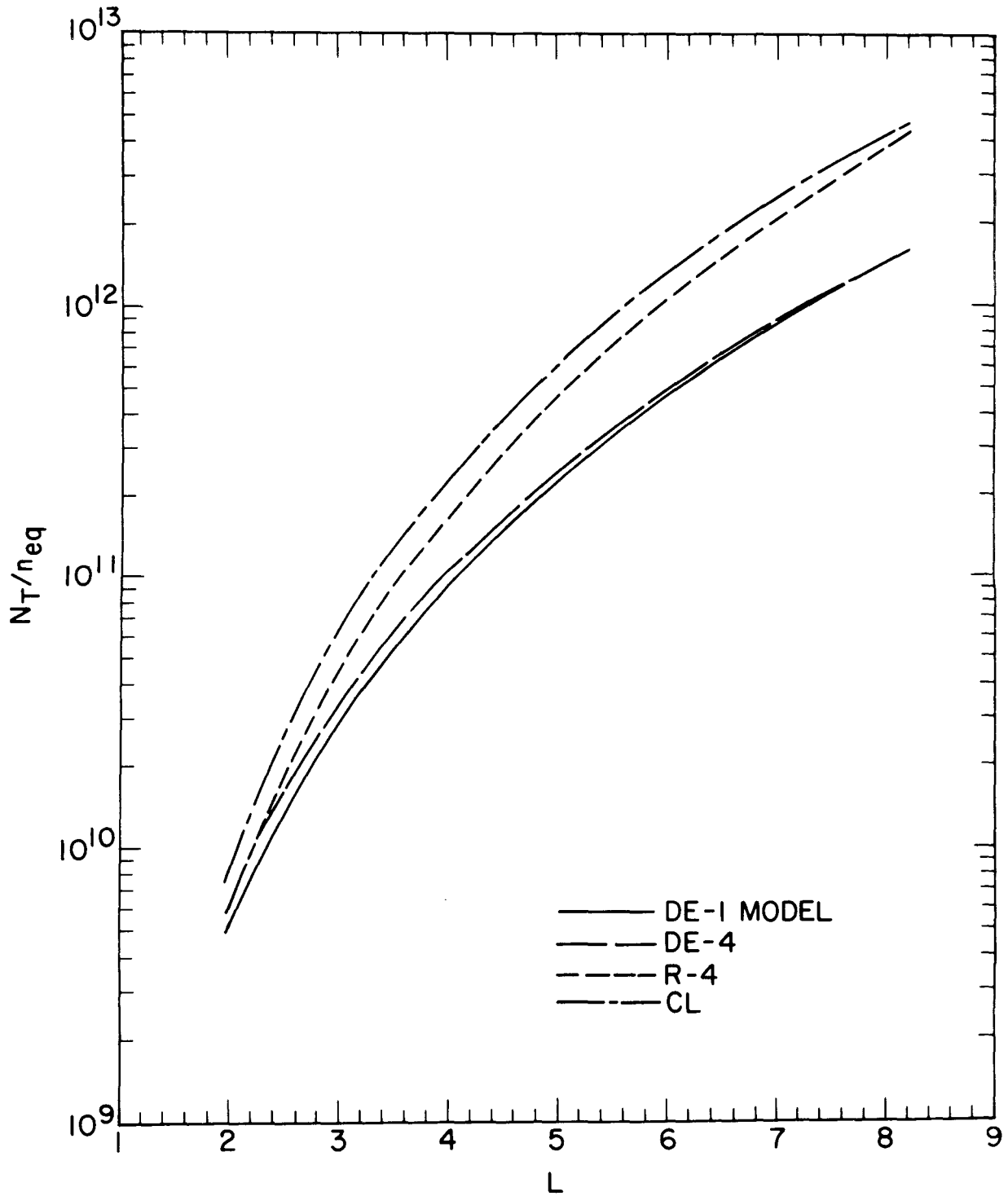
Figure 13. A plot of the ratio between the tube content and
the equatorial electron concentration as a function
of L for different field-line distribution models.

40
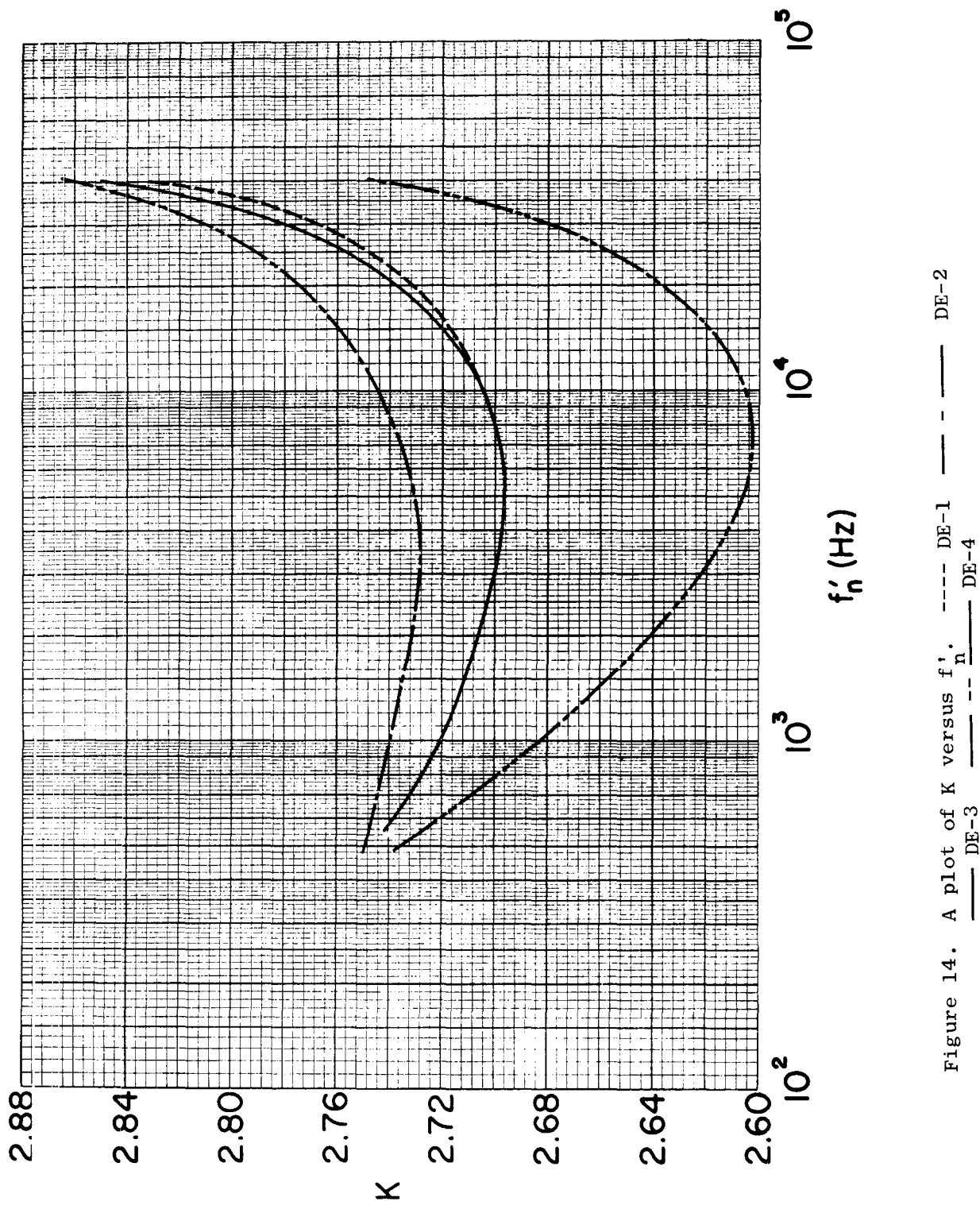
Figure 14. A plot of K versus f_n'.
--- DE-1   ———— DE-2
———— DE-3   —·—· DE-4

41
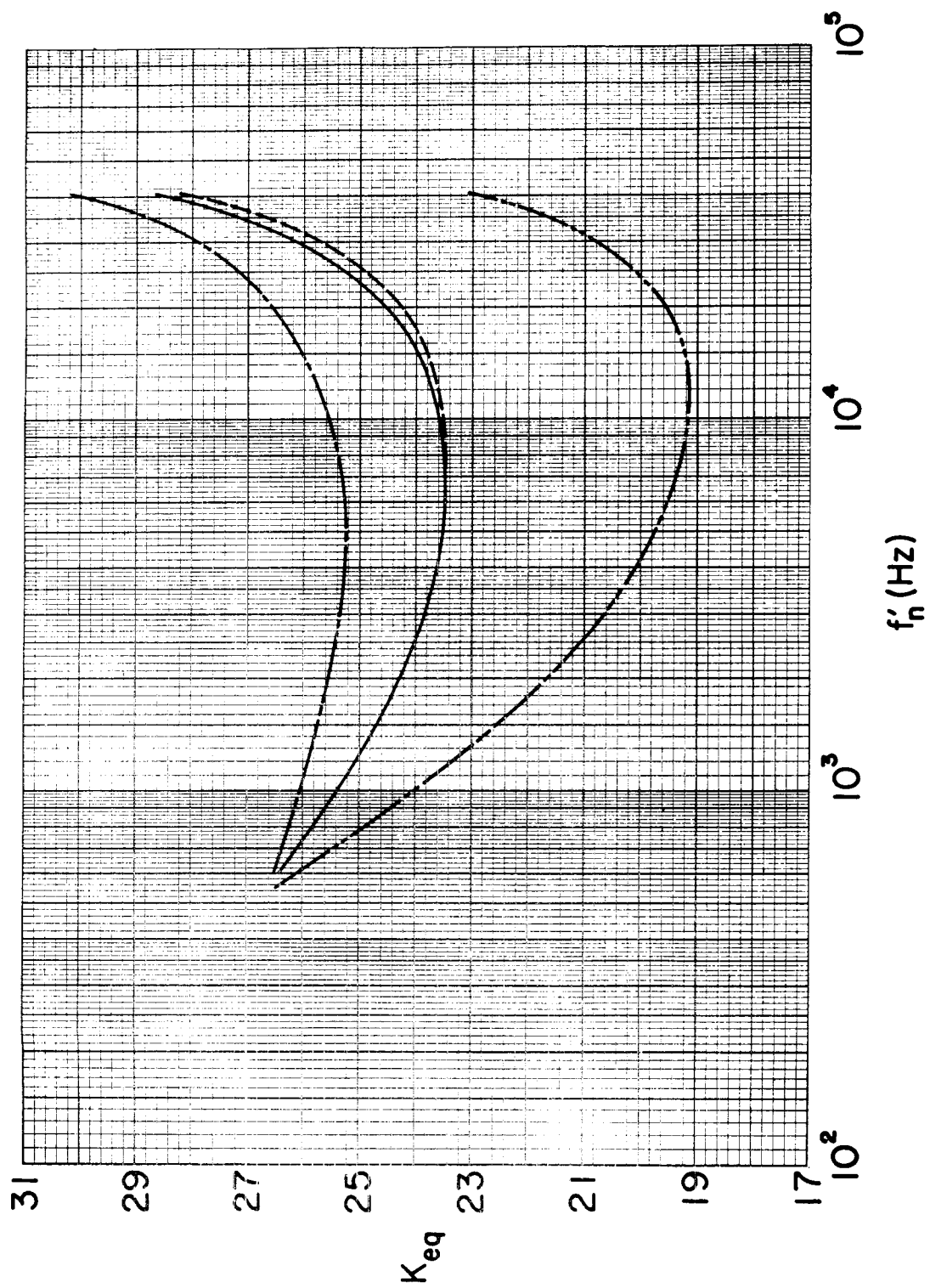
Figure 15. A plot of K_{eq} versus f'_n. --- DE-1   ———— DE-2
  ———— DE-3   -- -- DE-4
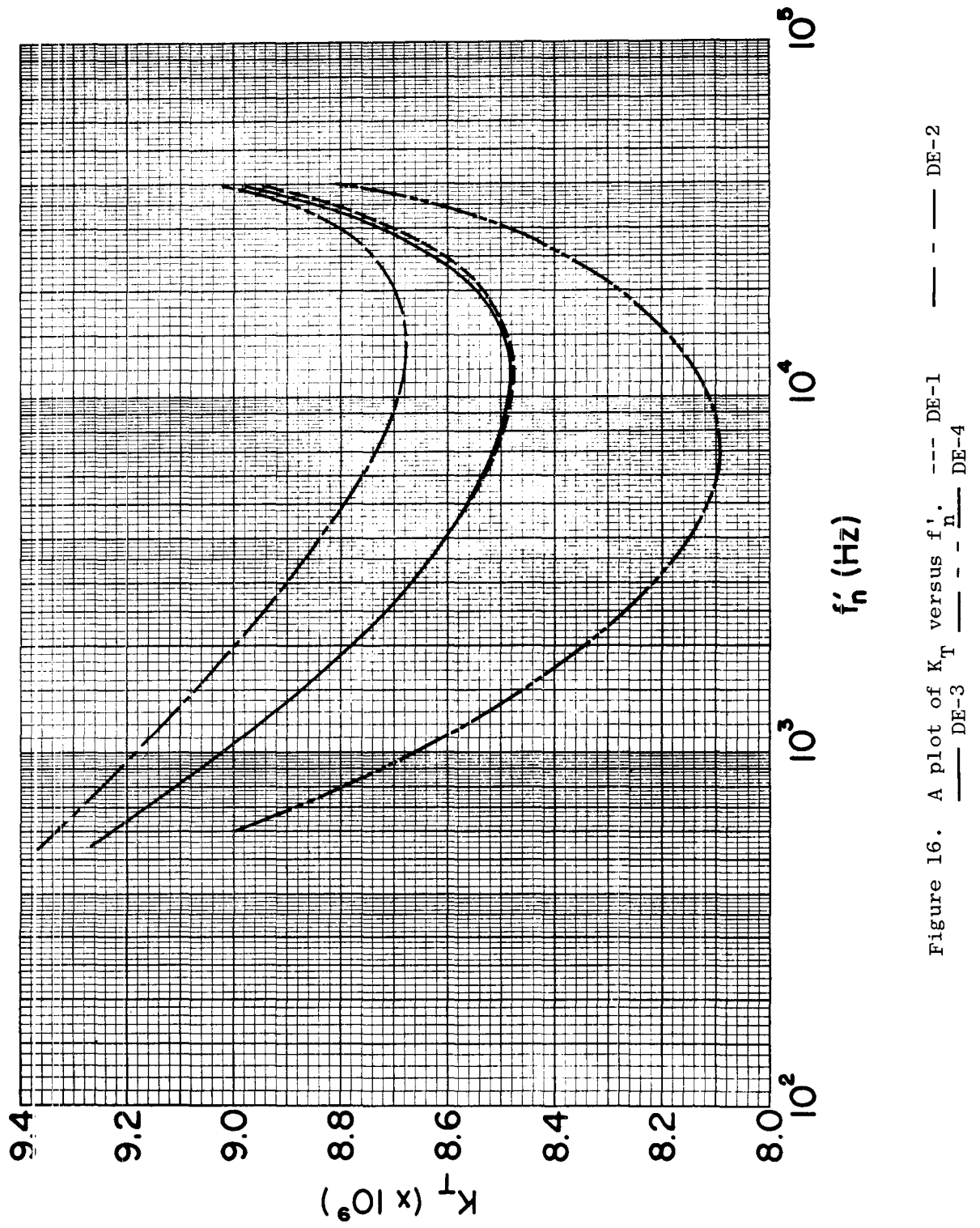
Figure 16. A plot of K_T versus f'_n. --- DE-1 — - — DE-2
——— DE-3 — - - — DE-4
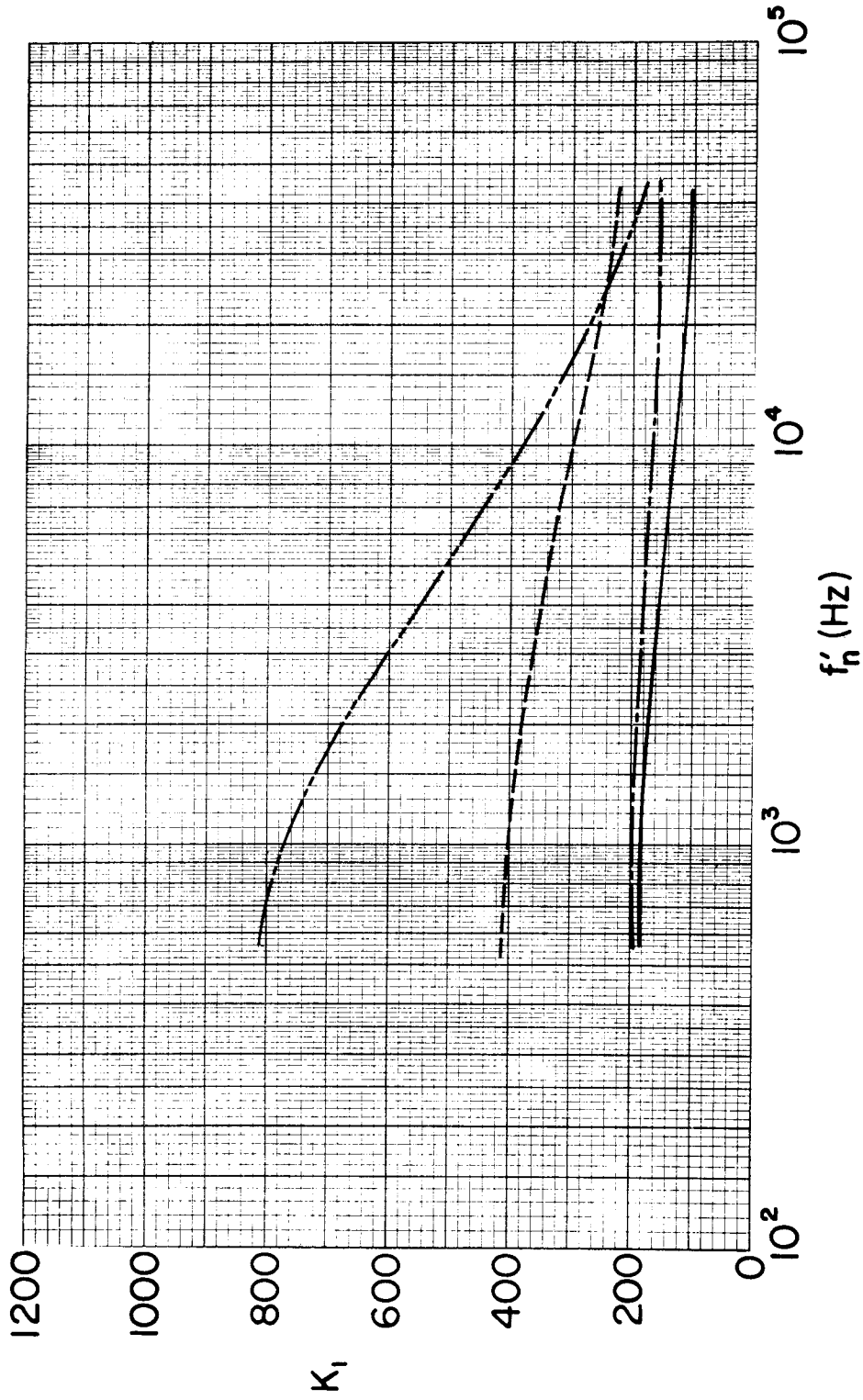
Figure 17. A plot of K_1 versus f'_n. --- DE-1 ——— DE-2
——— DE-3 --——— DE-4
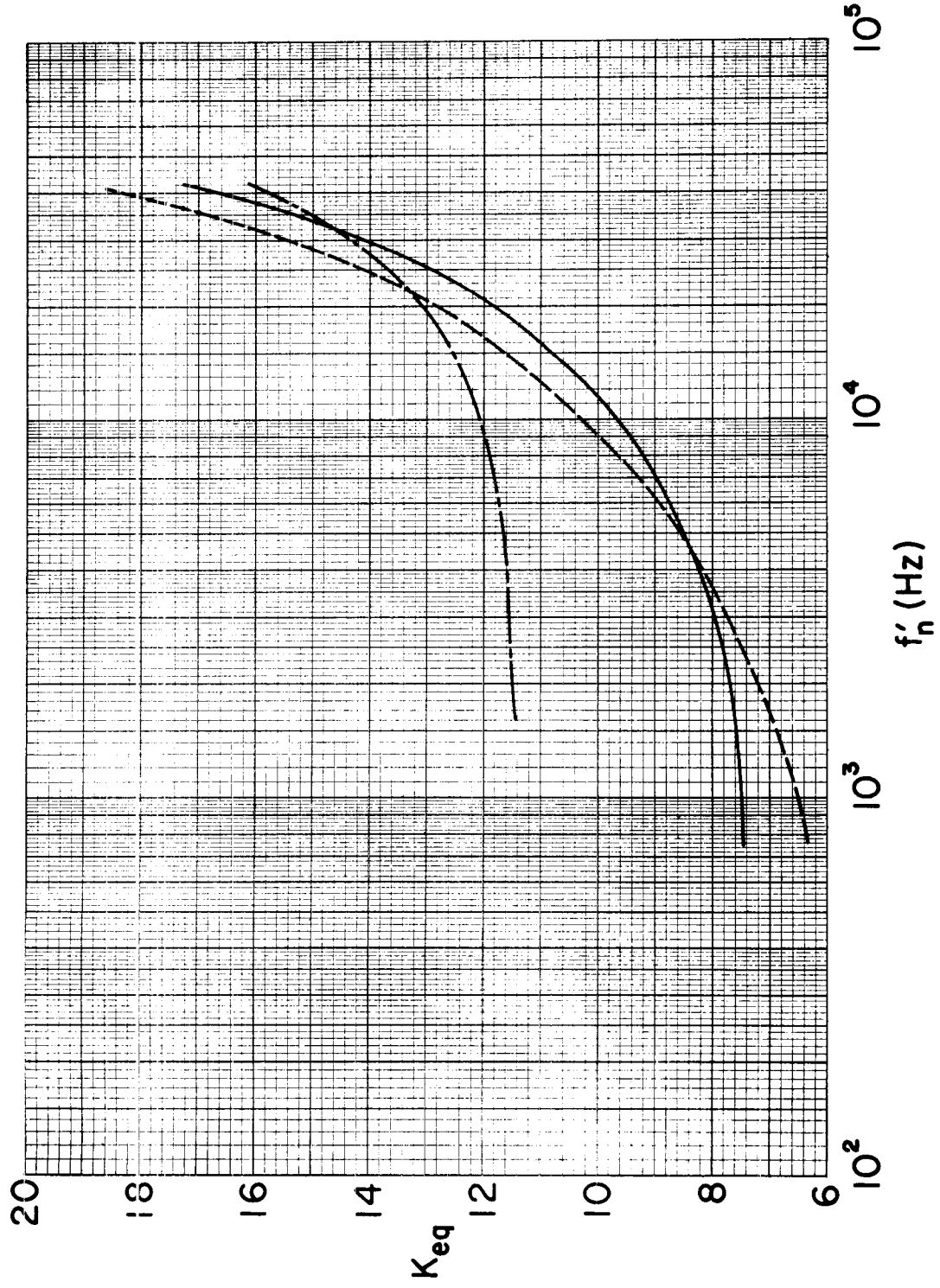
Figure 19. A plot of K_{eq} versus f'_n. —— CL   --- R-4   —— HY
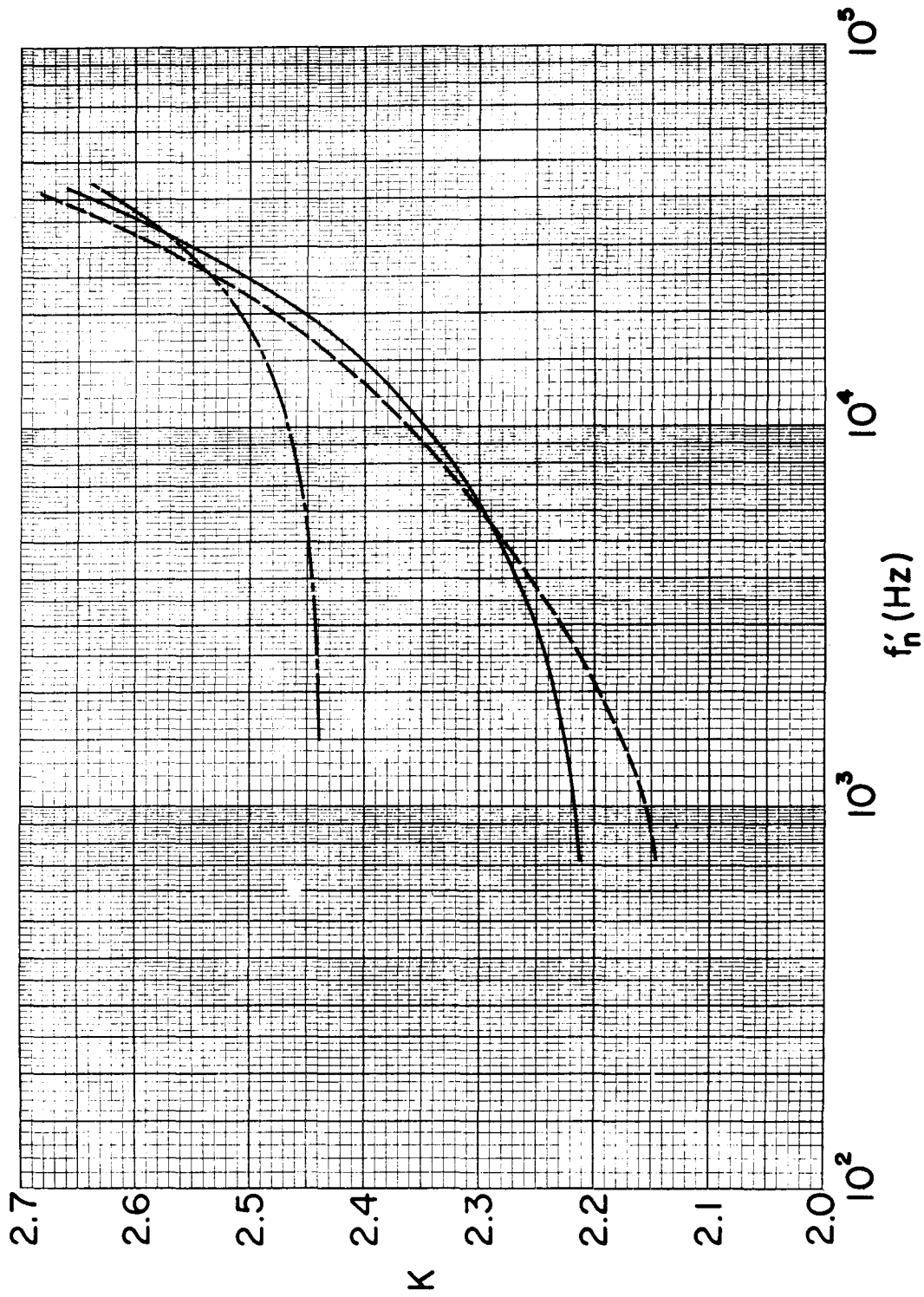
Figure 18. A plot of K versus f'_n. —— CL   --- R-4   —— HY
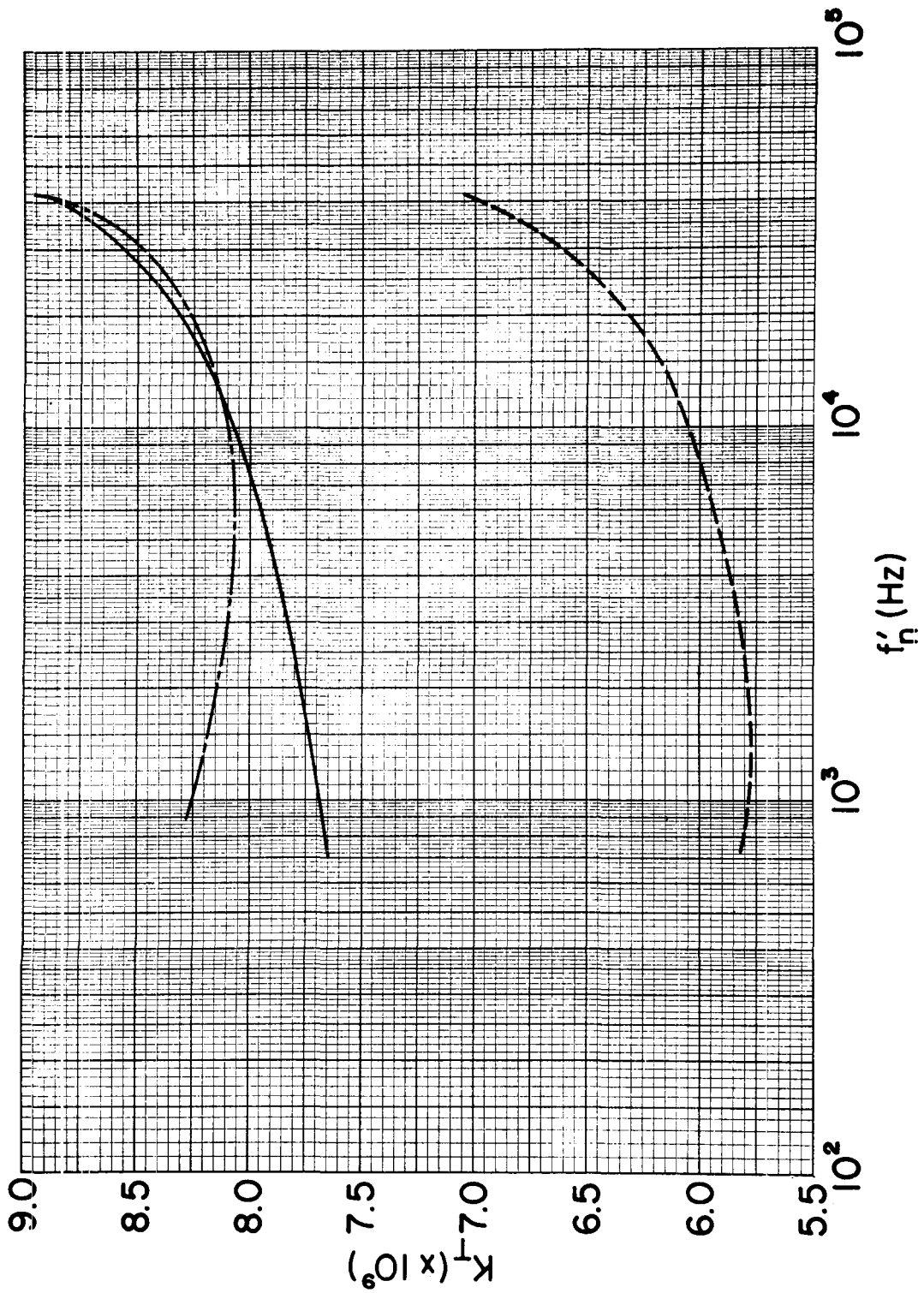
Figure 20. A plot of K_T versus f_n'. —— CL --- R-4 — · — HY
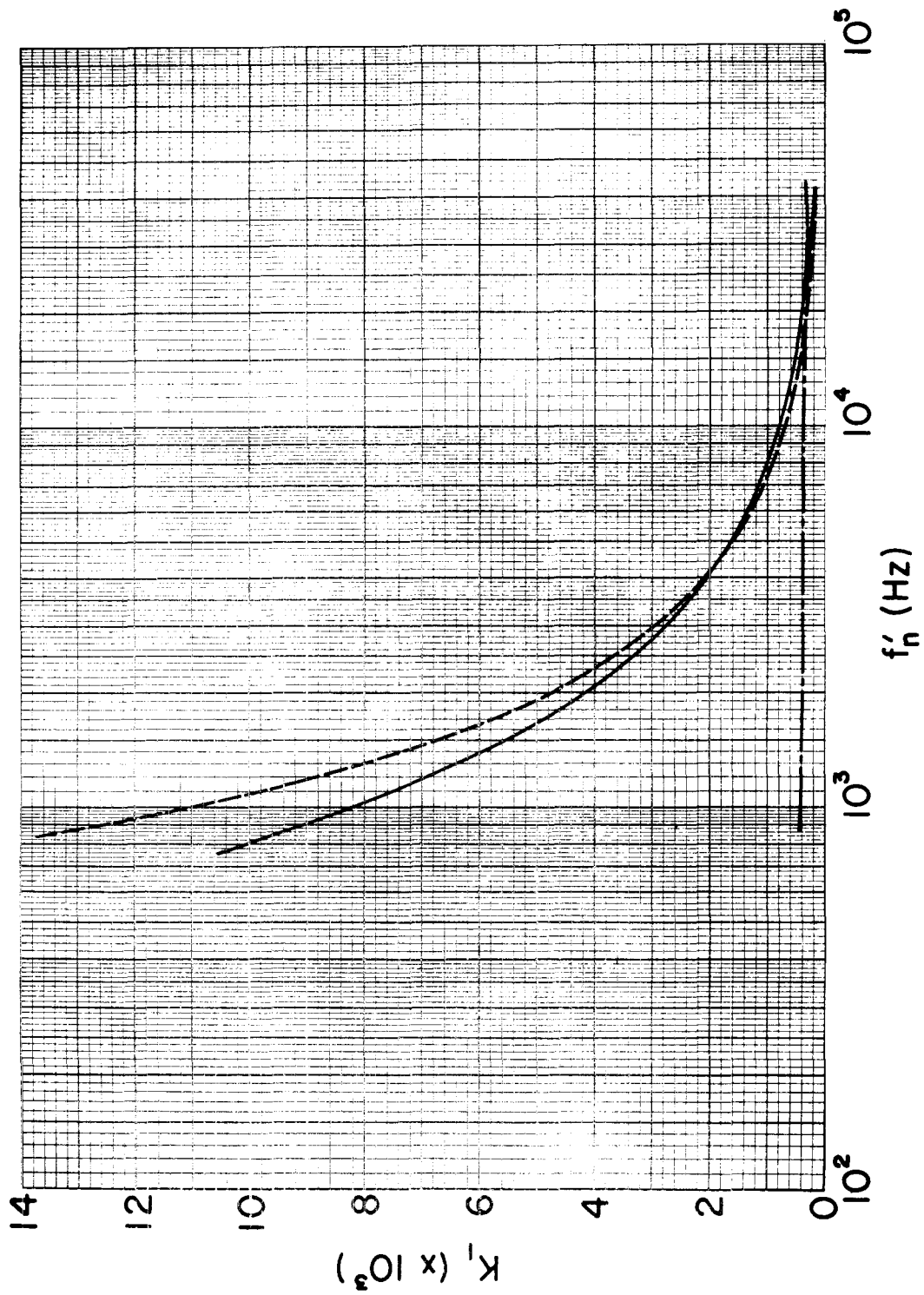
Figure 21. A plot of K_1 versus f'_n. —— CL   - - - R-4   —— HY
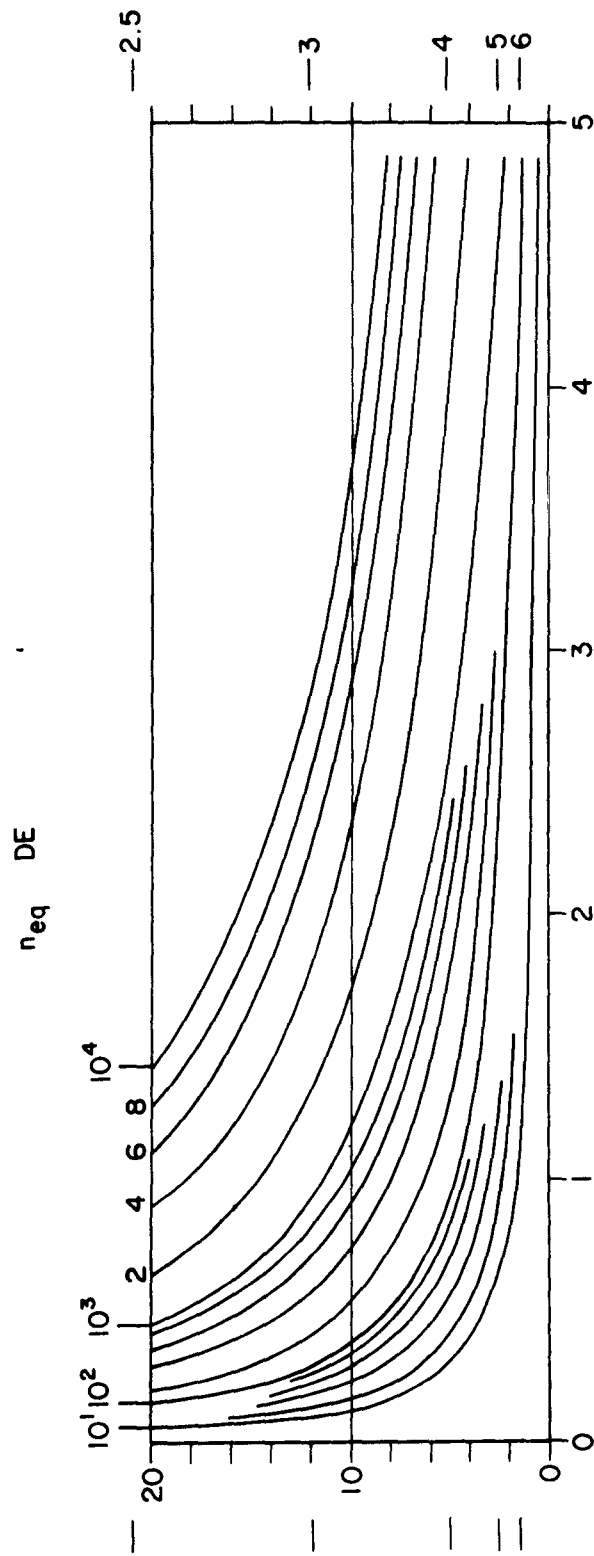
Figure 22. An overlay designed to be used on whistler spectrograms. The vertical scales are frequency in kHz (left) and L-value (right), and the horizontal scale is time in seconds. The sloping curves represent constant values of equatorial electron concentration assuming diffusive equilibrium distribution of plasma along field lines.
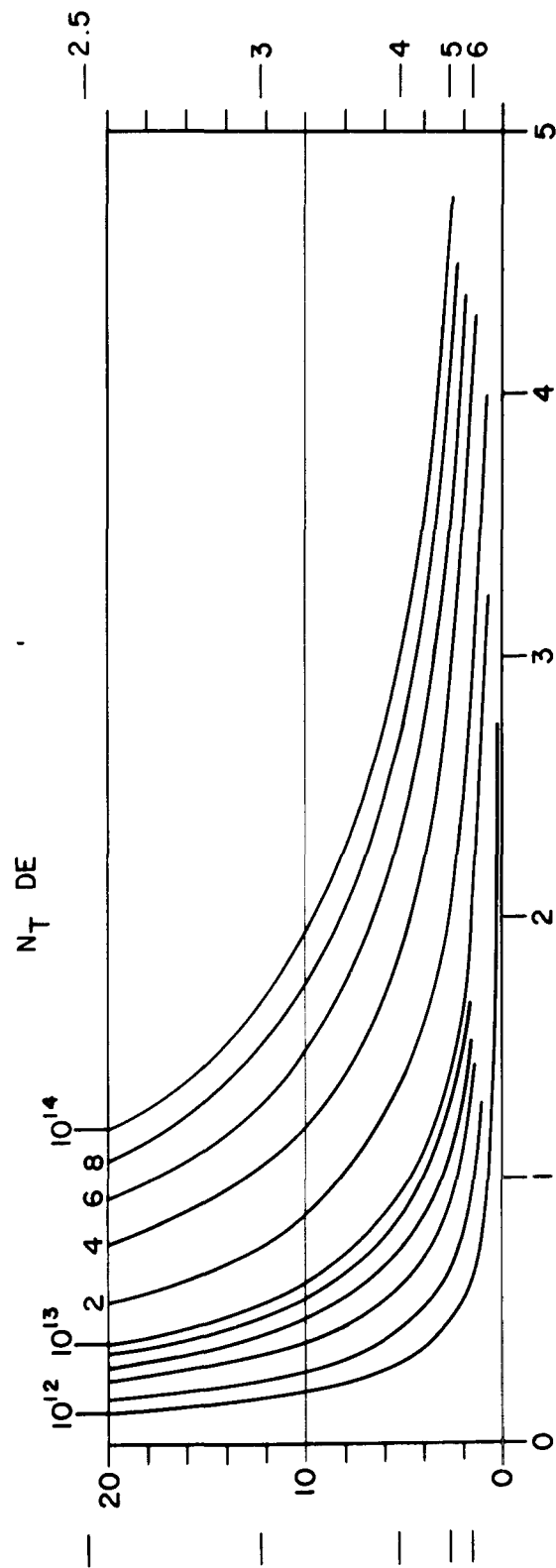
Figure 23. An overlay designed to be used on whistler spectrograms. The vertical scales are frequency (left) and L-value (right), and the horizontal scale is time in seconds. The sloping curves represent constant values of tube content assuming diffusive equilibrium distribution of plasma along field lines.

canno: be resolved on figures of this scale. The horizontal bars at the edges of the figure show L-values, and the sloping curves represent constant values of n_{eq} and N_T. These overlays are designed to be used on 35 mm Rayspan records with 0-20 kHz per 30 mm vertical scale and 20 mm per second of real time horizontal scale. An overlay may be placed over a spectrogram with the t = 0 line on the causative sferic. The L-value and values of n_{eq} or N_T can be read directly from the position of the whistler nose on the spectrogram. This method neglects corrections for dispersion in the conjugate ionospheres (Chapter 3) and for sub-ionospheric propagation time (Chapter 4). This is not very serious, however, because the two corrections tend to cancel one another and because of the relatively poor precision inherent in this method. As mentioned in the previous section, n_1 depends sensitively on electron concentration models and would require a large number of overlays. It is therefore preferable to obtain n_1 from n_{eq} using Figure 12.

An important advantage of this method is that it permits a quick identification of any structures in n_{eq} or N_T profiles from a train of nose whistlers. For example, if n_{eq} is constant with L in some part of the magnetosphere penetrated by whistlers, the train of corresponding noses will follow a n_{eq} = constant curve in Figure 22. Electron concentration profiles in the magnetosphere frequently exhibits complex structures such as those reported by Park and Carpenter [1970]. These structures can be easily identified on whistler spectrograms with the aid of the overlays.

G. EMPIRICAL FORMULAS

As shown in Figures 14 through 21, K, K_{eq}, K_T and K_1 vary only slowly with f'_n. These quasi-constants can be approximated by various curve

fitting techniques to achieve desired accuracy. For slide rule calcula-
tions, they can be approximated by constants. For the DE-1 model, the
following approximate formulas can be used:

| | Maximum Error |
| Formulas | $2.5 \leq L \leq 7$ |

$$f_{Heq} = 2.7 \; f'_n \qquad\qquad 1.1\%$$

$$L = \left(\frac{8.74 \times 10^5}{f_{Heq}}\right)^{1/3} \qquad\qquad 0.4$$

$$n_{eq} = 24\left(\frac{f'_n t'^2_n}{L^5}\right) \qquad\qquad 7.6$$

$$N_T = 8.6 \times 10^9\left(\frac{f'_n t'^2_n}{L}\right) \qquad\qquad 5.4$$

$$n_1 = 340\left(\frac{f'_n t'^2_n}{L^5}\right) \qquad\qquad 25$$

and for the CL model,

| | Maximum Error |
| Formulas | $2.5 \leq L \leq 7$ |

$$f_{Heq} = 2.3 \; f'_n \qquad\qquad 7.6\%$$

$$L = \left(\frac{8.74 \times 10^5}{f_{Heq}}\right)^{1/3} \qquad\qquad 2.5$$

$$n_{eq} = 10\left(\frac{f'_n t'^2_n}{L^5}\right) \qquad\qquad 35.9$$

$$N_T = 7.9 \times 10^9\left(\frac{f'_n t'^2_n}{L}\right) \qquad\qquad 7.8$$

These approximations by constant coefficients are reasonably good for diffusive equilibrium model, but they lead to somewhat larger errors in the case of the collisionless model. In particular, an attempt to use a constant coefficient K_1 for the collisionless model may lead to errors as large as a factor of 4.

For machine processing, a parabolic approximation of the following form gives high accuracy with a reasonable amount of computation.

$$K = a_o + a_1 \, F + a_2 \, F^2 \qquad (2.22)$$

where $F = \log_{10} f_n$ and the a's are constants. The coefficients a_o, a_1, a_2 can be obtained from a least squares fit to the values of the K's in Tables 2 through 8. Tables 9 and 10 give the results of a least squares fit for the range $2.5 \leq L \leq 7$ for the DE-1 model and R-4 model, respectively. The last column in the tables shows the maximum error due to this approximation in the range $2.5 \leq L \leq 7$.

TABLE 9. COEFFICIENTS IN EQN. (2.22) FOR THE DE-1 MODEL

	a_0	a_1	a_2	max.error $2.5 \leq L \leq 7$
K	3.5475	-4.7351×10^{-1}	6.5879×10^{-2}	0.14%
K_{eq}	6.5517×10^1	-2.2064×10^1	2.8976	0.61%
K_T	1.5778×10^{10}	-3.5512×10^9	4.3313×10^8	0.27%
K_1	3.8873×10^2	9.3285×10^1	-2.9088×10^1	0.95%

TABLE 10. COEFFICIENTS IN EQN. (2.22) FOR THE R-4 MODEL

	a_o	a_1	a_2	max. error $2.5 \leq L \leq 7$
K	3.0156	-6.5114×10^{-1}	1.2217×10^{-1}	0.3%
K_{eq}	3.6330×10^{1}	-1.9974×10^{1}	3.3715	1.9%
K_l	1.3347×10^{5}	-6.5024×10^{4}	7.9264×10^{3}	107%
K_T	1.0186×10^{10}	-2.7711×10^{9}	4.3506×10^{8}	0.4%

III. CORRECTIONS FOR DISPERSION IN THE IONOSPHERE

A. OUTLINE OF THE CHAPTER

We use f_n and t_n to denote the whistler nose frequency and travel time at the nose observed after propagation through the ionosphere and the magnetosphere. Because the ionosphere has great variability, but relatively small effects on whistler propagation, we have chosen to account for the ionosphere by making 'corrections' to the observed f_n and t_n, obtaining quantities f_n' and t_n' which would result from propagation through the magnetosphere only. Once f_n' and t_n' are obtained, the path latitude and the electron concentration along the path in the magnetosphere can be calculated by one of the methods described in the previous chapter. The purpose of this chapter is to examine in detail effects of the ionosphere on whistler propagation and to develop methods for obtaining f_n' and t_n' from f_n and t_n.

B. WHISTLER DISPERSION IN THE IONOSPHERE

The whistler travel time through the conjugate ionospheres, or the second term in Eq. (1.3) is

$$t_{ci}(f) = \frac{1}{2c} \int_{ci} \frac{f_p}{f^{1/2} f_H^{1/2} \left(1 - \frac{f}{f_H}\right)^{3/2}} \, ds$$

where the subscript ci refers to the two conjugate ionospheres. The integration extends through both ionospheres below 1000 km altitude. Several simplifying assumptions and approximations will be used in this chapter in treating ionospheric effects on whistler propagation. Some of them are justified partly on grounds that the ionospheric contribution t_{ci} to

the total whistler travel time is small (typically less than 10%).

Since $\frac{f}{f_H} \ll 1$ in the ionosphere, we can write

$$D_{ci} \equiv t_{ci} \; f^{1/2} \simeq \frac{1}{2c} \int_{ci} \frac{f_p}{f_H^{1/2}} \; ds \qquad (3.1)$$

The quantity D is called dispersion, and Eq. (3.1) shows that the dispersion in the ionosphere is independent of wave frequency. The dispersion is additive, so that

$$D_{ci} = (D_i)_{\substack{northern \\ hemisphere}} + (D_i)_{\substack{southern \\ hemisphere}}$$

In the remainder of this section, we will compute D_i from the ionospheric parameters.

Assuming a horizontally stratified ionosphere and neglecting curvatures of magnetic field lines, we write

$$D_i = \frac{1}{2c \sin \delta} \int \frac{f_p}{f_H^{1/2}} \; dh \qquad (3.2)$$

where δ is the magnetic dip angle, and h is the altitude. If we further neglect small changes in latitude as we move along inclined magnetic field lines, f_H can be expressed as

$$f_H = f_{Ho} \left(1 + \frac{h}{r_o} \right)^{-3}$$

where f_{Ho} is the electron gyrofrequency at $h = 0$ and at the latitude of interest. Substituting this into Eq. (3.2), we obtain

$$D_i = \frac{1}{2c\ f_{Ho}^{1/2}\ \sin \delta} \int f_p \left(1 + \frac{h}{r_o} \right)^{3/2} dh \qquad (3.3)$$

Equation(3.3) has been evaluated numerically for several electron concentration profiles at $L = 4$ where $f_{Ho} = 1.57 \times 10^6$Hz and $\sin\delta = 0.957$. The ionosphere was assumed to be a simple α-Chapman layer described by

$$n = n_{max}\ exp\left\{ \frac{1}{2}\ [1 - z - exp(-z)] \right\} \qquad (3.4)$$

$$z = \frac{h-h_o}{H}$$

where n_{max} is the maximum electron concentration and h_o the height of the maximum concentration. Three different profiles corresponding to scale height $H = 50$, 75 and 100 km have been considered. Figure 24 illustrates the three profiles with $h_o = 300$ km and n_{max} adjusted so as to involve the same height-integrated content. The results are summarized in Table 11.

Table 11 shows that the dispersion does not depend sensitively on the shape of the electron concentration profile. A comparison between the constant n_{max} case (A, B and C) and the constant integrated content case (D, E and F) shows that the dispersion varies more with the content than it does with n_{max}. In estimating D_i it is therefore preferable to use integrated columnar content information obtained from Doppler shift measurements or Faraday rotation measurements of satellite beacon signals.

Since about two thirds of the integrated content is above the F layer peak, topside sounder results are preferred over bottomside sounder results. The desired information on the ionosphere near a whistler path of interest is usually not available, particularly in the case of satellite data, and
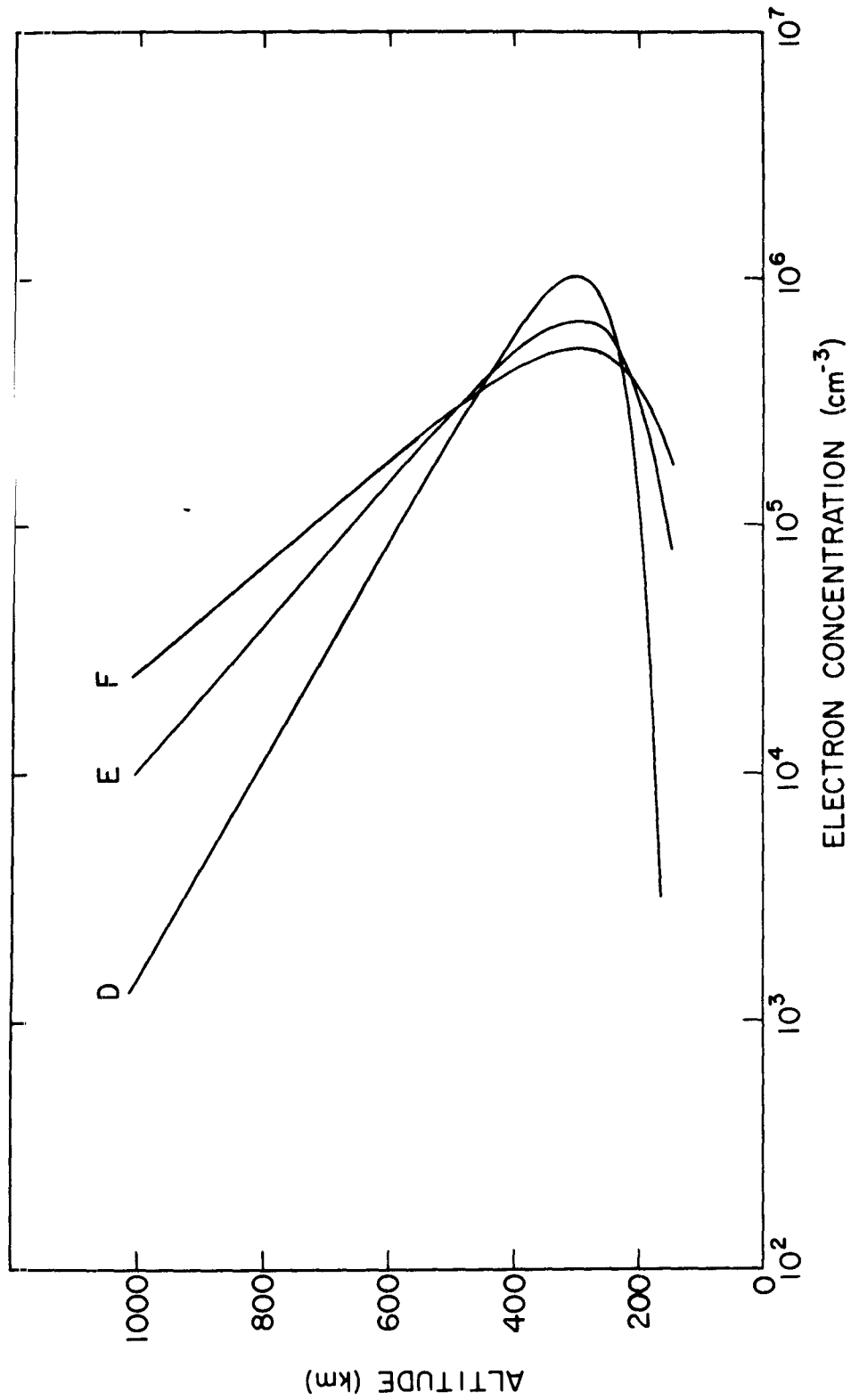
Figure 24. A sketch of model electron concentration profiles in the ionosphere.

59

TABLE 11.   IONOSPHERIC DISPERSION

	Scale height (km)	n_{max} (el cm^{-3})	Columnar Content (el cm^{-2})	D_i (sec$^{1/2}$)
A	50	10^6	2.06×10^{13}	4.43
B	75	10^6	3.08×10^{13}	6.31
C	100	10^6	4.01×10^{13}	7.72
D	50	10^6	2.06×10^{13}	4.43
E	75	6.68×10^5	2.06×10^{13}	5.17
F	100	5.13×10^5	2.06×10^{13}	5.53

an 'average' ionosphere must often be used.

The following formulas are offered for estimating D_i from columnar content N or the F2 layer critical frequency $f_o F2$.

$$D_i = 1.15 \ N^{1/2} \qquad\qquad (3.5)$$

$$D_i = 0.7 \ f_o F2 \qquad\qquad (3.6)$$

In the above equations, N is in units of 10^{12} el/cm^2 and $f_o F2$ in MHz. A typical value of D_{ci} (for two conjugate ionospheres) may be 8 during the day and 4 during the night near solar-cycle minimum. The corresponding values for solar cycle maximum may be 16 and 8.

The values of f_{Ho} and $\sin\delta$ in Eq. (3.3) vary with magnetic latitude. However, in the principal range of whistler propagation $2 \overset{\sim}{<} L \overset{\sim}{<} 7$ they can be regarded as constants, because their variations are not important compared to the uncertainties in electron concentration profile usually encountered. The height of the F layer peak makes little difference in the calculated value of D_i. A change in h_o by 200 km results in a change of only $\sim 5\%$ in D_i.

C. CALCULATIONS AND RESULTS

The whistler time delay is written as

$$t(f) = \beta n_{eq}^{1/2} \int_0^{\phi_1} \Im(\phi,f) \ d\phi + D_{ci} \ f^{-1/2} \qquad (3.7)$$

The first term on the right hand side is the magnetospheric part from Eq. (2.19), and the second term the propagation delay in two conjugate ionospheres. Equation (3.7) is evaluated numerically by the same procedures

used in Section 2C in search of the minimum time delay. In the present case, however, f_n depends on n_{eq} and D_{ci} as well as on the whistler path latitude. The dependence of f_n on n_{eq} for constant L and D_{ci} is illustrated schematically in Figure 25. The two dashed curves A and B represent the first term in Eq. (3.7), or the travel time through the magnetosphere. The two whistlers propagate on the same magnetic shell, and hence exhibit the same f_n'. The travel time for curve B is assumed to be 9 times as large. The curve marked C represents the travel time through conjugate ionospheres, or the second term in Eq. (3.7). The solid curves are the result of adding C to A and B. Evidently the effect of the ionosphere on f_n is less for larger magnetospheric electron concentrations. It is also apparent that the larger the value of D_{ci}, the larger its effect will be on f_n.

The calculations of f_n are repeated for variations in either D_{ci}, t_n', or L while the other two are held constant. The values of D_{ci} used are D_{ci} = 2,4,8,16 and 32. The results of such calculations for L = 2.5, 4 and 6 are shown in Figures 26 through 28 where the quantity $(f_n - f_n')/f_n'$ is plotted against D_{ci} for several values of t_n'. The quantity $(t_n - t_n')$ is also calculated from Eq. (3.7) and plotted in Figures 29 and 30.

D. EMPIRICAL FORMULAS

Although f_n' and t_n' can be obtained from f_n, t_n and D_{ci} with the aid of graphs illustrated in Figures 26 through 30, such a process is obviously cumbersome and time-consuming. In this section, we construct a few simple empirical formulas to approximate the results of the previous section.

We expect from the earlier discussion that the difference between f_n and f_n' would increase with D_{ci} and decrease with t_n, so we try an equation of the form
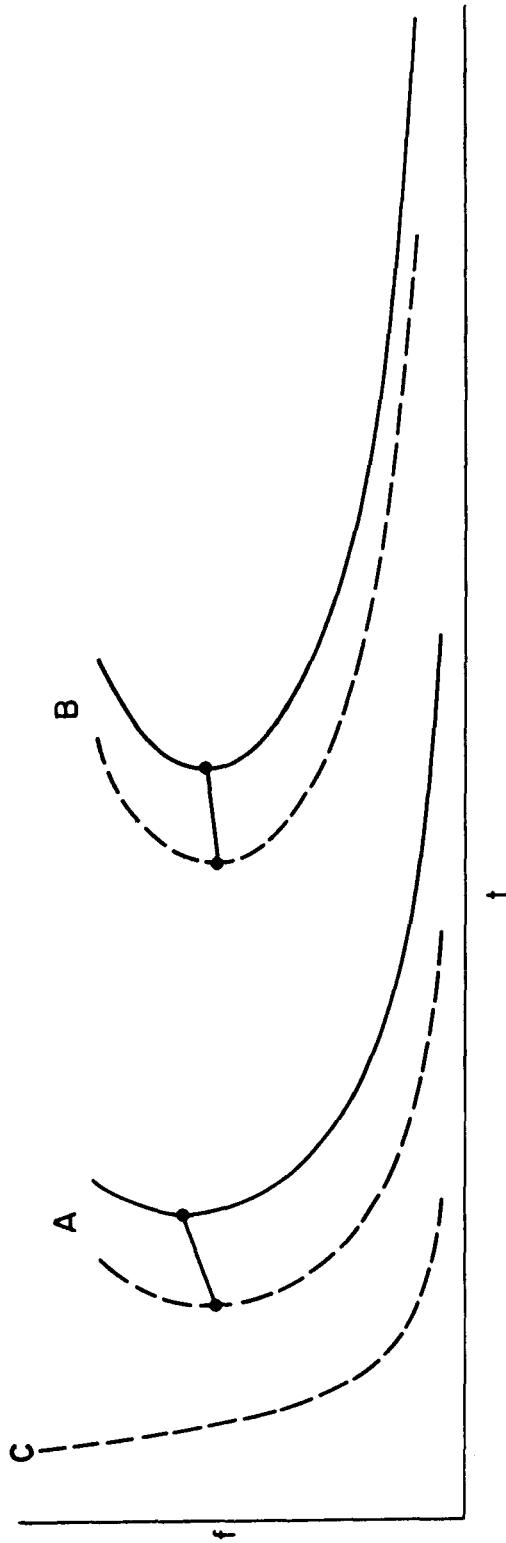
Figure 25. A sketch illustrating the effects of ionospheric dispersion on
nose whistlers. The dashed curves A and B result from propaga-
tion through the magnetospheric part of the path. The path lati-
tude is assumed to be identical in both cases, but the electron
concentration for B is 9 times that for A. The solid curves re-
sult from adding the ionospheric propagation delay C to A and B.
The effects of the ionosphere on the nose frequency decreases
with increasing electron concentration in the magnetosphere.
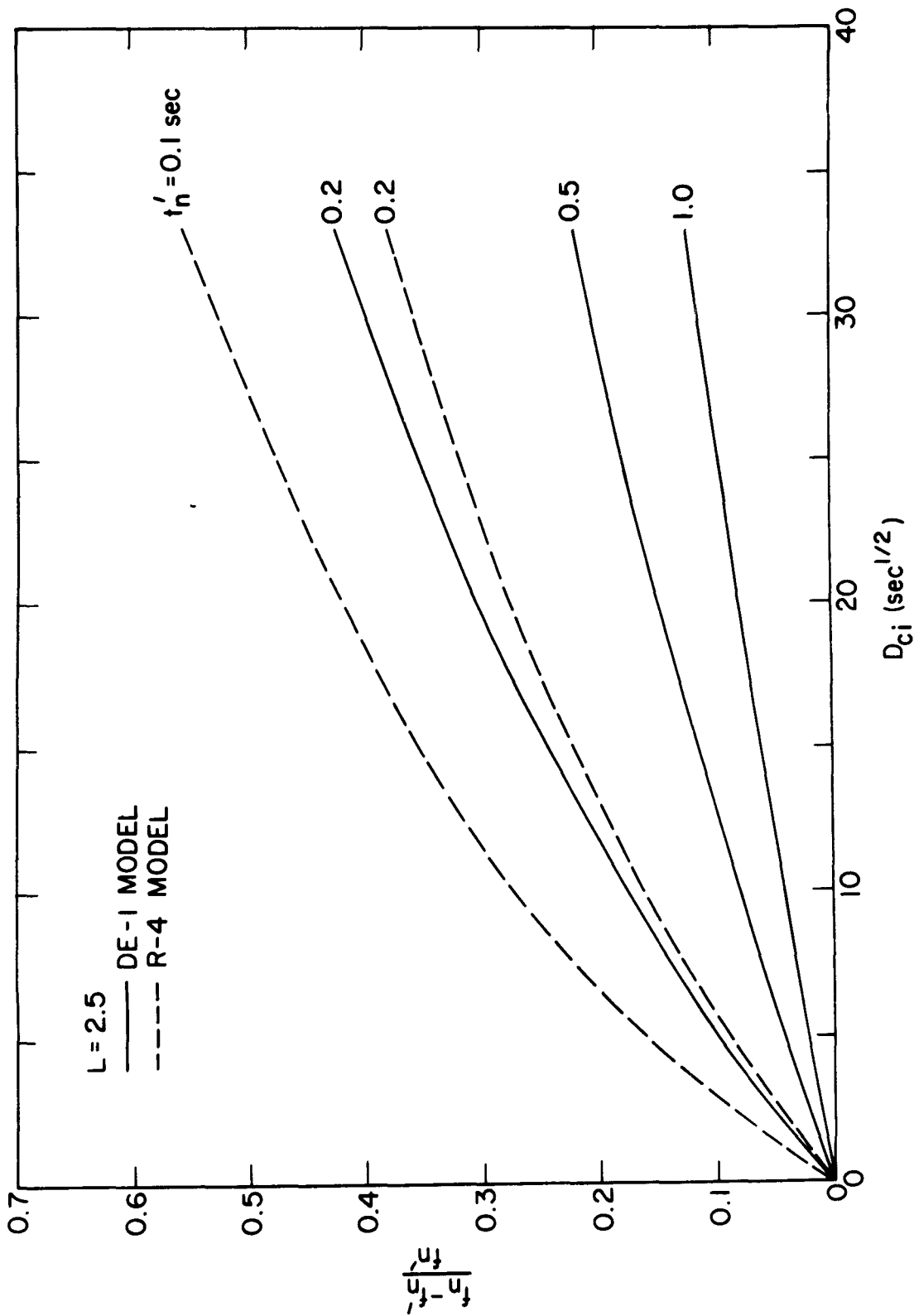
Figure 26. A plot showing the effects of ionospheric dispersion on the nose frequency of a whistler propagating along an L = 2.5 field line for different values of t'_n and for two different field-line distribution models.
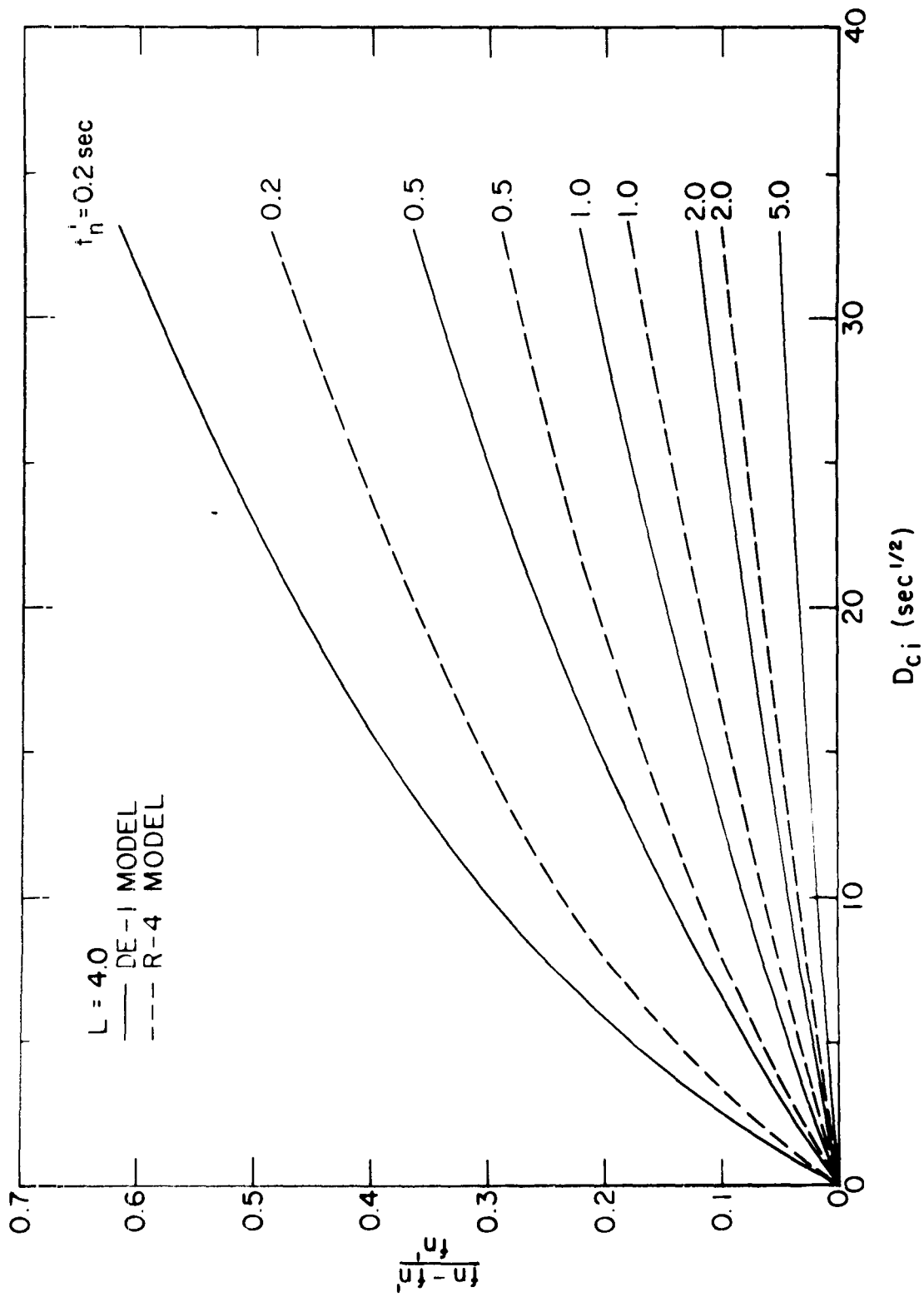
Figure 27. A plot similar to Figure 26 but for an L = 4 field line.
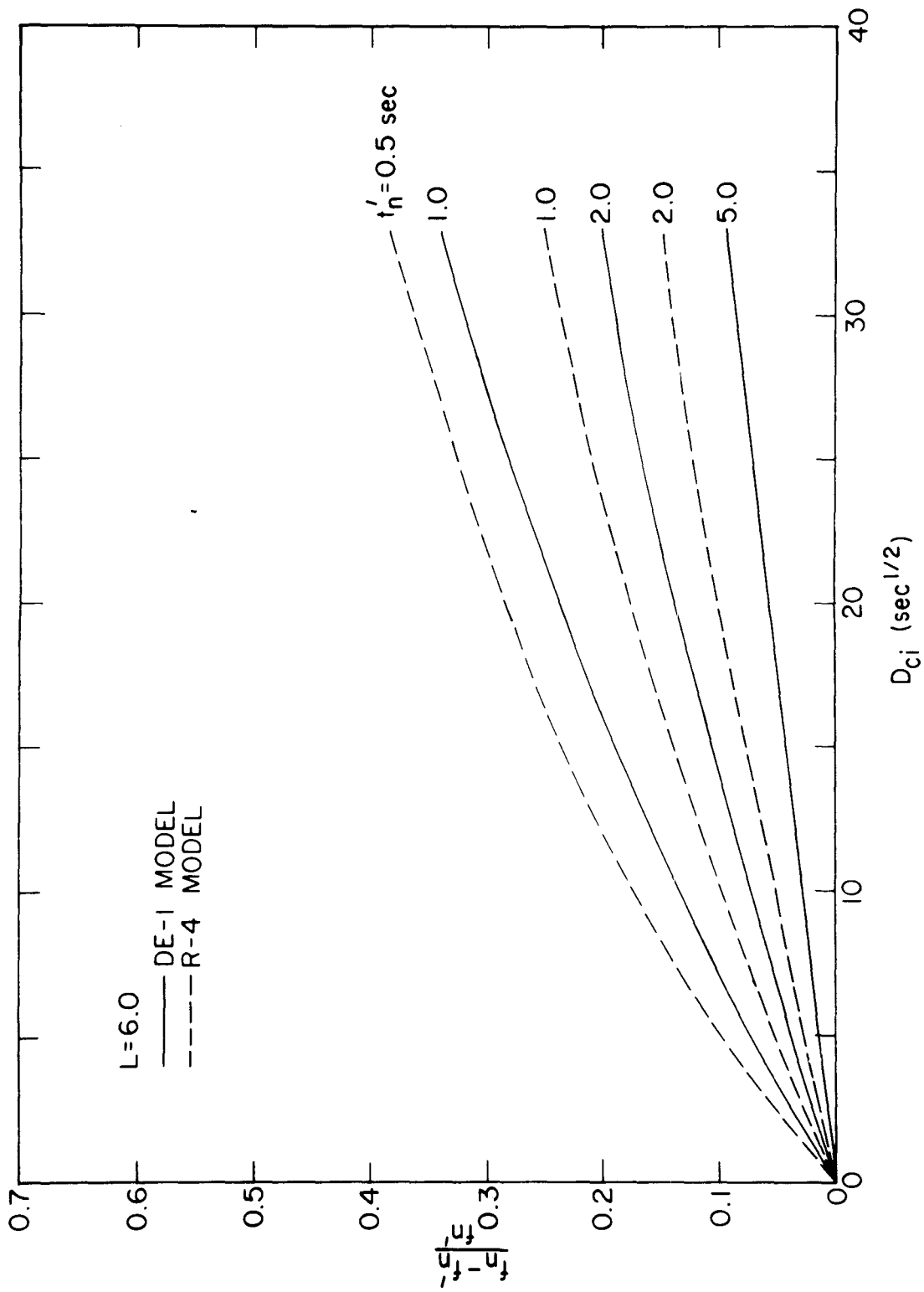
Figure 28. A plot similar to Figure 26 but for an L = 6 field line.
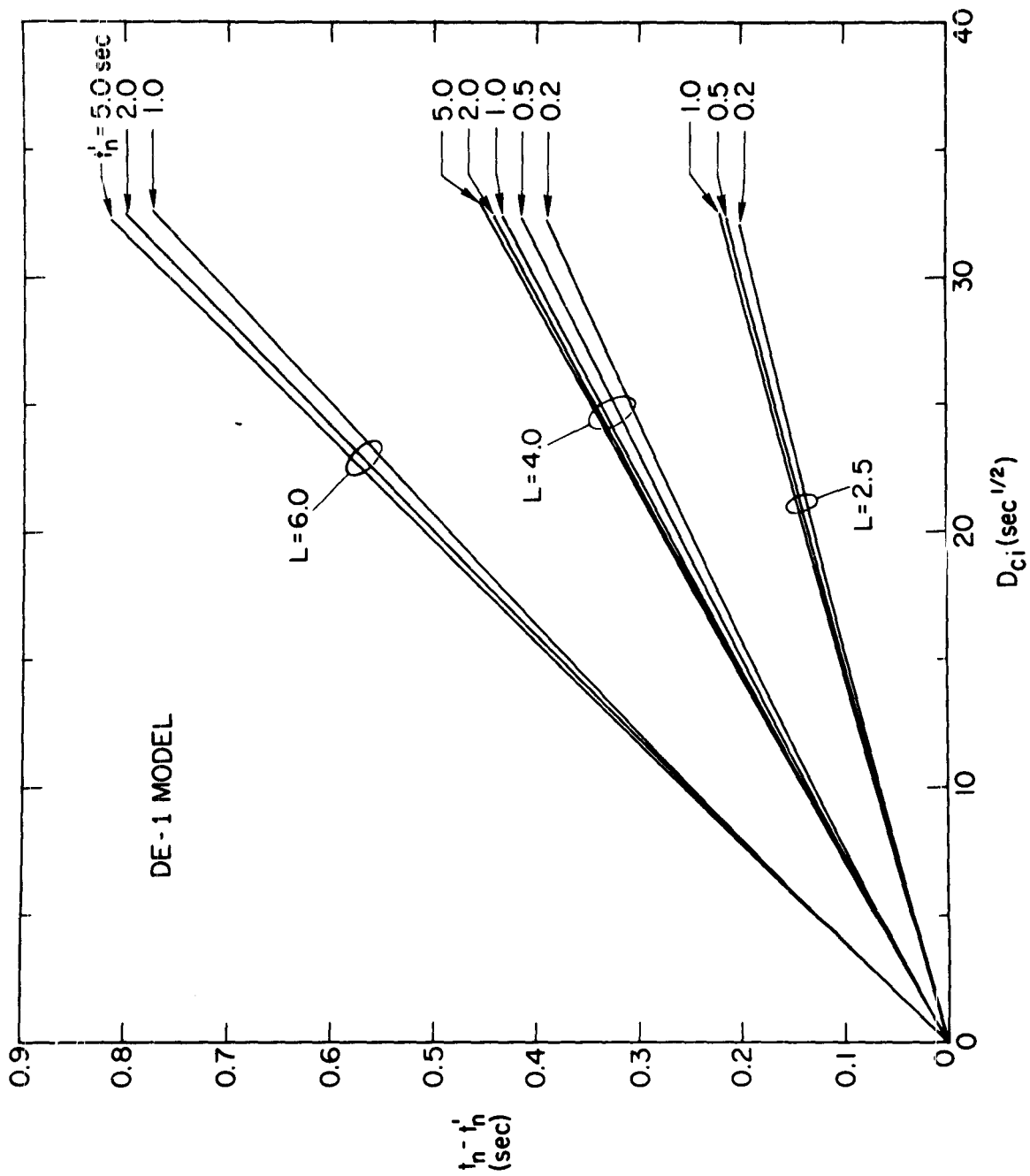
Figure 29. A plot showing the effects of ionospheric dispersion on the whistler t_n for a diffusive equilibrium model and for several different values of L and t_n'.
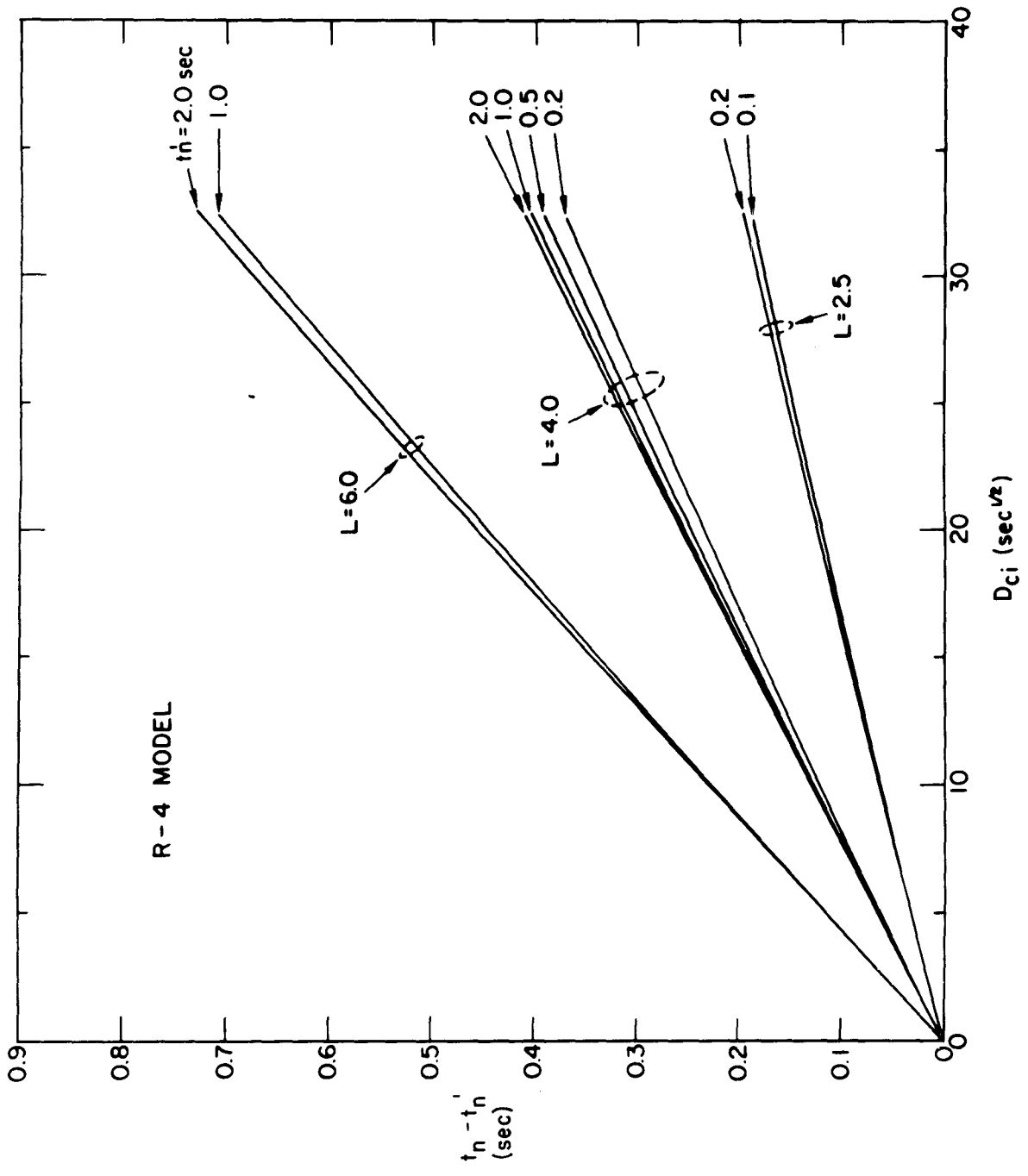
Figure 30. A plot similar to Figure 29 but for the R-4 model.

$$\frac{f_n - f'_n}{f'_n} = \gamma' \frac{D_{ci}}{t_n}$$

It is found that γ' is nearly constant for a given L-value, but that it decreases with increasing L. Since $L \propto f_{Heq}^{-1/3}$, and f_{Heq} is roughly proportional to f_n, we write

$$\frac{f_n - f'_n}{f'_n} = \gamma \frac{D_{ci}}{f_n^{1/3} t_n} \tag{3.8}$$

Equation (3.8) with a constant γ is a good approximation to the results of the previous section for a wide range of f_n, t_n and D_{ci}. Empirically, the best value of γ is found to be 0.17 for DE models and 0.15 for the CL or R-4 model. Thus,

$$f'_n = \frac{f_n}{1 + 0.17 \ (D_{ci}/t_n f_n^{1/3})} \tag{3.9}$$

for DE models, and

$$f'_n = \frac{f_n}{1 + 0.15 \ (D_{ci}/t_n f_n^{1/3})} \tag{3.10}$$

for the collisionless model. The error in f'_n due to the above approximation is plotted in Figures 31 and 32 against D_{ci} for a range of values of t'_n and L. The fact that the per cent error is generally larger for larger D_{ci} and for smaller t'_n means that the approximation by Eqs. (3.9) and (3.10) is better when the ionospheric part of the whistler dispersion is relatively small. For all realistic values of D_{ci} and t'_n, the error in f'_n is less than $\sim$ 3%. Several curves that surpass the 3% error level in Figures 31
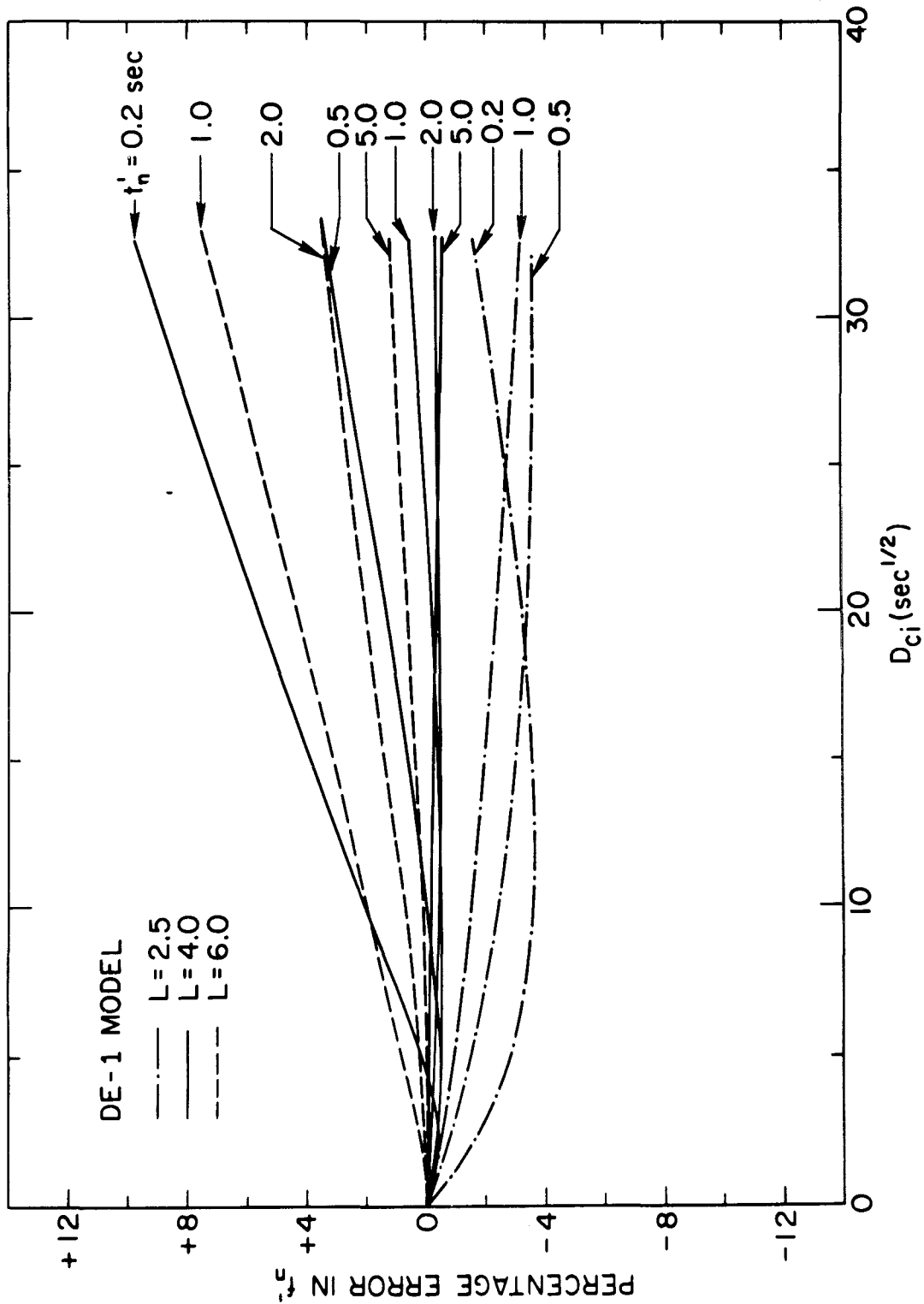
Figure 31. A plot of the percentage error in f'_n due to Eqn. (3.9) against D_{ci} for a range of values of L and t'_n.

70
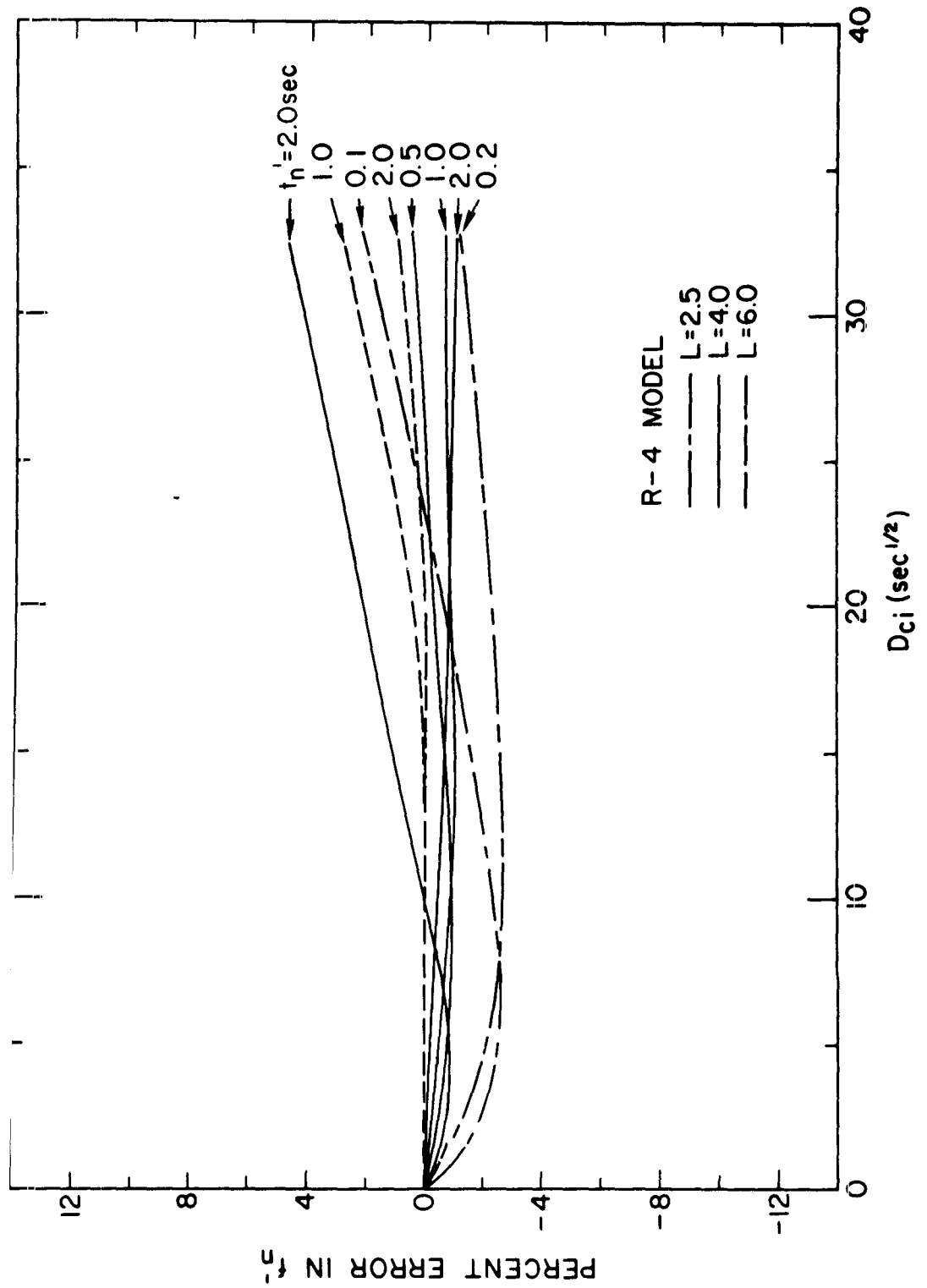
Figure 32. A plot of the percentage error in f' due to Eqn. (3.10) against D_{ci} for a range of values of L and $_n t'_n$.

and 32 correspond to extremely low electron concentrations in the magneto-sphere. For example, the solid curves marked $t'_n = 0.2$ sec are approaching the theoretical low limit of 0.18 sec which is the propagation time along the length of an $L = 4$ field line in free space. When electron concentrations are that low, errors due to other sources become more important than the error due to the empirical formulas given by Eqs. (3.9) and (3.10)(see Chapter 6).

We now consider expressions for t'_n. From Eq. (3.7),

$$t_n \simeq \bar{t'_n} + D_{ci} \, f_n^{-1/2} \simeq t'_n + D_{ci} \, f'^{-1/2}_n$$

Figure 33 is similar to Figure 25 except that the ionospheric dispersion is exaggerated in order to illustrate details near the nose frequency. It is evident in the figure that $t_n - t'_n$ is slightly less than $D_{ci} \, f'^{-1/2}_n$ but slightly greater than $D_{ci} \, f_n^{-1/2}$. A compromise is thus made:

$$t'_n = t_n - D_{ci} \left(\frac{f_n + f'_n}{2} \right)^{-1/2} \tag{3.11}$$

Equation (3.11) approximates the results of the previous section with less than 1 msec error for wide ranges of f_n, t_n and D_{ci}.
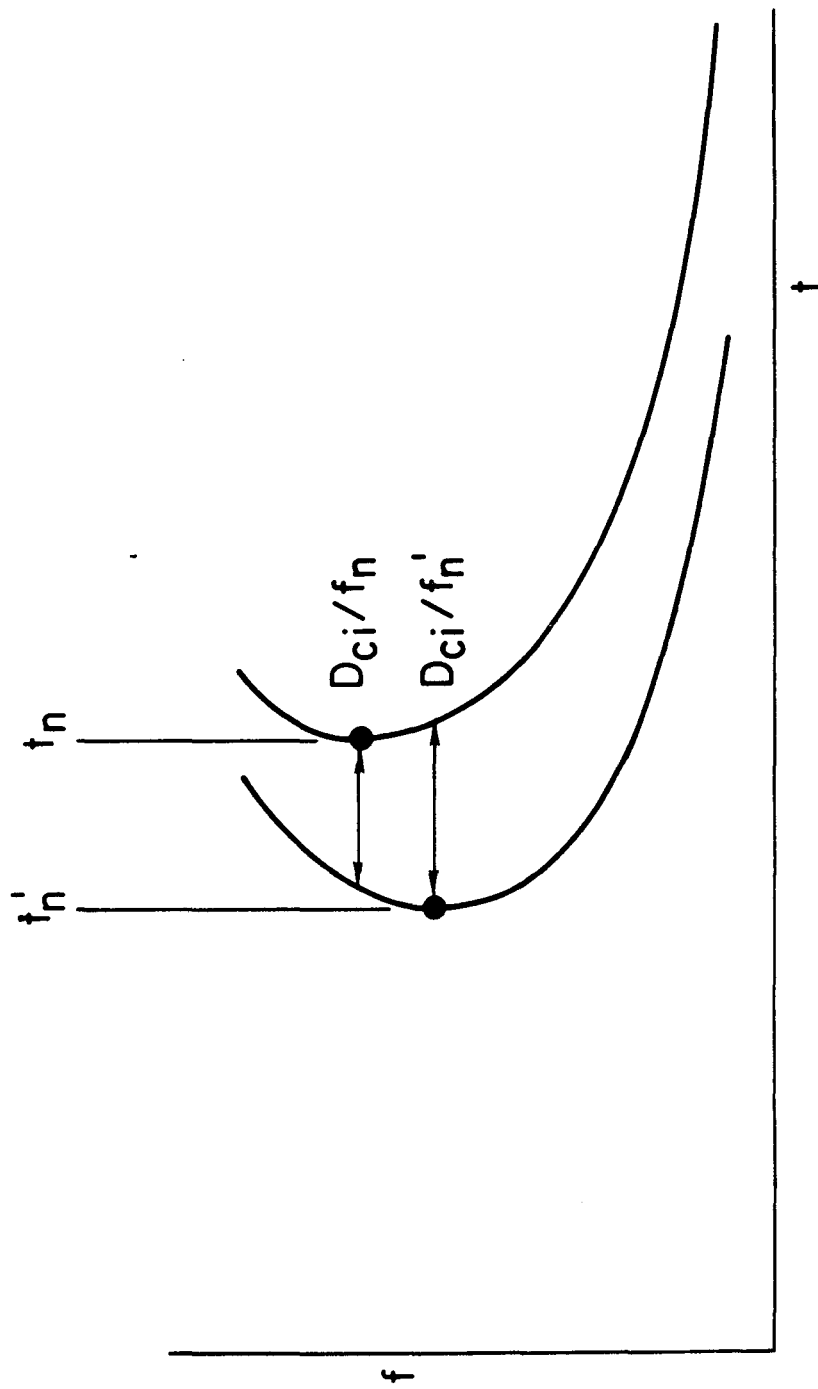
Figure 33. A sketch showing the effect of ionospheric dispersion on the minimum time delay of a nose whistler.

73

IV. SUBIONOSPHERIC PROPAGATION

The whistler travel time is usually measured with respect to the causative sferic on a whistler spectrogram, and it is necessary to account for the travel time of the signals in the earth-ionosphere waveguide. Figure 34 illustrates the geometry and the appearance of the sferic on a frequency-time spectrogram. At the top of the figure, R and T represent the locations of the whistler receiver and the sferic, respectively. A sferic often shows a small dispersion and a sharp low frequency cutoff as illustrated at the bottom of the figure. The cutoff occurs at the earth-ionosphere waveguide cutoff frequency which is 1.67 kHz for a lossless waveguide with a height of 90 km. The reader is referred to Helliwell [1965] for more detailed discussion of the dispersive effects of the earth-ionosphere waveguide. In this chapter, we estimate the subionospheric propagation time of the lightning signals that reach the whistler receiver. We will use t to denote the whistler travel time through the ionosphere and the magnetosphere and τ to denote the travel time of the whistler measured on a spectrogram with respect to the sferic.

We consider a simple case in which the lightning, whistler duct and the receiver are all in a magnetic meridional plane. The distance traveled by the direct wave can be written

$$\ell_D = \frac{\pi r_o}{180} (\phi_T + \phi_R) \tag{4.1}$$

where ϕ_T and ϕ_R are the magnetic latitude in degrees of the sferic and the receiver, respectively. The sign of the latitude is positive in both the northern and the southern hemispheres. The subionospheric distance traveled by the whistler wave is

$$\ell_w = \frac{\pi r_o}{180} \left(|\phi_T - \phi_D| + |\phi_R - \phi_D| \right) \tag{4.2}$$

where ϕ_D is the latitude of the end points of the whistler duct. The correction necessary for the subionospheric propagation is then

$$t - \tau = \frac{\ell_D - \ell_w}{c} \tag{4.3}$$

where c is the speed of light in a vacuum. Using Eqs. (4.1) and (4.2), the following equations are obtained:

$$t - \tau = 6.65 \times 10^{-4} \phi_D \text{ sec} \qquad \text{for } \phi_T \geq \phi_D \text{ and } \phi_R \geq \phi_D \tag{4.4}$$

$$t - \tau = 6.65 \times 10^{-4} \phi_R \text{ sec} \qquad \text{for } \phi_T \geq \phi_D \text{ and } \phi_R \leq \phi_D \tag{4.5}$$

$$t - \tau = 6.65 \times 10^{-4} \phi_R \text{ sec} \qquad \text{for } \phi_T \leq \phi_D \text{ and } \phi_R \geq \phi_D \tag{4.6}$$

$$t - \tau = 6.65 \times 10^{-4} (\phi_T + \phi_R - \phi_D) \text{ for } \phi_T \leq \phi_D \text{ and } \phi_R \leq \phi_D \tag{4.7}$$

For whistler receivers at high latitudes, ϕ_R is usually larger than ϕ_D, and therefore, Eq. (4.4) or Eq. (4.6) would apply. For $\phi_D = 60^\circ$ (L = 4), $t - \tau$ may vary from $0(\phi_T = 0)$ to 0.04 sec ($\phi_T = 60^\circ$) depending on ϕ_T. Since ϕ_T is usually not known, a constant value of $t - \tau = 0.03$ sec may be used for all medium to high latitude whistlers as a first order correction.

If we remove the assumption that the sferic and the duct lie in the same meridian plane as the receiver, the distances ℓ_D and ℓ_w should be great circle distances. However, in view of the fact that no means of identifying the location of sferics and the longitude of whistler ducts are available at present, we will not consider such refinements here.
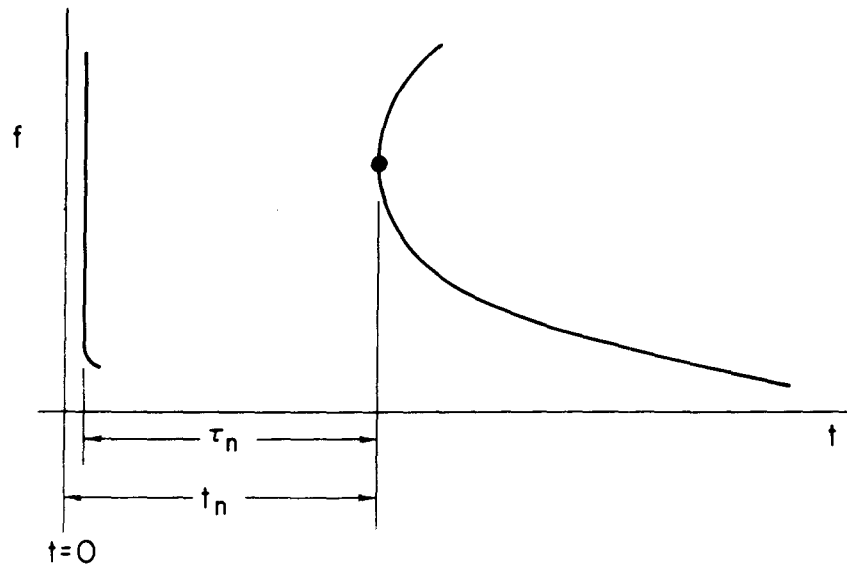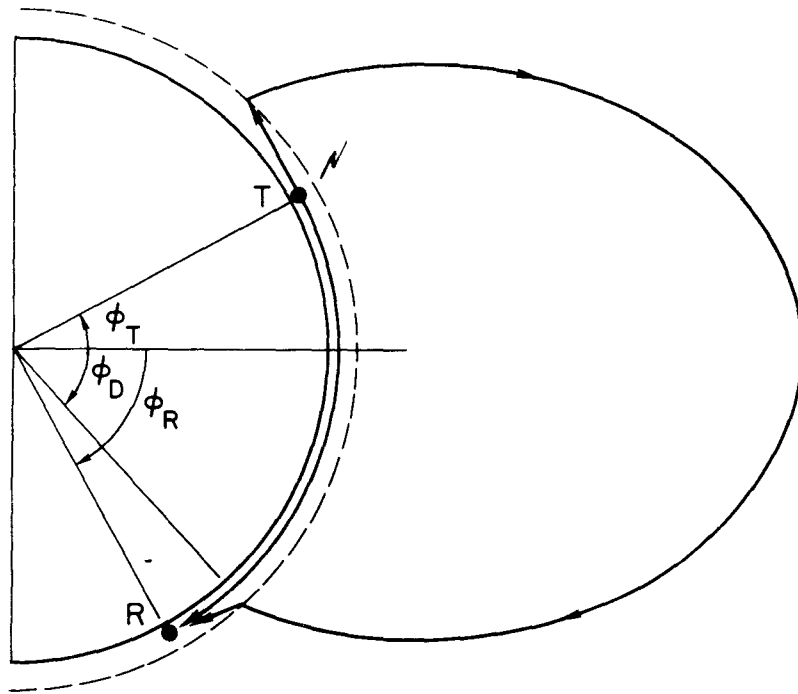
Figure 34. The sketch at the top shows a whistler mode and a wave-
guide mode propagation paths of lightning signal from
its source T to the receiver R in the conjugate hemisphere. The bot-
tom sketch shows how the received signal appears on a frequency-time
spectrogram. The wave-guide mode signal shows the effect of the wave-
guide cutoff at low frequencies.

76

V. SUMMARY

In this chapter, we briefly summarize the procedures for determining the path latitude and electron concentration along the path from the whistler parameters f_n and t_n.

1. Scale f_n and τ_n from whistler spectrogram.

2. Make corrections for subionospheric propagation as discussed in Chapter 4 to obtain t_n. Typically, $t_n = \tau_n + 0.03$ sec.

3. Decide on a magnetospheric electron concentration model to be used.

4. Estimate dispersion in the two conjugate ionospheres D_{ci} as discussed in Chapter 3.

5. Make corrections for the ionospheric dispersion to obtain f_n' and t_n' as follows:

(a) for diffusive equilibrium models (DE-1 through DE-4)

$$f_n' = \frac{f_n}{1 + \left(\dfrac{0.17 \, D_{ci}}{t_n f_n^{1/3}} \right)} \tag{5.1}$$

$$t_n' = t_n - D_{ci} \left(\frac{f_n + f_n'}{2} \right)^{-1/2} \tag{5.2}$$

(b) for collisionless models (CL and R-4 models)

$$f_n' = \frac{f_n}{1 + \left(\dfrac{0.15 \, D_{ci}}{t_n f_n^{1/3}} \right)} \tag{5.3}$$

$$t_n' = t_n - D_{ci} \left(\frac{f_n + f_n'}{2} \right)^{-1/2}$$

6. L, n_{eq}, N_T and n_1 can be obtained from f'_n and t'_n by one of the following methods depending on the desired precision and availability of a computer or a calculator.

(a) L, n_{eq} and N_T are read off the graphs in Figures 7, 8 and 9 for DE models and Figures 7, 10 and 11 for the CL model or R-4 model. n_1 is obtained from n_{eq} using Figure 12.

(b) Calculate L, n_{eq}, N_T and n_1 using the following formulas

$$f_{Heq} = K \, f'_n \qquad\qquad (5.4)$$

$$L = \left(\frac{8.736 \times 10^5}{f_{Heq}} \right)^{1/3} \qquad\qquad (5.5)$$

$$n_{eq} = K_{eq} \, \frac{f'_n \, t'^2_n}{L^5} \qquad\qquad (5.6)$$

$$N_T = K_T \, \frac{f'_n \, t'^2_n}{L} \qquad\qquad (5.7)$$

$$n_1 = K_1 \, \frac{f'_n \, t'^2_n}{L^5} \qquad\qquad (5.8)$$

using the values of K, K_{eq}, K_T and K_1 obtained from Figures 14 through 21.

(c) Use Eqs. (5.4) through (5.8) above, but obtain the values of K's from empirical formulas of the form $K = a_o + a_1 F + a_2 F^2$ where $F = \log_{10} f'_n$. The coefficient a's are given in Tables 9 and 10 for the DE-1 model and R-4 model.

VI. UNCERTAINTIES IN THE WHISTLER METHOD

A. INTRODUCTION

In this chapter, we discuss uncertainties in the whistler method described in this report. A few general remarks will be followed by more detailed examination of various sources of error.

As mentioned earlier in Chapter 2, whistlers are most sensitive to the conditions at the top of the propagation path. To illustrate this, we return to Eq. (1.2). At the nose frequency,

$$t_n = \frac{1}{c f_n^{1/2}} \int \frac{f_p}{f_H^{1/2}(1 - \frac{f_n}{f_H})^{3/2}} ds$$

From the results of Chapter 2, $f_n \simeq 0.377 \, f_{Heq}$ for diffusive equilibrium models, so t_n is approximately proportional to

$$\int \frac{f_p}{f_H^{1/2}(1 - 0.377 \frac{f_{Heq}}{f_H})^{3/2}} ds$$

Figure 35 is a plot of the value of the integrand,

$$I = \frac{f_p}{f_H^{1/2} \left(1 - 0.377 \frac{f_{Heq}}{f_H}\right)^{3/2}}$$

normalized to the equatorial value, as a function of distance along lines of force for several L-values. The DE-1 Model was used for the electron distribution along field lines. The terminal point of each curve corresponds to 1000 km altitude, and the circle on each curve to 30° dipole latitude. The whistler time delay is proportional to the area under the curve, and it can be seen that nearly 80% of the time delay occurs within
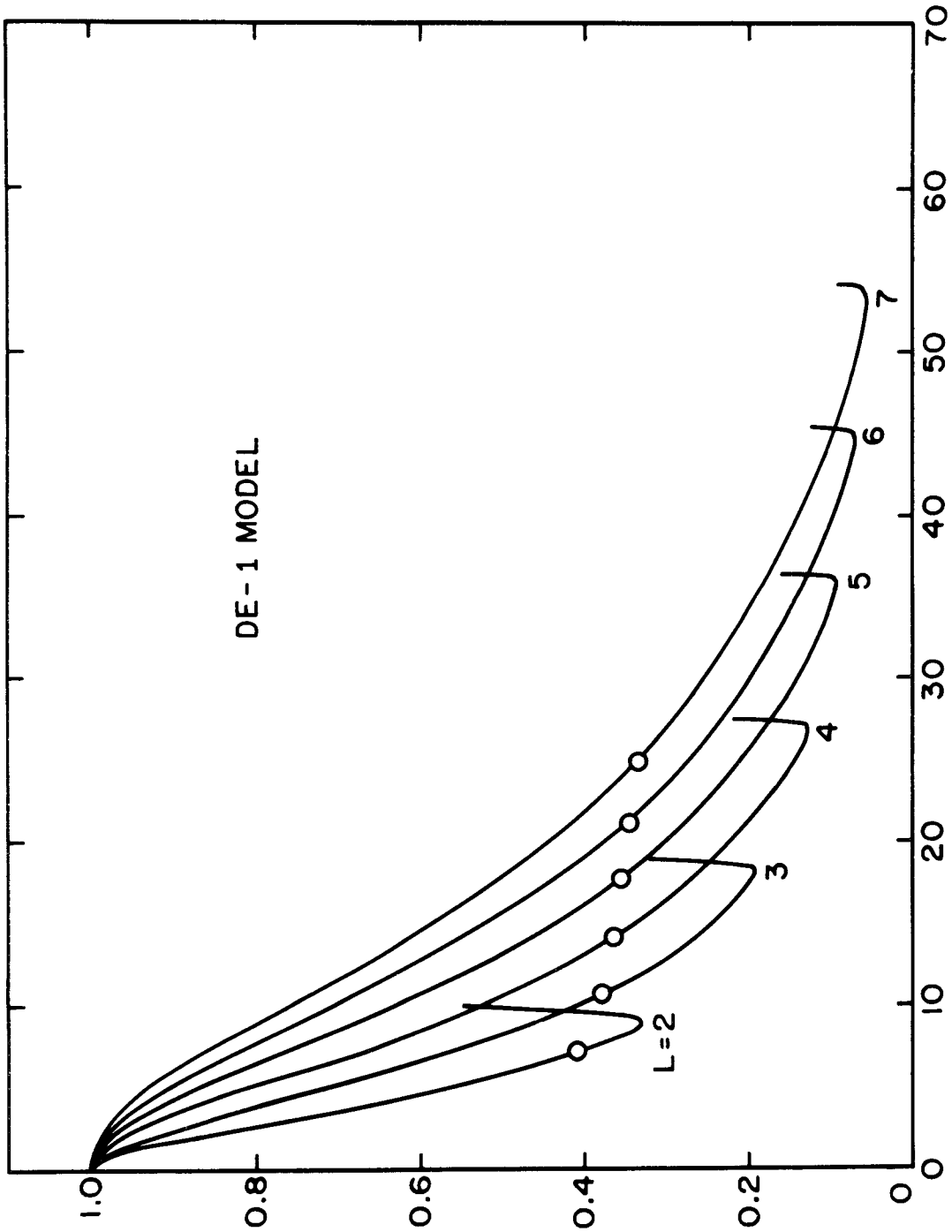
Figure 35.   A plot of the whistler integrand I (see text) as a function of
distance along field lines at several L values.   The distance is
measured from the equator, and the values of I are normalized to the equatorial
value.   The curves terminate at 1000 km altitude, and the circles indicate 30°
in latitude.

$\sim 30^{\circ}$ of the equator. The sharp 'hooks' in the curves are due to rapid increases in electron concentration near the base of the magnetosphere. If a diffusive equilibrium model with different parameters (temperature and ionic composition) is used, there are changes in the shape of the 'hocks', but little effect at distances greater than 1000 km from the base of the magnetosphere. For collisionless models, $f_n \cong 0.41\ f_{Heq}$, and the

quantity $I = \dfrac{f_p}{f_H^{1/2}\left(1 - 0.41\ \dfrac{f_{Heq}}{f_H}\right)^{3/2}}$ has been calculated at several

L-values and is plotted in Figure 36. In this case, $\sim 60\%$ of whistler propagation delay occurs within 30° of the equator. Because of these facts, electron concentration near the equator as measured by the whistler technique is remarkably independent of assumed electron distribution along field lines. On the other hand, electron concentration near the base of the magnetosphere depends sensitively on assumed models.

Information on electron concentration in the magnetosphere usually involves extrapolation along magnetic field lines by assumed models. For example, electron concentration measured near the base of the magnetosphere by incoherent backscatter radars, satellite-borne sounders or probes can be extrapolated to the equatorial plane. When computing magnetospheric tube content, however, the whistler technique has the advantage of measuring electron concentration accurately near the equatorial plane where most of the tube volume lies.

We now examine more quantitatively various sources of uncertainties in the whistler method.

B. UNCERTAINTIES DUE TO THE ASSUMED ELECTRON CONCENTRATION MODEL

For given f_n' and t_n', Eqs. (5.4) through (5.8) can be written in dif-
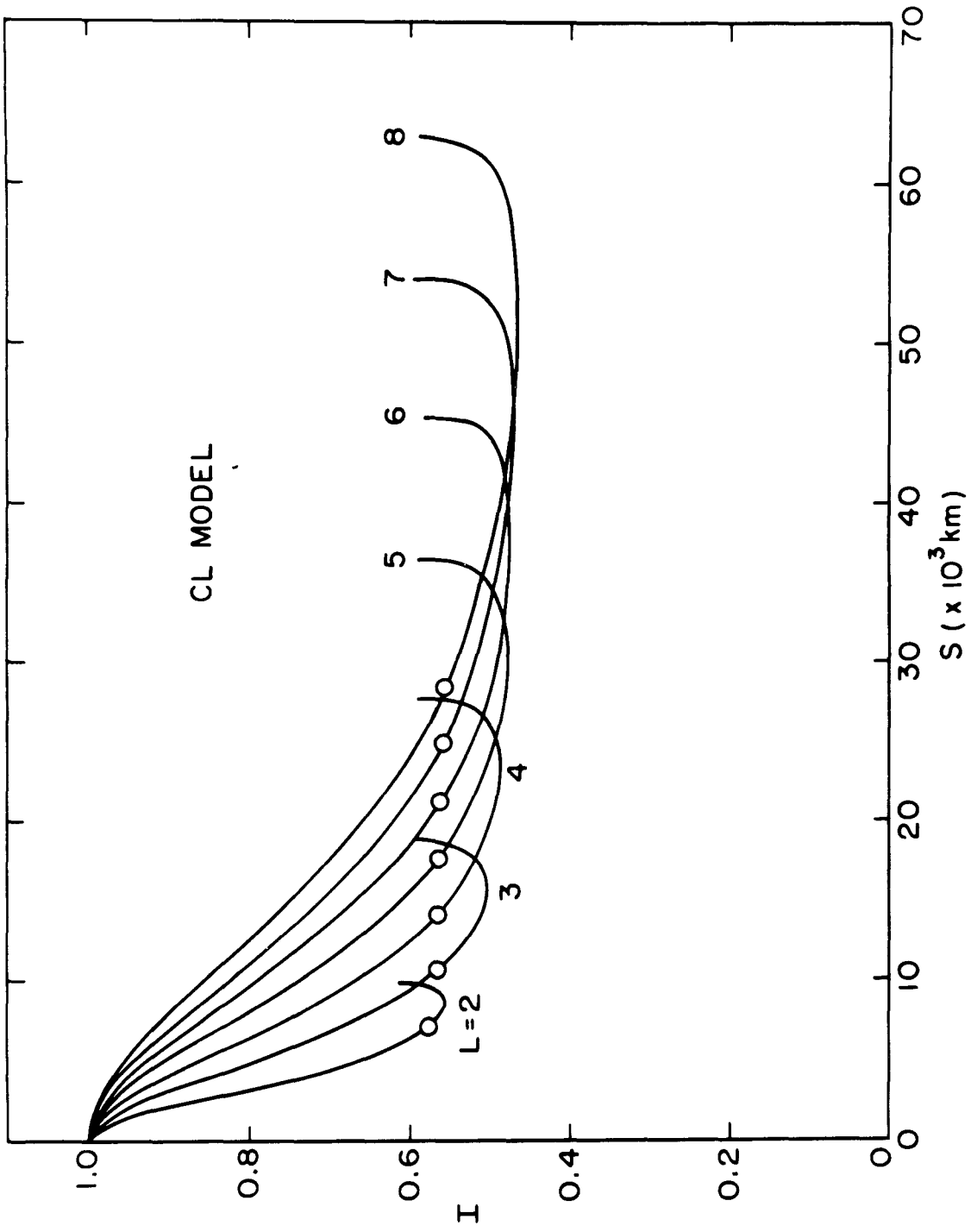
Figure 36. A plot similar to Figure 35 but for the CL model of field-line
distribution of plasma.

ferential form as follows:

$$\frac{\Delta f_{Heq}}{f_{Heq}} = \frac{\Delta K}{K}$$

$$\frac{\Delta L}{L} = -\frac{1}{3} \frac{\Delta f_{Heq}}{f_{Heq}} = -\frac{1}{3} \left(\frac{\Delta K}{K}\right)$$

$$\frac{\Delta n_{eq}}{n_{eq}} = \left(\frac{\Delta K_{eq}}{K_{eq}}\right) + \frac{5}{3} \left(\frac{\Delta K}{K}\right)$$

$$\frac{\Delta N_T}{N_T} = \left(\frac{\Delta K_T}{K_T}\right) + \frac{1}{3} \left(\frac{\Delta K}{K}\right)$$

$$\frac{\Delta n_1}{n_1} = \left(\frac{\Delta K_1}{K_1}\right) + \frac{5}{3} \left(\frac{\Delta K}{K}\right)$$

The ΔK's in the above equations represent differences between electron concentration models, and their values can be obtained from Figure 14 through 21. For a whistler with observed f_n, f_n' depends somewhat on the electron concentration model used (see Eqs. 5.1 and 5.3), but this is a small effect and will be ignored. An example given below illustrates the effects of changing the model from DE-2 (3200 $^\circ$K, 90% O^+, 8% H^+, 2% He^+) to DE-3 (1600 $^\circ$K, 50% O^+, 40% H^+, 10% He^+) for a whistler with $f_n' = 5$ kHz. From Figures 14 through 17, we obtain

$$\frac{\Delta K}{K} = -0.012, \quad \frac{\Delta K_{eq}}{K_{eq}} = -0.071, \quad \frac{\Delta K_T}{K_T} = -0.027 \text{ and } \frac{\Delta K_1}{K_1} = -0.17$$

Substitution of these values into the above equations yields

$$\frac{\Delta L}{L} = -0.004, \quad \frac{\Delta n_{eq}}{n_{eq}} = -0.091, \quad \frac{\Delta N_T}{N_T} = -0.031 \quad \text{and} \quad \frac{\Delta n_1}{n_1} = -0.19$$

It is seen that N_T and n_{eq} are relatively insensitive to changes in model, whereas n_1 is more model-dependent.

C. MEASUREMENT ERROR

We assume that measurement errors in f_n and t_n result in the same percentage errors in f'_n and t'_n. Since the K's in Eqs. (5.4) through (5.8) are only very slow functions of f'_n, we further assume that the K's are constant within the range of measurement errors in f_n. Equations (5.4) through (5.8) can then be written in differential form as

$$\frac{\Delta f_{Heq}}{f_{Heq}} = \frac{\Delta f'_n}{f'_n}$$

$$\frac{\Delta L}{L} = -\frac{1}{3} \left(\frac{\Delta f'_n}{f'_n} \right) \tag{6.1}$$

$$\frac{\Delta n_{eq}}{n_{eq}} = 2 \left(\frac{\Delta t'_n}{t'_n} \right) + \frac{8}{3} \left(\frac{\Delta f'_n}{f'_n} \right) \tag{6.2}$$

$$\frac{\Delta N_T}{N_T} = 2 \left(\frac{\Delta t'_n}{t'_n} \right) + \frac{4}{3} \left(\frac{\Delta f'_n}{f'_n} \right) \tag{6.3}$$

$$\frac{\Delta n_1}{n_1} = 2 \left(\frac{\Delta t'_n}{t_n} \right) + \frac{8}{3} \left(\frac{\Delta f'_n}{f'_n} \right) \tag{6.4}$$

In routine scaling, measurement errors can be easily maintained below $\sim 3\%$ for f'_n and $\sim 1\%$ for t'_n. Equations (6.1) through (6.4) show that a 1% error in t'_n causes a 2% error in computed n_{eq}, N_T and n_1. An error of 3% in f'_n causes a 1% error in the computed L-value, a 4% error in N_T and 8% errors in n_{eq} and n_1. With high quality whistler traces and sufficient care in scaling, measurement accuracies can be improved over the figures quoted above.

D. UNCERTAINTIES DUE TO THE IONOSPHERE

Uncertainties in ionospheric dispersion appear as uncertainties in f'_n and t'_n. From Eqs. (5.1) and (5.3), we can write

$$\frac{\Delta f'_n}{f'_n} = \frac{-0.17}{t_n f_n^{1/3}} \Delta D_{ci} \qquad \text{for DE models and}$$

$$\frac{\Delta f'_n}{f'_n} = \frac{-0.15}{t_n f_n^{1/3}} \Delta D_{ci} \qquad \text{for collisionless models.}$$

From Eq. (5.2)

$$\frac{\Delta t'_n}{t'_n} = - \frac{1}{t_n f_n^{1/2}} \Delta D_{ci} \qquad \begin{array}{l}\text{for both DE models and} \\ \text{collisionless models.}\end{array}$$

Equations (6.1) through (6.4) can then be used to estimate uncertainties in L, n_{eq}, N_T and n_1.

As an example, consider a whistler propagating in the plasmasphere (DE model) with $f_n = 6$ kHz ($L \sim 4$) and $t_n = 1$ sec. An overestimate of D_{ci} by 1 $\text{sec}^{-1/2}$ results in $\frac{\Delta f'_n}{f_n} = -0.009$ and $\frac{\Delta t'_n}{t'_n} = - 0.002$. Substituting these values into Eqs. (6.1) through (6.4), we obtain

$$\frac{\Delta L}{L} = 0.003, \quad \frac{\Delta n_{eq}}{n_{eq}} = -0.028, \quad \frac{\Delta N_T}{N_T} = -0.016 \text{ and } \frac{\Delta n_1}{n_1} = -0.028$$

In addition to uncertainties in D_{ci}, the empirical approximation of Eqs. (5.1) and (5.3) introduces small errors in f_n'. The magnitude of this error depends on magnetospheric parameters and D_{ci} (see Section 3D) and can be estimated with the aid of Figures 31 and 32.

E.   UNCERTAINTIES DUE TO SUBIONOSPHERIC PROPAGATION

Whistler propagation in the earth-ionosphere wave guide has negligible effects on f_n unless f_n approaches the wave guide cutoff frequency of ~ 1.6 kHz. Corrections for subionospheric propagation, however, must be made to time delays measured on a whistler spectrogram. As discussed in Chapter 4, the amount of correction necessary is typically ~ 0.03 sec with uncertainties of ~ 0.015 sec due to uncertainties in the location of lightning. For $t_n = 1.5$ sec, this corresponds to $\frac{\Delta t_n'}{t_n'} \sim 0.01$, and from Eqs. (6.2) through (6.4), $\frac{\Delta n_{eq}}{n_{eq}} = \frac{\Delta N_T}{N_T} = \frac{\Delta n_i}{n_1} \sim 0.02$.

F.   SUGGESTIONS FOR FURTHER WORK

A number of simplifying assumptions were made in this study in order to facilitate calculations and arrive at simple recipes for routine processing of whistler data. It was also necessary to use several models for electron distribution along geomagnetic lines of force. When a need arises for improved accuracy in whistler methods, these models and assumptions must be re-examined critically.

As mentioned previously, there is empirical evidence in support of a diffusive equilibrium model inside the plasmapause under normal conditions. Outside the plasmapause, however, the idealized collisionless model used

here is probably extreme, and the actual situation may be better represented by a model falling between the collisionless model and the diffusive equilibrium model (see Section 2B). Banks, et al [1971] recently pointed out a theoretical possibility that a low plasma pressure outside the plasmapause following a magnetic storm may cause the ionospheric plasma to flow upward at supersonic speeds. The field line distribution of plasma may be very complicated under such circumstances. More detailed theoretical and experimental studies are needed to improve the electron concentration models used outside the plasmapause.

The expression for refractive index used in this study is for a cold plasma, and it is further simplified by neglecting the additive 1 in Eq. (1.1) on the assumption that plasma frequency is much higher than electron gyrofrequency. These assumptions need further critical examination outside the plasmapause, where electron concentrations are low and the temperatures are high.

Another important simplification made in this study is the use of a dipole magnetic field. At large L values and during magnetic disturbances, the earth's magnetic field is distorted significantly by the solar wind, and the ring current. A detailed investigation should be made of whistler propagation in distorted magnetic fields and the possibility of detecting such distortions by the whistler technique.

An improvement is desired in estimating subionospheric propagation time and correcting for the effect of wave guide dispersion on nose frequency when the nose frequency is close to the wave guide cutoff frequency.

SEL-71-058

APPENDIX. DIPOLE GEOMETRY

A. MAGNETIC FIELD STRENGTH

In a centered dipole approximation, the earth's magnetic field strength is given by

$$B = 0.312 \ (r_o/r)^3 (1 + 3 \sin^2\phi)^{1/2} \quad \text{gauss} \qquad (A.1)$$

where ϕ is the latitude, r the geocentric distance and r_o the mean radius of the earth, 6370 km. Figure 3 illustrates the dipole geometry and the symbols used. The electron gyrofrequency is given by

$$f_H = \frac{1}{2\pi} \frac{Be}{m} = 8.736 \times 10^5 \ (r_o/r)^3 (1 + 3 \sin^2\phi)^{1/2} \quad \text{Hertz}$$

$$(A.2)$$

Figure 37 shows the equatorial field strength B_{eq} (and f_{Heq}) plotted against r_{eq}, while Figure 38 shows the latitudinal variation of the field strength at the earth's surface B_o.

B. L-VALUE

A dipole field line is described by

$$\frac{r}{\cos^2\phi} = \frac{r_o}{\cos^2\phi_o} \qquad (A.3)$$

where the subscript o refers to the earth's surface. In a dipole, McIlwain's L parameter is

$$L = \frac{r_{eq}}{r_o} = \frac{1}{\cos^2\phi_o} \qquad (A.4)$$
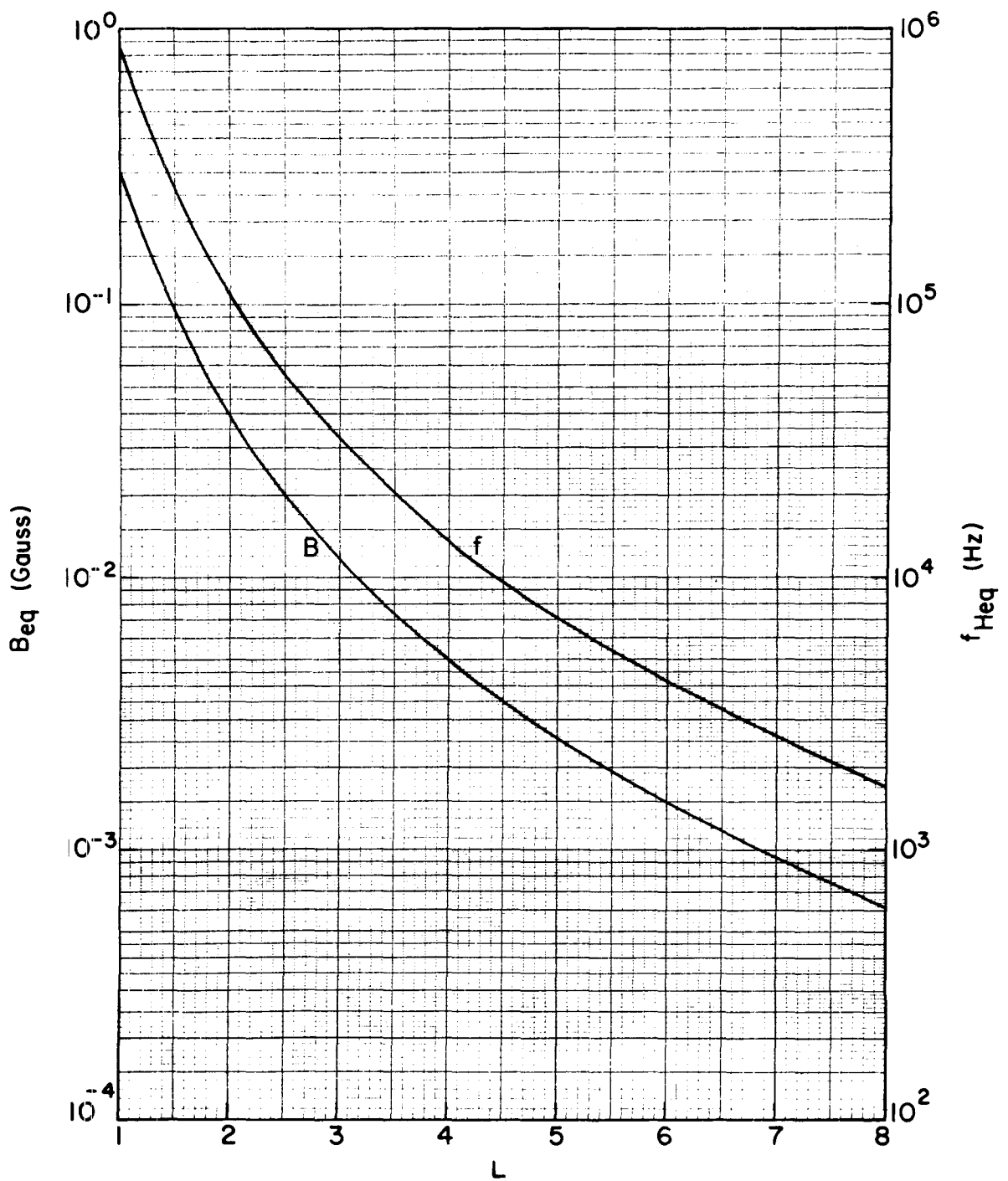
Figure 37. A plot of the earth's magnetic field strength and electron gyrofrequency at the equator as a function of L according to a centered dipole model.

89
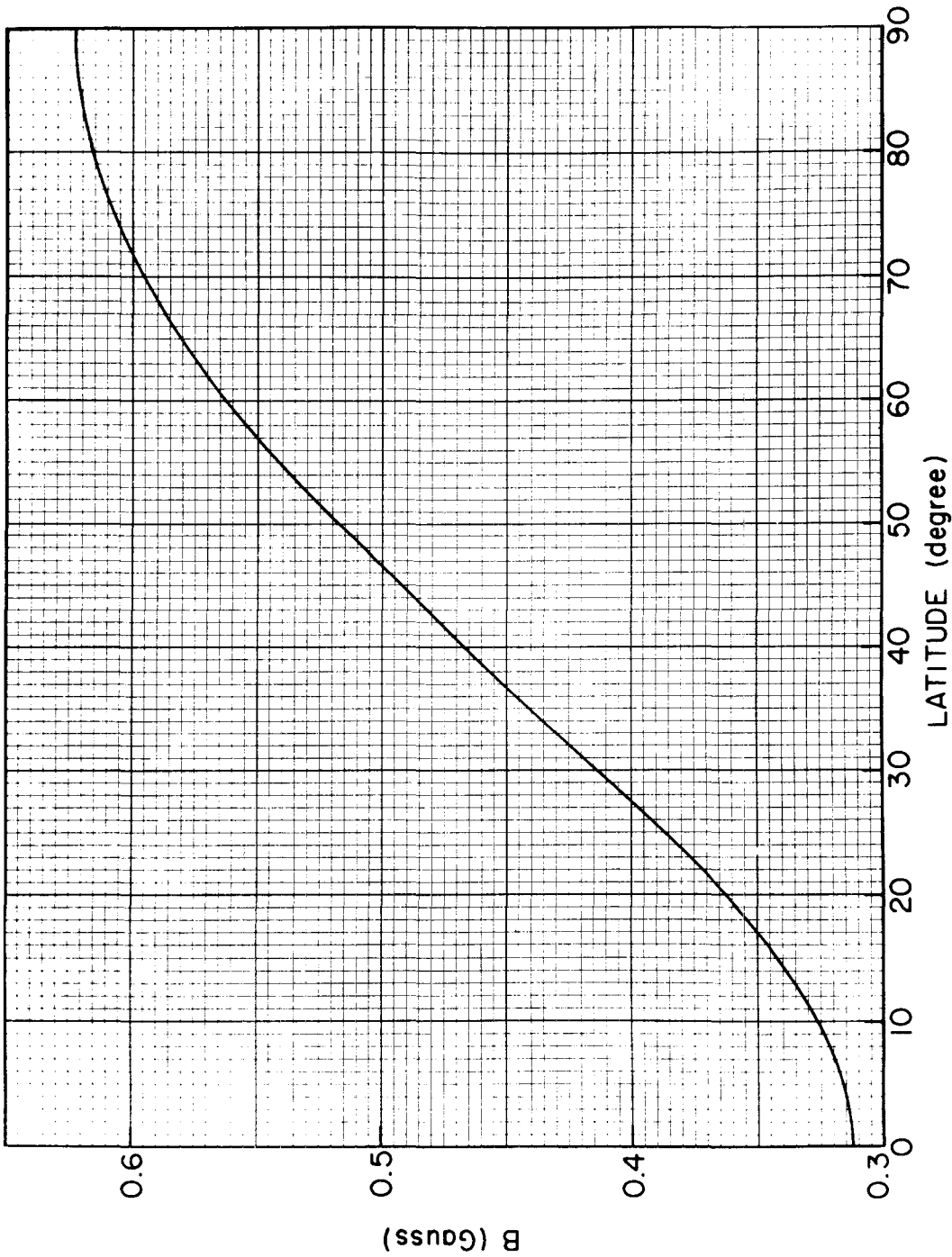
Figure 38. A plot of a dipole magnetic field strength on the earth's surface as a function of latitude.

If the reference level is changed to 1000 km altitude, ϕ_1 can be substituted for ϕ_0 by using Eq. (A.3) and we obtain

$$L = \frac{r_1}{r_0} \frac{1}{\cos^2\phi_1} \qquad (A.5)$$

Figure 39 shows plots of ϕ_0 and ϕ_1 versus L-value.

C. DIP ANGLE

The radial and tangential components of B are given by

$$\left. \begin{array}{l} B_r = 0.624 \ (r_0/r)^3 \cos\theta \\ \\ \\ B_\theta = 0.312 \ (r_0/r)^3 \sin\theta \end{array} \right\} \qquad (A.6)$$

These vector components are related to dip angle δ by

$$\tan\delta = \frac{B_r}{B_\theta} = 2 \ \cot\theta = 2\tan\phi \qquad (A.7)$$

Figure 40 is a plot of δ as a function of ϕ. The horizontal scale at top is the L-value at the earth's surface.

D. LENGTH OF FIELD LINES

The arc length along a dipole field line between the equator and ϕ can be written as (see Helliwell [1965])

$$S = \frac{1}{2\sqrt{3}} \frac{r_0}{\cos^2\phi_0} \ (x + \sinh x \ \cosh x) \qquad (A.8)$$

where $\sinh x = \sqrt{3 \ \sin\phi}$. By substituting $\sinh x = (e^x - e^{-x})/2$ and $\cosh x =$
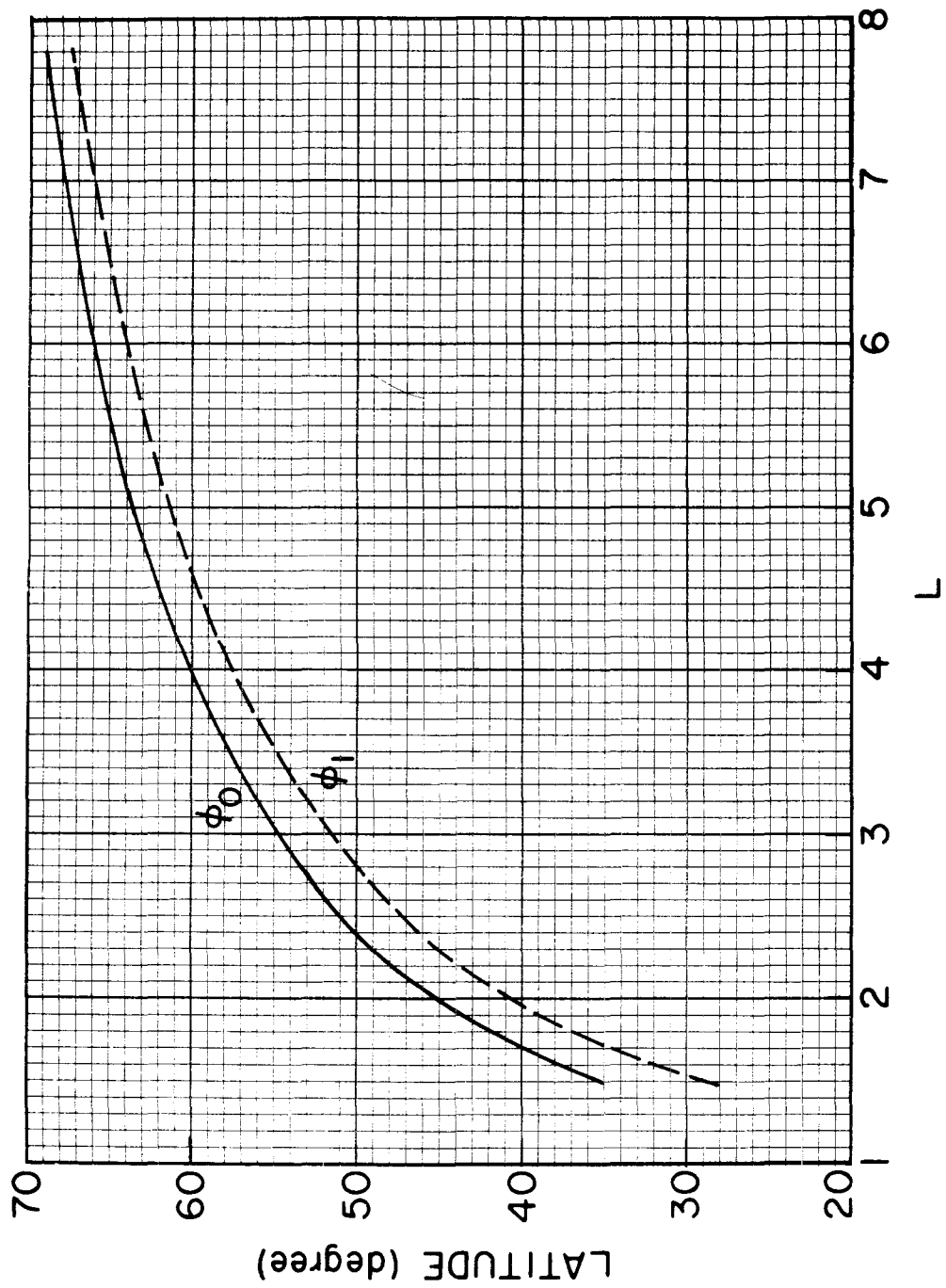
Figure 39. A plot of the latitude where the earth's magnetic field lines inter-sect the earth's surface (ϕ_o) and the 1000 km level (ϕ_1) as a function of dipole L parameter.
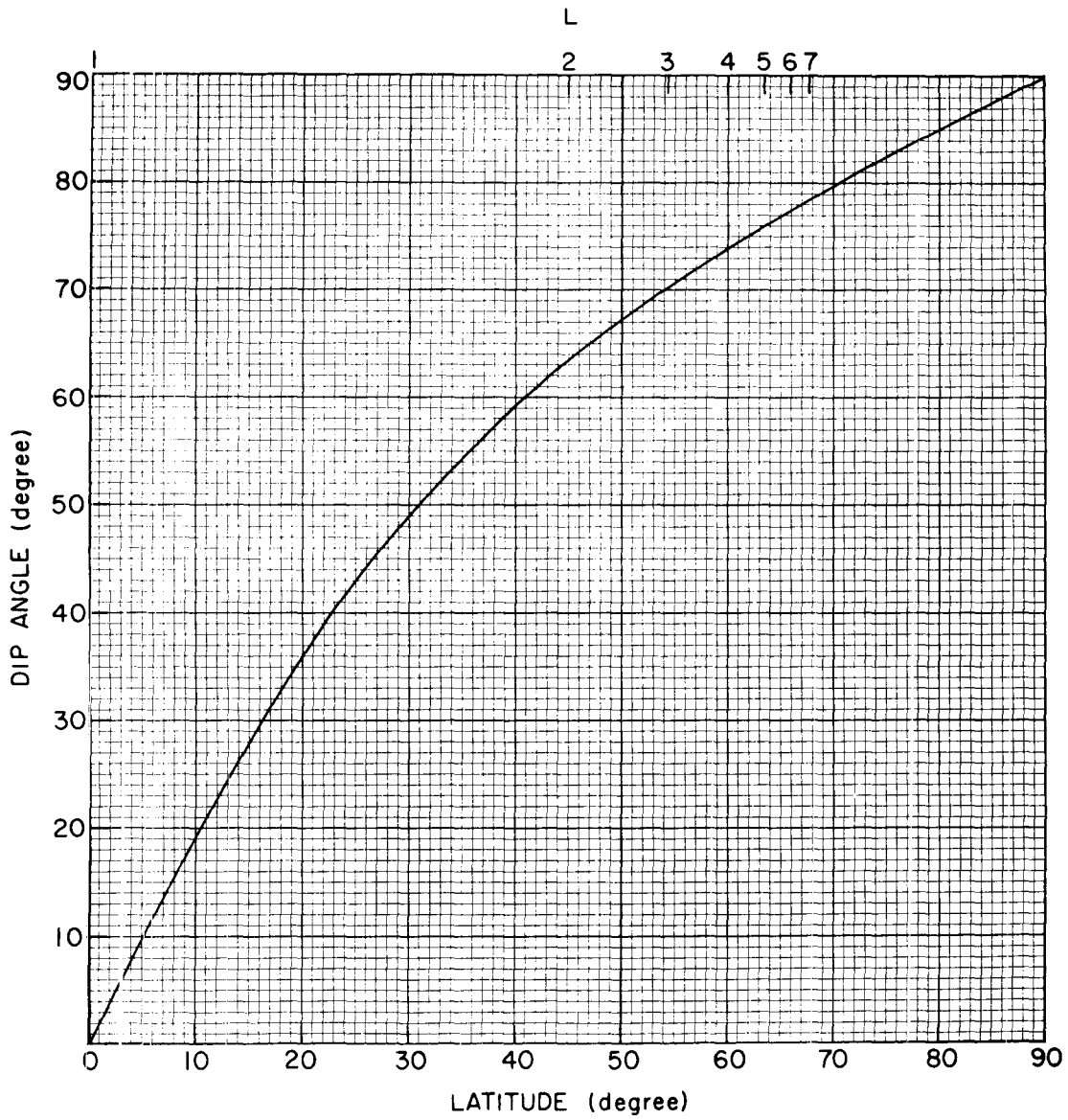
Figure 40.   A plot of the dip angle as a function of latitude for a dipole field. The horizontal scale at the top shows dipole L parameter.

$(e^x + e^{-x})/2$, and using the identity $\cosh^2 x - \sinh^2 x = 1$. Eq. (A.8) can be rewritten as

$$S = \frac{1}{2\sqrt{3}} \quad \frac{r_o}{\cos^2 \phi_o} \left[\ln\left(\sqrt{3} \sin\phi + \sqrt{1 + 3 \sin^2\phi} \right) + \sqrt{3} \sin\phi \sqrt{1 + 3 \sin^2\phi} \right]$$

(A.9)

Figure 41 shows a plot of the arc length measured from the dipole equator as a function of latitude for several L-values. Figure 42 shows the arc length from the equator to the 1000 km level S_1 plotted against L.

E. TUBE VOLUME

We define V as the volume of a tube of force with 1 cm^2 cross-sectional area at 1000 km and extending to the equator. We write

$$V_T = \int_{1000 \text{ km}}^{\text{equator}} \frac{B_1}{B} \, ds$$

and use Eqs. (A.1) and (2.15) to obtain

$$V_T = \frac{r_o^4 L^4}{r_1^3} \left(1 + 3 \sin^2\phi_1 \right)^{1/2} \int_0^{\phi_1} \cos^7\phi \, d\phi$$

The integration yields
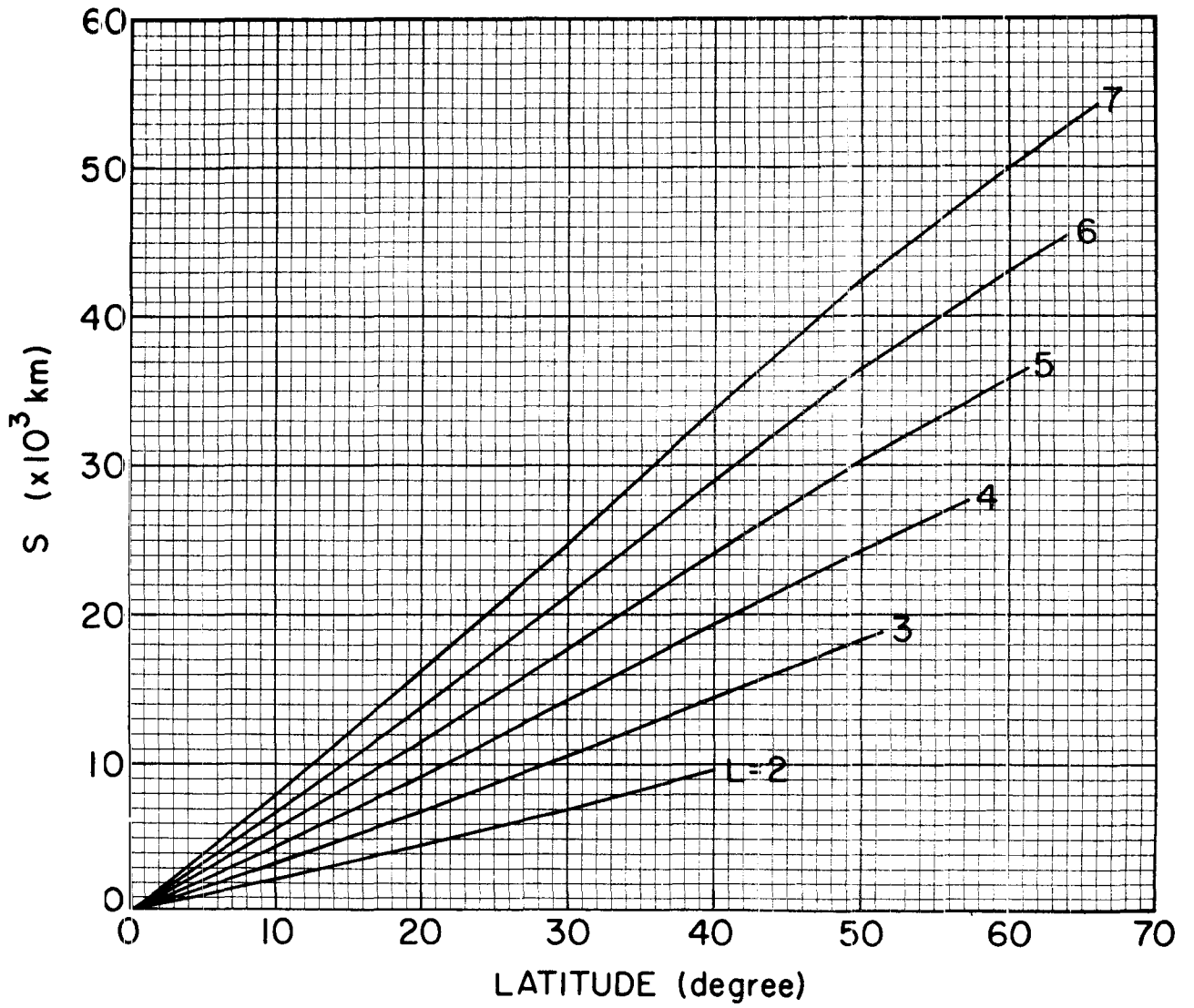
Figure 41. A plot of the arc length of the earth's dipole field lines as a
function of latitude for several L values.
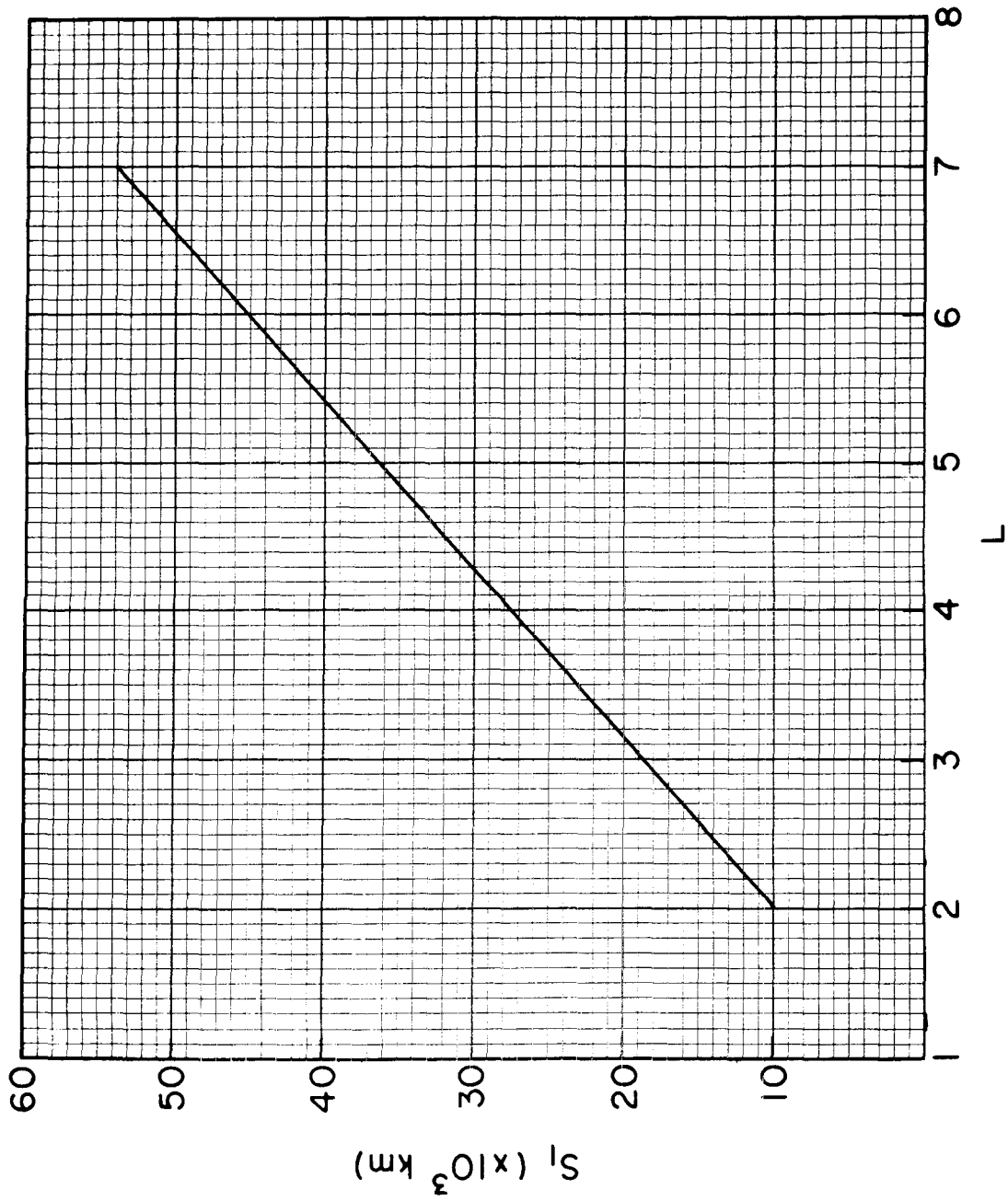
Figure 42.   A plot of the arc length of the earth's dipole field lines between the equator and 1000 km altitude as a function of dipole L parameter.

96

$$V_T = \frac{r_o^4 \, L^4}{r_1^3} \, (1 + 3 \sin^2\phi)^{1/2} \left[\frac{35}{64} \sin\phi_1 + \frac{7}{64} \sin3\phi_1 + \frac{7}{320} \sin5\phi_1 + \right.$$

$$\left. \frac{1}{448} \sin7\phi_1 \right] \qquad\qquad\qquad (A.10)$$

Figure 43 shows a plot of V_T versus L.
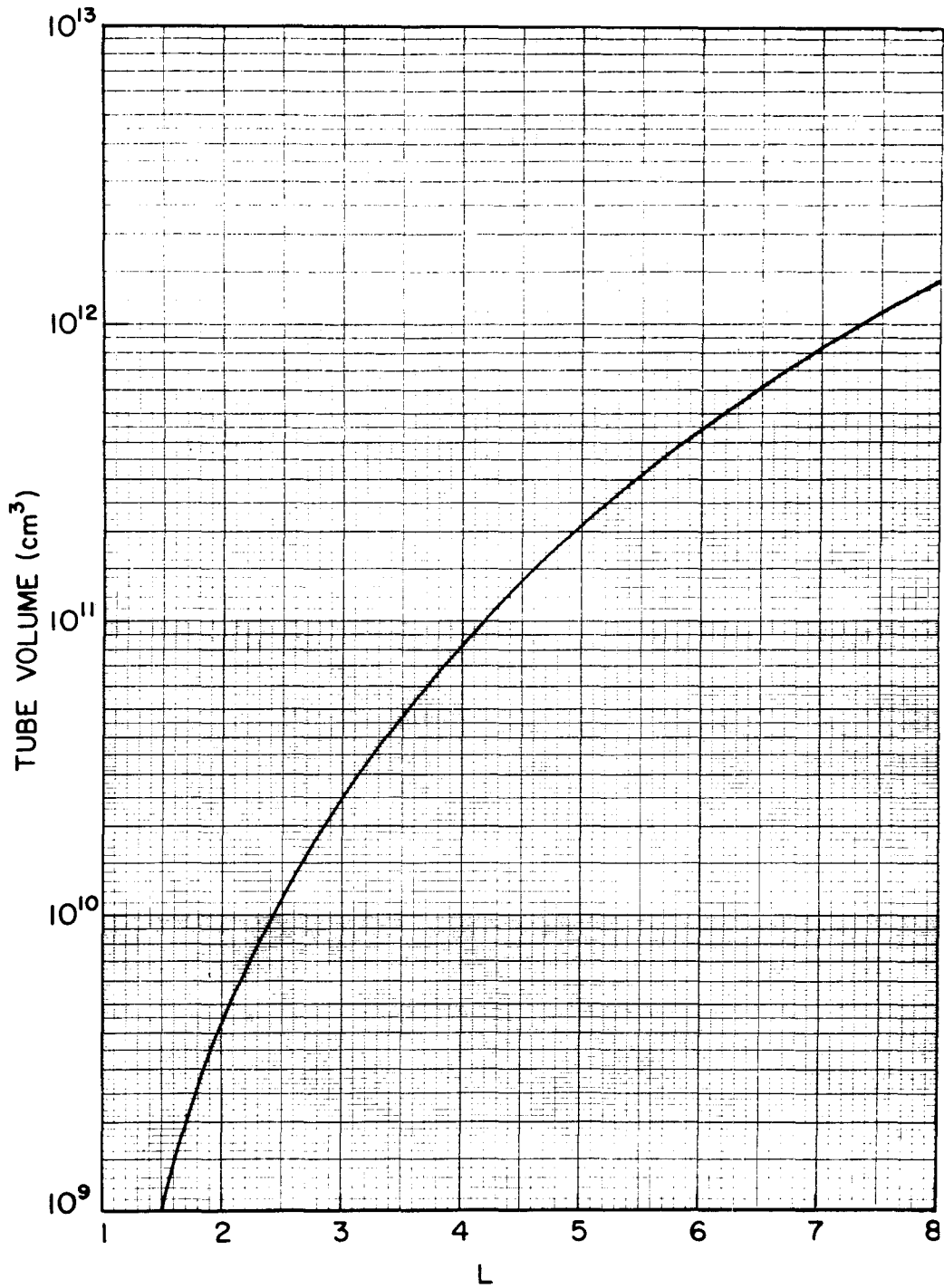
Figure 43. A plot of tube volume against dipole L parameter. The tube has 1 cm^2 cross-sectional area at 1000 km altitude and extends to the equatorial plane.

REFERENCES

Angerami, J. J., A whistler study of the distribution of thermal electrons in the magnetosphere, SEL-66-017, Radioscience Lab., Stanford Electronics Labs., Stanford University, Stanford, Calif., May 1966.

Angerami, J. J. and D. L. Carpenter, Whistler studies of the plasmapause in the magnetosphere-2; equatorial density and total tube electron content near the knee in magnetospheric ionization, J. Geophys. Res., 71,(3), 711-25, Feb. 1966.

Angerami, J. J. and J. O. Thomas, The distribution of ions and electrons in the earth's exosphere, Radioscience Lab., Stanford Electronic Labs., Stanford University, Stanford, Calif., December 1963.

Banks, P. M., A. F. Nagy and W. I. Axford, Dynamical behavior of thermal protons in the midlatitude ionosphere and magnetosphere. Planet Space Sci., 19, 1053, 1971.

Bernard, L. C., A simple approximation to whistler dispersion and its application to the nose extension method, in preparation, 1971.

Carpenter, D. L., The magnetosphere during magnetic storms; a whistler analysis, Ph.D. Thesis, Stanford University, Tech. Report No. 12, Radioscience Lab., Stanford University, Stanford, Calif., June 1962.

Carpenter, D. L., Whistler evidence of a 'knee' in the magnetospheric ionization density profile, J. Geophys. Res., 68, 1675, 1963.

Carpenter, D. L. Whistler studies of the plasmapause in the magnetosphere -1; temporal variations in the position of the knee and some evidence on plasma motions near the knee, J. Geophys. Res., 71 (3), 693-709, Feb. 1966.

Carpenter, D. L., Whistler evidence of the dynamic behavior of the duskside bulge in the plasmasphere, J. Geophys. Res., 75, 3837, 1970.

Carpenter, D. L. and R. L. Smith, Whistler measurements of electron density in the magnetosphere, Rev. of Geophys., 2(3), 415-41, August, 1964.

Carpenter, D. L., and Keppler Stone, Direct detection by a whistler method of the magnetospheric electric field associated with a polar substorm, Planetary and Space Science, 15(2), 395-97, Feb. 1967.

Carpenter, D. L., and Keppler Stone, Jan C. Siren and T. L. Crystal, Magnetospheric electric fields deduced from drifting whistler paths, submitted to J. Geophys. Res., 1971.

Dowden, R. L. and G. Mck. Allcock, Determination of nose frequency of non-nose whistlers, J. Atmos. Terr. Phys., 33, 1125, 1971.

SEL-71-058

Helliwell, R. A., J. H. Crary, J. H. Pope, and R. L. Smith, The 'nose'
    whistler - a new high-latitude phenomenon, J. Geophys. Res., 61,
    139-142, 1956.

Helliwell, R. A., Whistlers and Related Ionospheric Phenomena, Stanford
    University Press, Stanford, California., 1965.

McIlwain, C. E., Coordinates for mapping the distribution of magnetically
    trapped particles, J. Geophys. Res., 66, 3681, 1961.

Park, C. G., Whistler observations of the interchange of ionization between
    the ionosphere and the protonosphere, J. Geophys. Res., 75, 4249,
    1970.

Park, C. G. and D. L. Carpenter, Whistler evidence of large-scale electron-
    density irregularities in the plasmasphere, J. Geophys. Res., 75,
    3825, 1970.

Smith, R. L., The use of nose whistlers in the study of the outer iono-
    sphere , Radioscience Lab., Stanford Electronics Labs., Stanford
    University, Stanford, Calif., July 1960, Tech. Rep. No. 6.

Smith, R. L. and D. L. Carpenter, Extension of nose whistler analysis,
    J. Geophys. Res., 66(8), 2582-86, August 1961.

Storey, L. R. O., An investigation of whistling atmospherics, Phil. Trans.
    Roy. Soc., A, 246, 113-141, 1953.